Thrust at N^{3}LL with power corrections and a precision global fit for $\alpha_s(m_Z)$

Riccardo Abbate,[1] Michael Fickinger,[2] André H. Hoang,[3] Vicent Mateu,[3] and Iain W. Stewart[1]

[1]*Center for Theoretical Physics, Massachusetts Institute of Technology, Cambridge, Massachusetts 02139, USA*

[2]*Department of Physics, University of Arizona, Tucson, Arizona 85721, USA*

[3]*Max-Planck-Institut für Physik (Werner-Heisenberg-Institut), Föhringer Ring 6, 80805 München, Germany*

(Received 10 August 2010; published 26 April 2011)

We give a factorization formula for the e^+e^- thrust distribution $d\sigma/d\tau$ with $\tau = 1 - T$ based on the soft-collinear effective theory. The result is applicable for all τ, i.e. in the peak, tail, and far-tail regions. The formula includes $\mathcal{O}(\alpha_s^3)$ fixed-order QCD results, resummation of singular partonic $\alpha_s^j \ln^k(\tau)/\tau$ terms with N^{3}LL accuracy, hadronization effects from fitting a universal nonperturbative soft function defined with field theory, bottom quark mass effects, QED corrections, and the dominant top mass dependent terms from the axial anomaly. We do not rely on Monte Carlo generators to determine nonperturbative effects since they are not compatible with higher order perturbative analyses. Instead our treatment is based on fitting nonperturbative matrix elements in field theory, which are moments Ω_i of a nonperturbative soft function. We present a global analysis of all available thrust data measured at center-of-mass energies $Q = 35$–207 GeV in the tail region, where a two-parameter fit to $\alpha_s(m_Z)$ and the first moment Ω_1 suffices. We use a short-distance scheme to define Ω_1, called the R-gap scheme, thus ensuring that the perturbative $d\sigma/d\tau$ does not suffer from an $\mathcal{O}(\Lambda_{\rm QCD})$ renormalon ambiguity. We find $\alpha_s(m_Z) = 0.1135 \pm (0.0002)_{\rm expt} \pm (0.0005)_{\rm hadr} \pm (0.0009)_{\rm pert}$, with $\chi^2/{\rm dof} = 0.91$, where the displayed 1-sigma errors are the total experimental error, the hadronization uncertainty, and the perturbative theory uncertainty, respectively. The hadronization uncertainty in α_s is significantly decreased compared to earlier analyses by our two-parameter fit, which determines $\Omega_1 = 0.323$ GeV with 16% uncertainty.

DOI: 10.1103/PhysRevD.83.074021 PACS numbers: 12.38.−t, 12.38.Cy, 13.66.Jn

I. INTRODUCTION

A traditional method for testing the theory of strong interactions (QCD) at high precision is the analysis of jet cross sections at e^+e^- colliders. Event shape distributions play a special role as they have been extensively measured with small experimental uncertainties at LEP and earlier e^+e^- colliders and are theoretically clean and accessible to high-order perturbative computations. They have been frequently used to make precise determinations of the strong coupling α_s; see e.g. Ref. [1] for a review. One of the most frequently studied event shape variables is thrust [2]:

$$T = \max_{\hat{\mathbf{t}}} \frac{\sum_i |\hat{\mathbf{t}} \cdot \vec{p}_i|}{\sum_i |\vec{p}_i|}, \tag{1}$$

where the sum i is over all final-state hadrons with momenta $\vec{p}_i$. The unit vector $\hat{\mathbf{t}}$ that maximizes the right-hand side of Eq. (1) defines the thrust axis. We will use the more convenient variable $\tau = 1 - T$. For the production of a pair of massless quarks at tree level $d\sigma/d\tau \propto \delta(\tau)$, so the measured distribution for $\tau > 0$ involves gluon radiation and is sensitive to the value of α_s. The thrust value of an event measures how much it resembles two jets. For τ values close to zero the event has two narrow, pencil-like, back-to-back jets, carrying about half the center-of-mass (c.m.) energy into each of the two hemispheres defined by the plane orthogonal to $\hat{\mathbf{t}}$. For τ close to the multijet end point $1/2$, the event has an isotropic multiparticle final state containing a large number of low-energy jets.

On the theoretical side, for $\tau < 1/3$ the dynamics is governed by three different scales. The *hard scale* $\mu_H \simeq Q$ is set by the e^+e^- c.m. energy Q. The *jet scale* $\mu_J \simeq Q\sqrt{\tau}$ is the typical momentum transverse to $\hat{\mathbf{t}}$ of the particles within each of the two hemispheres, or the jet invariant mass scale if all energetic particles in a hemisphere are grouped into a jet. There is also uniform soft radiation with energy $\mu_S \simeq Q\tau$, called the *soft scale*. The physical description of the thrust distribution can be divided into three regions:

$$\begin{aligned} &\text{peak region:} && \tau \sim 2\Lambda_{\rm QCD}/Q, \\ &\text{tail region:} && 2\Lambda_{\rm QCD}/Q \ll \tau \lesssim 1/3, \\ &\text{far-tail region:} && 1/3 \lesssim \tau \leq 1/2. \end{aligned} \tag{2}$$

In the *peak region* the hard, jet, and soft scales are Q, $\sqrt{Q\Lambda_{\rm QCD}}$, and $\Lambda_{\rm QCD}$, respectively, and the distribution shows a strongly peaked maximum. Theoretically, since $\tau \ll 1$ one needs to sum large (double) logarithms, $(\alpha_s^j \ln^k \tau)/\tau$, and account for the fact that $\mu_S \simeq \Lambda_{\rm QCD}$, so $d\sigma/d\tau$ is affected at leading order by a nonperturbative distribution. We call this distribution the nonperturbative soft function. The *tail region* is populated predominantly by broader dijets and 3-jet events. Here the three scales are still well separated and one still needs to sum logarithms, but now $\mu_S \gg \Lambda_{\rm QCD}$, so soft radiation can be described by

TABLE I. Recent thrust analyses which use the $\mathcal{O}(\alpha_s^3)$ fixed-order results. The theoretical components of the errors were determined as indicated, by either the error band method, variation of the renormalization scale μ, or by a simultaneous fit to $\alpha_s(m_Z)$ and α_0 (see text for more details). The analyses of Refs. [20,23] used thrust data only, while Refs. [22,24,25] employed six different event shapes.

Ref.	Sum logs	Power corrections	$\alpha_s(m_Z)$
[22]	No	MC	0.1240 ± 0.0034[a]
[20]	N^{3}LL	Uncertainty from MC model	0.1172 ± 0.0021[a]
[23]	NLL	Effective coupling model	0.1164 ± 0.0028[c]
[24]	NLL	MC	0.1172 ± 0.0051[b]
[25]	NLL	MC	0.1224 ± 0.0039[a]

[a]The error band method.
[b]Variation of the renormalization scale μ.
[c]Simultaneous fit to $\alpha_s(m_Z)$ and α_0.

perturbation theory and a series of power correction parameters Ω_i. Finally, the *far-tail* region is populated by multijet events. Here the distinction of the three scales becomes meaningless, and accurate predictions can be made with fixed-order perturbation theory supplemented with power corrections. The transition to this region must be handled carefully since including a summation of $(\alpha_s^j \ln^k \tau)/\tau$ terms in this region spoils the cancellations that take place at fixed-order multijet thresholds and hence would induce uncertainties that are significantly larger than those of the fixed-order results.

Recently two very important achievements were made improving the theoretical description of event shape distributions in e^+e^- annihilation. First, in the work of Gehrmann *et al.* in Refs. [3,4] and Weinzierl in Refs. [5,6] the full set of $\mathcal{O}(\alpha_s^3)$ contributions to the 2-, 3-, and 4-jet final states was determined. These results were made available in the program package EERAD3 [3]. Second, soft-collinear effective theory (SCET) [7–11] provides a systematic framework to treat nonperturbative corrections [12,13] and to factorize and compute hard, collinear, and soft contributions for jet production to all orders in α_s [14–16], building on earlier all-orders QCD factorization results [17–19]. The SCET framework allows for the summation of large logarithms at higher orders, as demonstrated by the analytic calculation of the thrust distribution at N^{3}LL order by Becher and Schwartz in Ref. [20].[1] In contrast, the classic exponentiation techniques of Ref. [21] for event shapes have so far only been carried out to NLL (next-to-leading-log) order. Also, the anomalous dimensions in SCET relevant for thrust are valid over perturbative momentum scales, and there are no Landau pole ambiguities in the resummation at any order. In addition, as we will discuss in the body of our paper, SCET provides a rigorous framework for including perturbative and nonperturbative contributions, which can be used to connect power corrections in factorization theorems to those in an operator expansion for thrust moments. Moreover it provides a simple method to simultaneously treat the peak, tail, and far-tail regions.

Several determinations of α_s in the tail region have been carried out incorporating the fixed-order $\mathcal{O}(\alpha_s^3)$ results, which we have collected in Table I. They differ on which event shape data have been used for the fits, on the accuracy of the partonic resummation of logarithms in the theory formula, the approach for nonperturbative hadronization effects, and how the theory errors are estimated. It is instructive to compare the analyses by Dissertori *et al.* [22,25] and by Becher and Schwartz [20], which both used the error band method [26] to determine theoretical uncertainties. The improved convergence and reduced theoretical uncertainty for $\alpha_s(m_Z)$ obtained by Becher and Schwartz indicates that the summation of logarithms beyond NLL order level is important. Both the analyses by Dissertori *et al.* and Becher and Schwartz are limited by the fact that they used Monte Carlo (MC) generators to estimate the size of nonperturbative corrections.

The use of e^+e^- MC generators to estimate power corrections is problematic since the partonic contributions are based on LL parton showers with at most one-loop matrix elements, complemented by hadronization models below the shower cutoff that are not derived from QCD. The parameters of these models have been tuned to LEP data and thus unavoidably encode both nonperturbative effects as well as higher order perturbative corrections. Hence, one must worry about double counting, and this makes MC generators unreliable for estimating nonperturbative corrections in higher order LEP analyses. Moreover, purely perturbative results for event shapes in the $\overline{\text{MS}}$ scheme such as those in Refs. [6,20,22,25] suffer from infrared effects known as infrared renormalons (see Ref. [27] for a review of the early literature). These infrared effects arise because fluctuations from large angle soft radiation down to arbitrarily small momenta are included in the $\overline{\text{MS}}$ perturbative series and can cause unphysical large corrections already in low-order perturbative QCD results. On the other hand, the hard shower cutoff protects

[1]The calculation of Ref. [20] also revealed a numerical problem at small τ in the initial fixed-order results of Refs. [3,4].

the parton level MC from infrared renormalons. Hence one cannot rigorously combine MC hadronization effects with strict perturbative $\overline{\rm MS}$ results. From the two points raised above, we conclude that the $\alpha_s(m_Z)$ results obtained in Refs. [20,22,25] contain a systematic theoretical error from nonperturbative effects that can be quite sizable. We emphasize that this criticism also applies in part to the numerous earlier event shape analyses which estimated nonperturbative corrections using MC generators; see Ref. [1] for a review.

The presence of $\Lambda_{\rm QCD}/(Q\tau)$ power corrections in $d\sigma/d\tau$ have been discussed in earlier literature [28–34], where it has been argued that the leading effect is a shift in the thrust distribution: $\tau \to \tau - 2\Lambda/Q$ with $\Lambda \sim \Lambda_{\rm QCD}$. The analyses with the $\mathcal{O}(\alpha_s^3)$ results that discuss nonperturbative effects in the thrust tail region without relying on MC generators are Ref. [20], which examined a $1/Q$ power correction in a simple soft function model but due to the large induced uncertainty on $\alpha_s(m_Z)$ does not use it for their final error analysis, and Ref. [23], which uses the effective coupling model.

For the most accurate data at $Q = m_Z$ the change to the extracted $\alpha_s(m_Z)$ from including the leading power correction can be quite significant, at the 10% level. We can derive this estimate by a simple calculation. We first write the cross section with a shift due to the power correction: $(1/\sigma)d\sigma/d\tau = h(\tau - 2\Lambda/Q)$. Assuming h is proportional to α_s, and expanding for $\Lambda/(Q\tau) \ll 1$, one can easily derive that the change in the α_s value extracted from data due to the existence of the power correction is

$$\frac{\delta\alpha_s}{\alpha_s} \simeq \frac{2\Lambda}{Q}\frac{h'(\tau)}{h(\tau)}. \tag{3}$$

The expression in Eq. (3) gives a scaling estimate for the fractional change in α_s from an analysis with the power correction compared to one without, using data at τ. To the extent that the assumptions stated above are realized, the slope factor $h'(\tau)/h(\tau)$ should be constant. In Fig. 1 we show the slope factor computed from experimental data at $Q = m_Z$. The figure shows that the slope factor is indeed only weakly depending on τ in the tail region and we get $h'(\tau)/h(\tau) \simeq -14 \pm 4$. The remaining visible variation in τ is related to subleading nonperturbative and higher power α_s effects that are not accounted for in our simple scaling estimate. For a QCD power correction of natural size, $\Lambda = 0.3$ GeV, Eq. (3) gives $\delta\alpha_s/\alpha_s \simeq -(9 \pm 3)\%$ for $Q = m_Z$. The magnitude of this effect makes it important to treat power corrections as accurately as possible in a fit to thrust data. We will show in later sections of this work that the relative downward shift in the fitted $\alpha_s(m_Z)$ due to nonperturbative effects is indeed at the level of the scaling estimate of -10%.

In the NLL/$\mathcal{O}(\alpha_s^3)$ analysis by Davison and Webber [23] the nonperturbative effects are incorporated through a power correction α_0 which is fit together with α_s to the

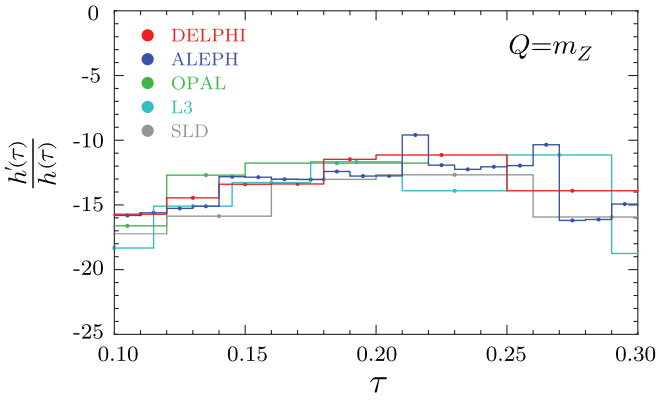

FIG. 1 (color online). Plot of $h'(\tau)/h(\tau)$, the slope of $\ln[(1/\tau)d\sigma/d\tau]$, computed from experimental data at $Q = m_Z$. The derivative is computed using the central difference with neighboring experimental bins.

experimental data. The power correction is formulated from the low-scale effective coupling model of Ref. [35], which modifies $\alpha_s(\mu)$ below $\mu = \mu_I = 2$ GeV, and defines α_0 as the average value of the coupling between $\mu = 0$ and μ_I. It is important that the effective coupling model correctly predicts the Q dependence of the leading nonperturbative power correction in factorization [17,35]. This model also induces a subtraction of perturbative contributions below the momentum cutoff μ_I (based on the running coupling approximation) and thus removes infrared renormalon ambiguities.[2] However the model is not based on factorization, and hence this treatment of nonperturbative corrections is not systematically improvable. It is therefore not easy to judge the corresponding uncertainty. Another problem of the effective coupling model is that its subtractions involve large logs, $\ln(\mu_I/Q)$, which are not resummed. This affects the Q dependence in the interplay between perturbative and nonperturbative effects.

In this paper we extend the event shape formalism to resolve the theoretical difficulties mentioned above. Our results are formulated in the SCET framework and hence are rigorous predictions of QCD. The formula we derive has a N^{3}LL order summation of logarithms for the partonic singular $\alpha_s^j \ln^k(\tau)/\tau$ terms and $\mathcal{O}(\alpha_s^3)$ fixed-order contributions for the partonic nonsingular terms. Our theoretical improvements beyond earlier work include:

(i) A factorization formula that can be simultaneously applied to data in the peak and the tail regions of the thrust distribution and for multiple c.m. energies Q, as well as being consistent with the multijet thresholds in the far-tail region.

[2]Another thrust analysis where infrared renormalon contributions have been removed from the partonic contributions is by Gardi and Rathsman in Refs. [36,37], which used a principal value prescription for the inverse Borel transformation of the thrust distribution. Their analysis was prior to the new $\mathcal{O}(\alpha_s^3)$ fixed-order computations and hence was not included in Table I.

(ii) In the factorization formula a nonperturbative soft function defined from the field theory is implemented using the method of Ref. [16] to incorporate hadronization effects. To achieve independence of a particular analytic ansatz in the peak region, the nonperturbative part of the soft function uses a linear combination of orthogonal basis functions that converge quickly for confined functions [38].

(iii) In the tail region the leading power correction to $d\sigma/d\tau$ is determined by a nonperturbative parameter Ω_1 that appears through a factorization theorem for the singular distribution. Ω_1 is a field theory matrix element of an operator and is also related to the first moment of the nonperturbative soft function. In the tail region the effects of Ω_1 hadronization corrections are included for the nonsingular corrections that are kinematically subleading in the dijet limit, based on theoretical consistency with the far-tail region.

(iv) Defining the matrix element $\bar{\Omega}_1$ in $\overline{\rm MS}$, the perturbative cross sections suffer from an $\mathcal{O}(\Lambda_{\rm QCD})$ renormalon. In our analysis this renormalon is removed by using an R-gap scheme for the definition of Ω_1 [16]. This scheme choice induces subtractions on the leading power $\overline{\rm MS}$ cross section which simultaneously remove the renormalon there. Large logarithms in the subtractions are summed to all orders in α_s using R-evolution equations given in Refs. [39,40].

(v) Finite bottom quark mass corrections are included using a factorization theorem for event shapes involving massive quarks, derived in Refs. [14,41].

(vi) QED corrections at NNLL order are incorporated, counting $\alpha_{\rm em} \sim \alpha_s^2$. This includes QED Sudakov effects, final-state radiation, and QED/QCD renormalization group interference.

(vii) The 3-loop finite term h_3 of the quark form factor in $\overline{\rm MS}$ is extracted using the results of Ref. [42] and is included in our analysis.

(viii) The most important corrections from the axial anomaly are included. The anomaly modifies the axial-vector current contributions at $\mathcal{O}(\alpha_s^2)$ by terms involving the top quark mass.

Electroweak loop effects from virtual W and Z loops mostly affect the normalization of the cross section, and so their dominant contribution drops out of $(1/\sigma)d\sigma/d\tau$ [43,44]. These corrections are not included in our analysis.

For the numerical analyses carried out in this work we have created within our collaboration two completely independent codes. One code within MATHEMATICA [45] implements the theoretical expressions exactly as given in this paper, and one code is based on theoretical formulas in Fourier space and realized as a fast FORTRAN code suitable for parallelized runs on computer clusters. These two codes agree for the thrust distribution at the level of 10^{-6}.

While the resulting theoretical code can be used for all values of τ, in this paper we focus our numerical analysis on a global fit of e^+e^- thrust data in the tail region, for c.m. energies Q between 35 and 207 GeV, to determine $\alpha_s(m_Z)$.[3] Our global fit exhibits consistency across all available data sets and reduces the overall experimental uncertainty. For a single Q we find a strong correlation between the effect of $\alpha_s(m_Z)$ and Ω_1 on the cross section. This degeneracy is broken by fitting data at multiple Q's. The hadronization uncertainty is significantly decreased by our simultaneous global fit to $\alpha_s(m_Z)$ and Ω_1. To estimate the perturbative uncertainty in the fit we use a random scan in a 12-dimensional theory parameter space. This space includes 6 parameters for μ variation, 3 parameters for theory uncertainties related to the finite statistics of the numerical fixed-order results, one parameter for the unknown 4-loop cusp anomalous dimension, and two parameters for unknown constants in the perturbative 3-loop jet and 3-loop soft functions. The scan yields a more conservative theory error than the error band method [26]. Despite this we are able to achieve smaller perturbative uncertainties than earlier analyses due to our removal of the $\mathcal{O}(\Lambda_{\rm QCD})$ renormalon and the inclusion of h_3. We also analyze in detail the dependence of the fit results on the range in τ used in the fit.

The outline of the paper is as follows. In Sec. II we introduce the theoretical framework and discuss the various theoretical ingredients in our final $d\sigma/d\tau$ formula. In Sec. III we present the profile functions which allow us to simultaneously treat multiple τ regions and discuss the 6 parameters used for μ variation in the analysis of the perturbative uncertainty. In Sec. IV we review the parametrization of the nonperturbative function. In Sec. V we discuss the normalization of our distributions and compare results at different orders in perturbation theory for fixed-order results, adding the log resummation, adding the nonperturbative corrections, and adding the renormalon subtractions. In Sec. VI we discuss the experimental data and the fit procedure. Our results for $\alpha_s(m_Z)$ and the soft function moment Ω_1 from the global fit are presented in Sec. VII, including a discussion of the theory errors. In Sec. VIII we use our tail fit results to make predictions in the far-tail and peak regions and compare with data. Cross-checks on our code are discussed in Sec. IX, including using it to reproduce the earlier lower precision fits of Dissertori *et al.* [22] and Becher and Schwartz [20]. Section X contains our conclusions and outlook, including prospects for future improvements based on the universality of the parameter Ω_1. The analytic theoretical expressions that went into our analysis for massless quarks and QCD effects are presented in condensed form in Appendix A. In Appendix B we use the operator product

[3]Throughout this paper we use the $\overline{\rm MS}$ scheme for α_s with five light flavors.

TABLE II. Perturbative and nonperturbative corrections included in our analysis. (a) Loop orders j for perturbative corrections of $\mathcal{O}(\alpha_s^j)$. Here cusp, noncusp, and $\gamma_\Delta^{\mu,R}$ refer to anomalous dimensions, while matching, nonsingular, and the gap subtraction δ refer to fixed-order series. For convenience in our numerical analysis we use the four-loop beta function for the α_s running in all orders displayed. (b) Nonperturbative corrections included in $d\sigma/d\tau$ with implicit sums over i and k. All powers $\Omega_k/(Q\tau)^k$ can be included in the peak region with the function $S_\tau^{\rm mod}$, while only a fixed set of power correction parameters are included in the tail and far-tail regions. The row labeled p.c. shows the scaling of the first power correction that is not entirely determined by the earlier rows and hence yields corrections to Eq. (4).

(a) Perturbative corrections

	Cusp	Noncusp	Matching	$\beta[\alpha_s]$	Nonsingular	$\gamma_\Delta^{\mu,R}$	δ
LL	1	None	Tree	1	None	None	None
NLL	2	1	Tree	2	None	1	None
NNLL	3	2	1	3	1	2	1
N^{3}LL	$4^{\rm pade}$	3	2	4	2	3	2
NLL$'$	2	1	1	2	1	1	1
NNLL$'$	3	2	2	3	2	2	2
N^{3}LL$'$	$4^{\rm pade}$	3	3	4	3	3	3

(b) Nonperturbative corrections with $\Omega_k \sim \Lambda_{\rm QCD}^k$

	Peak (any k)	Tail and far-tail ($k = 0, 1, 2$)
$\frac{d\hat{\sigma}_s}{d\tau}$	$\alpha_s^i \frac{\ln^j\tau}{\tau} \frac{\Omega_k}{(Q\tau)^k}$	$\alpha_s^i \frac{\ln^j\tau}{\tau} \frac{\Omega_k}{(Q\tau)^k}$
$\frac{d\hat{\sigma}_{ns}}{d\tau}$	$\alpha_s^i f_{ik}(\tau) \frac{\Omega_k}{(Q\tau)^k}$	$\alpha_s^i f_{ik}(\tau) \frac{\Omega_k}{(Q\tau)^k}$
$\frac{d\hat{\sigma}_b}{d\tau}$	$\alpha_s^i g_{ik}\left(\tau, \frac{m_b}{Q}\right) \frac{\Omega_k}{(Q\tau)^k}$	$\alpha_s^i g_{ik}\left(\tau, \frac{m_b}{Q}\right) \frac{\Omega_k}{(Q\tau)^k}$
p.c.	$\alpha_s \frac{\Lambda_{\rm QCD}}{Q}$	$\alpha_s \frac{\Lambda_{\rm QCD}}{Q}$

expansion (OPE) for the soft function in the tail region, discussing uniqueness and deriving an all-order relation for the Wilson coefficient of Ω_1. In Appendix C we use an OPE for the first moment of the thrust distribution to show that it involves the same Ω_1 at lowest order. Readers most interested in our numerical results can skip directly to Secs. VI and VII.

II. FORMALISM

A. Overview

The factorization formula we use for the fits to the experimental thrust data is

$$\frac{d\sigma}{d\tau} = \int dk \left(\frac{d\hat{\sigma}_{\rm s}}{d\tau} + \frac{d\hat{\sigma}_{\rm ns}}{d\tau} + \frac{\Delta d\hat{\sigma}_b}{d\tau}\right)\left(\tau - \frac{k}{Q}\right) \times S_\tau^{\rm mod}(k - 2\bar{\Delta}(R, \mu_S)) + \mathcal{O}\left(\sigma_0 \alpha_s \frac{\Lambda_{\rm QCD}}{Q}\right). \quad (4)$$

Here $d\hat{\sigma}_{\rm s}/d\tau$ contains the singular partonic QCD corrections $\alpha_s^j[\ln^k(\tau)/\tau]_+$ and $\alpha_s^j\delta(\tau)$ with the standard plus functions as defined in Eq. (A17). It also contains the singular partonic QED corrections depending on $\alpha_{\rm em}$ which are discussed in Sec. II H. This $d\hat{\sigma}_{\rm s}/d\tau$ term accounts for matrix element corrections and the resummation of $\ln\tau$ terms within the SCET formalism up to N^{3}LL order, which we discuss in Sec. II C. Our definition of N^{3}LL, N^{3}LL$'$, and other orders is discussed in detail in Sec. II B (see also Table II).

The term $d\hat{\sigma}_{\rm ns}/d\tau$, which we call the nonsingular partonic distribution, contains the thrust distribution in strict fixed-order expansion with the singular terms $\propto \alpha_s^j \ln^k(\tau)/\tau$ subtracted to avoid double counting. The most singular terms in $d\hat{\sigma}_{\rm ns}/d\tau$ scale as $\ln^k\tau$ for $\tau \to 0$.[4] Our implementation of nonsingular terms is discussed in detail in Sec. II E.

Finally, $\Delta d\hat{\sigma}_b/d\tau$ contains corrections to the singular and nonsingular cross sections due to the finite mass of the bottom quark. The b-mass corrections are implemented as a difference of the massive and massless cross sections computed at NNLL order as discussed in Sec. II G.

The function $S_\tau^{\rm mod}$ that is convoluted with these partonic cross sections in Eq. (4) describes the nonperturbative effects from soft gluons including large angle soft radiation [17,46]. The definition of $S_\tau^{\rm mod}$ also depends on the hemisphere prescription inherent to the thrust variable. This is a hadronic function that enters in a universal way for both massless and massive cross sections and is independent of the value of Q. The universality of $S_\tau^{\rm mod}$ in Eq. (4) follows

[4]For $d\hat{\sigma}_{\rm ns}/d\tau$ the resummation of $\ln\tau$ terms is currently unknown. These terms could be determined with subleading factorization theorems in SCET.

from the leading power thrust factorization theorem [14,15,17] and the thrust factorization theorem for massive quarks in Refs. [14,41]. Our treatment of the convolution of $S_\tau^{\rm mod}$ with $d\hat{\sigma}_{\rm ns}/d\tau$ yields a consistent treatment of multijet thresholds and the leading power correction to the operator expansion for the first moment of thrust. Details of our implementation of power corrections and nonperturbative corrections are discussed in Secs. II D and IV. The function $S_\tau^{\rm mod}$ is normalized to unity and can be determined from experimental data. Its form depends on a gap parameter $\bar{\Delta}$ and additional moment parameters Ω_i which are discussed below.

The factorization formula given in Eq. (4) can be applied simultaneously in the peak, tail, and far-tail regions of Eq. (2), i.e. for all τ values. In the peak region $d\hat{\sigma}_{\rm ns}/d\tau$ is significantly smaller than $d\hat{\sigma}_{\rm s}/d\tau$, and the full analytic form of the soft nonperturbative function $S_\tau^{\rm mod}(k)$ is relevant to determine the τ distribution since $\mu_S \simeq \Lambda_{\rm QCD}$. Because $\mu_H \gg \mu_J \gg \mu_S$, the summation of logarithms of τ is also crucial to achieve an accurate theoretical description.

For much of the tail region the summation of $\ln\tau$ terms remains important, although this is no longer the case when we reach $\tau \simeq 1/3$. Likewise, the dominance of the singular partonic contributions remains as long as $\tau < 1/3$, but the nonsingular terms become more important for increasing τ (see Fig. 7 below). Near $\tau \simeq 1/3$ the nonsingular terms become equal in size to the singular terms with opposite sign. Since $\mu_S \gg \Lambda_{\rm QCD}$ in the tail region the effects of $S_\tau^{\rm mod}$ can be parameterized in terms of the moments

$$\Omega_i = \int dk \left(\frac{k}{2}\right)^i S_\tau^{\rm mod}(k - 2\bar{\Delta}), \tag{5}$$

where $\Omega_0 = 1$ since $S_\tau^{\rm mod}$ is normalized. Their importance is determined by $\Omega_i/(Q\tau)^i$ as discussed in Sec. II D, so the first moment Ω_1 parameterizes the dominant power correction and higher moments provide increasingly smaller corrections. The first moment is defined by

$$\Omega_1 \equiv \bar{\Delta} + \frac{1}{2N_c}\langle 0|{\rm tr}\bar{Y}_{\bar{n}}^T(0)Y_n(0)i\hat{\partial}Y_n^\dagger(0)\bar{Y}_{\bar{n}}^*(0)|0\rangle, \tag{6}$$

where $Y_n^\dagger(0) = {\rm P}\exp(ig\int_0^\infty dsn\cdot A(ns))$, $\bar{Y}_{\bar{n}}^\dagger$ is similar but in the $\bar{3}$ representation, and we trace over color. Here

$$i\hat{\partial} \equiv \theta(i\bar{n}\cdot\partial - in\cdot\partial)in\cdot\partial + \theta(in\cdot\partial - i\bar{n}\cdot\partial)i\bar{n}\cdot\partial, \tag{7}$$

is a derivative operator[5] involving lightlike vectors $n = (1, \hat{\mathbf{t}})$ and $\bar{n} = (1, -\hat{\mathbf{t}})$. Ω_1 is the field theory analog of the parameter α_0 employed in the low-scale effective coupling approach to power corrections. Since the renormalon subtractions depend on a cutoff scale R and the renormalization scale μ_S, all moments $\Omega_i(R, \mu_S)$ as well as $\bar{\Delta}(R, \mu_S)$ are scale- and scheme-dependent quantities. The scheme we use to define $\Omega_1(R, \mu_S)$ is described in Sec. II F. In our fit to experimental data we use the R-gap scheme and extract the first moment at a reference scale $R_\Delta = \mu_\Delta = 2$ GeV; i.e. we use $\bar{\Delta}(R_\Delta, \mu_\Delta)$ and hence $\Omega_1 = \Omega_1(R_\Delta, \mu_\Delta)$. In the factorization theorem the gap appears evaluated at $\bar{\Delta}(R, \mu_S)$ and the scales (R, μ_S) are connected to the reference scales (R_Δ, μ_Δ) using renormalization group equations.

Finally, in the far-tail region $\tau \simeq 0.3$ the singular and the nonsingular partonic contributions $d\hat{\sigma}_{\rm s}/d\tau$ and $d\hat{\sigma}_{\rm ns}/d\tau$ become nearly equal with opposite signs, exhibiting a strong cancellation. This is due to the strong suppression of the fixed-order distribution in the three- and four-jet end point regions at $\tau \gtrsim 1/3$ in fixed-order perturbation theory. In this region the summation of logarithms of τ must be switched off to avoid messing up this cancellation. Here our Eq. (4) reduces to the pure fixed-order partonic thrust distribution supplemented with power corrections coming from the convolution with the soft function. All three regions are smoothly joined together in Eq. (4). The proper summation (or nonsummation) of logarithms is achieved through τ-dependent renormalization scales $\mu_J(\tau)$, $\mu_S(\tau)$, and $R(\tau)$ which we call *profile functions*. They are discussed in detail in Sec. III.

In the following subsections various ingredients of the factorization formula of Eq. (4) are presented in more detail. Compact results for the corresponding analytic expressions for massless quarks in QCD are given in Appendix A. In Secs. II G and II H we describe how finite bottom mass and QED corrections are included in our analysis. The full formulas for these corrections will be presented in a future publication.

B. Order counting

In the classic order counting used for fits to event shape distributions it is common to separately quote orders for the summation of logarithms and the fixed-order matching contributions. For fixed-order contributions the $\mathcal{O}(\alpha_s)$ contributions are called LO, the $\mathcal{O}(\alpha_s^2)$ contributions are called NLO, etc. This counting is motivated from the fact that at tree level the fixed-order thrust distribution vanishes for $\tau > 0$. For the summation one refers to LL (leading-log) summation if the one-loop cusp anomalous dimension is used to sum the double Sudakov logs and NLL if the two-loop cusp and the one-loop noncusp anomalous dimension terms are also included.

In our analysis the summation orders (LL, NLL, ...) match the classical language. For the fixed-order contributions we account for the tree level $\delta(\tau)$ in LL and NLL, and we include $\mathcal{O}(\alpha_s)$ corrections at NLL′ and NNLL, etc., as shown in Table II(a). In SCET the summation can be carried out at both NNLL and N^{3}LL [20]. The corresponding loop orders for the anomalous dimensions are also shown in Table II(a). Within SCET the summation of

[5]Note that $i\hat{\partial}$ is defined in the c.m. frame of the colliding e^+e^-. One may also write $i\hat{\partial} = \int d\eta e^{-|\eta|}\hat{\mathcal{E}}_T(\eta)$, where $\hat{\mathcal{E}}_T(\eta)$ measures the sum of absolute transverse momenta at a given rapidity η with respect to the thrust axis $\hat{t}$ [17,47].

logarithms is achieved by renormalization group evolution and the fixed-order corrections enter as series evaluated at each of the transition scales μ_H, μ_J, and μ_S which we refer to as matching or matrix element corrections. The logs in the singular thrust cross section exponentiate to all orders if we use y, the Fourier-transformed variable to τ. The orders we consider correspond to summing the terms

$$\ln\left[\frac{d\tilde{\sigma}_s}{dy}\right] \sim \left[L\sum_{k=1}^{\infty}(\alpha_s L)^k\right]_{\rm LL} + \left[\sum_{k=1}^{\infty}(\alpha_s L)^k\right]_{\rm NLL} + \left[\alpha_s\sum_{k=0}^{\infty}(\alpha_s L)^k\right]_{\rm NNLL} + \left[\alpha_s^2\sum_{k=0}^{\infty}(\alpha_s L)^k\right]_{\rm N^3LL}, \quad (8)$$

where $L = \ln(iy)$, and the series in the exponent makes clear the structure of the large logs that are summed at each order.

The nonsingular counting in Table II(a) for the fixed-order series in $d\hat{\sigma}_{\rm ns}/d\tau$ must be the same as for the matching and matrix element corrections to ensure that we exactly reproduce the fixed-order cross section when the resummed result is expanded. Since the relative importance of the log resummation and the nonsingular terms varies depending on the τ region, we also consider an alternative ''primed'' counting scheme. In the primed counting all series for fixed-order quantities are included to one higher order in α_s. In this counting scheme the $\mathcal{O}(\alpha_s^3)$ fixed-order results occur in N^{3}LL$'$, which is the order we use for our final analysis.

Also shown in Table II(a) are columns for the fixed-order gap subtractions $\delta = \delta(R, \mu)$ and the gap anomalous dimensions $\gamma_\Delta^{\mu,R}$. These terms are required to remove the leading $\mathcal{O}(\Lambda_{\rm QCD})$ renormalon from the perturbative corrections while still maintaining the same level of log resummation for terms in the cross section. The resummation of these large logarithms is missing in the recent analysis of Ref. [23] and is discussed further in Sec. II F.

A crucial aspect of our analysis is the inclusion of power corrections in a rigorous manner through field theoretic techniques. In the effective theory there are several types of power corrections which arise from the possible ratios of the scales μ_H, μ_J, μ_S, and $\Lambda_{\rm QCD}$:

$$(1)\ \frac{\Lambda_{\rm QCD}}{\mu_S} = \frac{\Lambda_{\rm QCD}}{Q\tau}, \quad (2)\ \frac{\mu_S^2}{\mu_J^2} = \tau, \quad (3)\ \frac{\Lambda_{\rm QCD}}{\mu_H} = \frac{\Lambda_{\rm QCD}}{Q}. \quad (9)$$

Any $\Lambda_{\rm QCD}/\mu_J$ power correction can be taken as a cross term between types 1 and 2 for the purpose of enumeration. The type 1 power corrections are enhanced by the presence of the soft scale and are encoded by the moments $\Omega_k \sim \Lambda_{\rm QCD}^k$ of the soft function. Type 2 are kinematic power corrections that occur because of the expansion about small τ and can be computed with perturbation theory. The importance of these first two types depends on the region considered in Eq. (2), with all terms in type 2 becoming leading order for the far-tail region. Type 3 are nonenhanced power corrections that are of the same size in any region. There are also cross terms between the three types.

In our analysis we keep all power corrections of types 1 and 2 and the dominant terms of type 3. Our treatment of the nonsingular cross section also includes cross terms between 1 and 2 in a manner that is discussed in Sec. II D. For the different thrust regions we display the relevant terms kept in our analysis in Table II(b). The nonsingular cross-section corrections fully account for the power corrections of type 2. The factor $[\Lambda_{\rm QCD}/(Q\tau)]^k$ in the peak region denotes the fact that we sum over all type 1 power corrections from the leading soft function. In the tail and multijet regions we only consider the first three orders: $k = 0$ (partonic result), $k = 1$ (power correction involving Ω_1), and $k = 2$ (power correction involving Ω_2). Here $k = 2$ terms are used in our error analysis for our simultaneous fit to $\alpha_s(m_Z)$ and Ω_1. The leading power correction that is not fully captured in all regions is of type 3 and is of $\mathcal{O}(\alpha_s\Lambda_{\rm QCD}/Q)$. Since our analysis is dominated by $Q = m_Z$ or larger, parametrically this gives an uncertainty of

$$\left[\frac{\delta\alpha_s}{\alpha_s}\right]_{\rm p.c.} \sim \frac{\Lambda_{\rm QCD}}{Q} \simeq 0.3\% \quad (10)$$

in our final fit (taking $\Lambda_{\rm QCD} = 0.3$ GeV to obtain the number here). This estimate has been validated by running our fits in the presence of an additional $\alpha_s\Lambda_{\rm QCD}/Q$ power correction.[6]

C. Singular partonic distribution

The singular partonic thrust distribution $d\hat{\sigma}_s/d\tau$ contains the most singular terms $\propto \alpha_s^j \ln^k(\tau)/\tau$ and $\alpha_s^j\delta(\tau)$ that arise from perturbation theory. Using SCET one can derive a factorization theorem for these terms which allows for the resummation of the logarithmic terms to all orders in perturbation theory. In massless QCD the factorization formula for the perturbative corrections involving α_s reads

$$\begin{aligned}\frac{d\hat{\sigma}_s^{\rm QCD}}{d\tau}(\tau) = Q\sum_I \sigma_0^I H_Q^I(Q,\mu_H)U_H(Q,\mu_H,\mu) \\ \times \int ds ds' J_\tau(s',\mu_J)U_J^\tau(s-s',\mu,\mu_J) \\ \times \int dk' U_S^\tau(k',\mu,\mu_S)e^{-2(\delta(R,\mu_s)/Q)(\partial/\partial\tau)} \\ \times S_\tau^{\rm part}\left(Q\tau - \frac{s}{Q} - k', \mu_S\right).\end{aligned} \quad (11)$$

Here σ_0^I is the total partonic e^+e^- cross section for quark pair production at tree level from a current of type $I = \{uv, dv, bv, ua, da, ba\}$ as explained below. Large

[6]To perform this test we include an $\alpha_s(\mu_{\rm ns})\Lambda_1/Q$ correction in the normalized thrust cross section, vary $\Lambda_1 = \pm 1.0$ GeV, and perform our default fit to $\alpha_s(m_Z)$ and Ω_1 as described in Sec. VI. This variation causes only a $\pm 0.1\%$ change to these fit parameters, which is smaller than the estimate in Eq. (10).

logs are summed by the renormalization group factors U_H between the hard scale and μ, U_J^τ between the jet scale and μ, and U_S^τ between the soft scale and μ. The choice of μ is arbitrary and the dependence on μ cancels out exactly when working at any particular order in the resummed expansion. Short-distance virtual corrections are contained in the hard function H_Q^I. The term J_τ is the thrust jet function. The term S_τ^{part} is the partonic soft function and the $\delta(R, \mu_S)$-dependent exponential implements the perturbative renormalon subtractions. There are four renormalization scales governing the factorization formula: the hard scale $\mu_H \sim Q$, the jet scale μ_J, the soft scale μ_S, and the renormalon subtraction scale R. We have $R \sim \mu_S$ to properly sum logarithms related to the renormalon subtractions, and there is also a renormalization group evolution in R. The typical values for μ_J, μ_S, and R depend on τ as discussed in Sec. III.

The total tree level partonic e^+e^- cross section $\sigma_0^I = \sigma_0^I(Q, m_Z, \Gamma_Z)$ depends on the c.m. energy Q, the Z mass, and the Z width and has six types of components: σ_0^{uv}, σ_0^{ua}, σ_0^{dv}, σ_0^{da}, σ_0^{bv}, and σ_0^{ba}, where the first index denotes flavor, u = up + charm, d = down + strange, and b = bottom, and the other index denotes production through the vector (v) and axial-vector (a) currents. For QCD corrections we have the hard functions $H_Q^v \equiv H_Q^{uv} = H_Q^{dv} = H_Q^{bv}$, H_Q^{ua}, H_Q^{da}, and H_Q^{ba}, where the vector current terms do not depend on the flavor of the quark. For massless quark production the axial-vector hard functions differ from the vector due to flavor singlet contributions. All six σ_0^I's and H_Q^I's are relevant for the implementation of the b-mass and QED corrections. Since we use data taken for energies close to the Z pole we adopt $i/(q^2 - m_Z^2 + iQ^2\Gamma_z/m_Z)$ as the Z-boson propagator which is the form of the width term used for thrust data analyses. The modifications of Eq. (11) required to include QED effects are discussed in Sec. II H.

The hard factor H_Q contains the hard QCD effects that arise from the matching of the two-jet current in SCET to full QCD. For $\mu_H = Q$ we have $H_Q^v(Q, Q) = 1 + \sum_{j=1}^3 h_j[\alpha_s(Q)/4\pi]^j$, and the full hard function with $\ln(\mu_H/Q)$ dependence is given in Eq. (A6). For the flavor nonsinglet contributions where the final-state quarks are directly produced by the current, one can obtain the matching coefficient from the on-shell quark vector current form factor, which is known to $\mathcal{O}(\alpha_s^3)$ [42,48–52]. Converting the bare result in Ref. [52] (see also Refs. [42,53]) to the $\overline{\text{MS}}$ scheme and subtracting $1/\epsilon_{\text{IR}}^k$ divergences present in SCET graphs, the three-loop nonsinglet constant, which is one of the new ingredients in our analysis, is

$$
\begin{aligned}
h_3 &= C_F^3\left[-460\zeta(3) - \frac{140\pi^2\zeta(3)}{3} + 32\zeta(3)^2 + 1328\zeta(5) - \frac{5599}{6} + \frac{4339\pi^2}{36} - \frac{346\pi^4}{15} + \frac{27\,403\pi^6}{17\,010}\right] \\
&\quad + C_A C_F^2\left[-\frac{52\,564\zeta(3)}{27} + \frac{1690\pi^2\zeta(3)}{9} + \frac{592\zeta(3)^2}{3} - \frac{5512\zeta(5)}{9} + \frac{824\,281}{324} - \frac{406\,507\pi^2}{972} + \frac{92\,237\pi^4}{2430} - \frac{1478\pi^6}{1701}\right] \\
&\quad + C_A^2 C_F\left[\frac{505\,087\zeta(3)}{243} - \frac{1168\pi^2\zeta(3)}{9} - \frac{2272\zeta(3)^2}{9} - \frac{868\zeta(5)}{9} - \frac{51\,082\,685}{26\,244} + \frac{596\,513\pi^2}{2187} - \frac{4303\pi^4}{4860} + \frac{4784\pi^6}{25\,515}\right] \\
&\quad + C_F^2 n_f\left[\frac{26\,080\zeta(3)}{81} - \frac{148\pi^2\zeta(3)}{9} - \frac{832\zeta(5)}{9} - \frac{56\,963}{486} + \frac{13\,705\pi^2}{243} - \frac{1463\pi^4}{243}\right] \\
&\quad + C_A C_F n_f\left[-\frac{8576\zeta(3)}{27} + \frac{148\pi^2\zeta(3)}{9} - \frac{8\zeta(5)}{3} + \frac{3\,400\,342}{6561} - \frac{201\,749\pi^2}{2187} - \frac{35\pi^4}{243}\right] \\
&\quad + C_F n_f^2\left[-\frac{832\zeta(3)}{243} - \frac{190\,931}{6561} + \frac{1612\pi^2}{243} + \frac{86\pi^4}{1215}\right] \\
&= 20\,060.0840 - 2473.4051 n_f + 52.2009 n_f^2. \qquad (12)
\end{aligned}
$$

For $n_f = 5$ we have $h_3 = 8998.080$, which is the value used for our analysis.[7]

The axial-vector hard functions H_Q^{ua} and H_Q^{da} are equal to H_Q^v up to additional singlet corrections that enter at $\mathcal{O}(\alpha_s^2)$ and $\mathcal{O}(\alpha_s^3)$. The fact that the SCET hard functions have these singlet corrections was discussed in Ref. [55]. At $\mathcal{O}(\alpha_s^2)$ only the axial-vector current gets a singlet correction. It arises from the axial-vector anomaly, from suitable cuts of the graph shown in Fig. 2 where each axial current is connected to a triangle. Summing over the light quarks u, d, s, and c gives a vanishing contribution from this graph, but it does not vanish for heavy quarks due to the large bottom-top mass splitting [56]. Since for the Q's we consider top pairs are never produced, the required terms can be obtained in the limit $m_b/m_t \to 0$. For the axial current the hard correction arises from the $b\bar{b}$ cut and gives $H_Q^{ua} = H_Q^{da} = H_Q^v$, and $H_Q^{ba} = H_Q^v + H_Q^{\text{singlet}}$, where

[7]The analytic expression for h_3 in Eq. (12) is consistent with Eq. (7.3) given in Ref. [54].

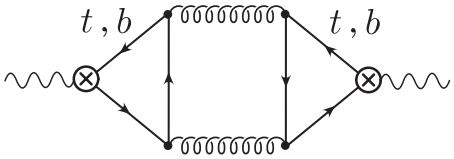

FIG. 2. Two-loop singlet correction to the axial current. Its cuts contribute to the hard coefficient and nonsingular terms.

$$H_Q^{\text{singlet}}(Q, r_t, \mu_H) = \frac{1}{3}\left(\frac{\alpha_s(\mu_H)}{\pi}\right)^2 I_2(r_t). \tag{13}$$

Here $r_t = Q^2/(4m_t^2)$ and the function $I_2(r_t)$ from Ref. [56] is given in Eq. (A7). Throughout our analysis we use $m_t = 172$ GeV. H_Q^{singlet} is a percent level correction to the cross section at the Z peak and hence is non-negligible at the level of precision of our analysis. (The uncertainty in the top mass is numerically irrelevant.) At $\mathcal{O}(\alpha_s^3)$ the singlet corrections for vector currents are known [42], but they are numerically tiny. We therefore neglect the $\mathcal{O}(\alpha_s^3)$ vector current singlet corrections together with the unknown $\mathcal{O}(\alpha_s^3)$ singlet corrections for the axial-vector current. Likewise we do not account for $\mathcal{O}(\alpha_s^3)$ singlet corrections to the nonsingular distributions discussed in Sec. II E.

The full anomalous dimension of H_Q^I is known at three loops: $\mathcal{O}(\alpha_s^3)$ [49,51,57]. It contains the cusp anomalous dimension, responsible for the resummation of the Sudakov double logarithms, and the noncusp anomalous dimension. To determine the corresponding hard renormalization group factor U_H at the orders N^{3}LL$'$ and N^{3}LL we need the $\mathcal{O}(\alpha_s^4)$ cusp anomalous dimension Γ_3^{cusp} which is still unknown and thus represents a source of theory error in our analysis. We estimate the size of Γ_3^{cusp} from the order [1/1] Padé approximant in α_s built from the known lower order coefficients, which is within 13% of the two other possible Padé approximants [0/2] and [0/1]. For our theory error analysis we assign 200% uncertainty to this estimate and hence scan over values in the range $\Gamma_3^{\text{cusp}} = 1553.06 \pm 3016.12$.

The thrust jet function J_τ is the convolution of the two hemisphere jet functions that describe collinear radiation in the $\hat{\mathrm{t}}$ and $-\hat{\mathrm{t}}$ directions:

$$\begin{aligned} J_\tau(s, \mu) &= \int ds' J(s', \mu) J(s - s', \mu) \\ &= \frac{1}{\mu^2} \sum_{n=-1}^{\infty} J_n[\alpha_s(\mu)] \mathcal{L}_n(s/\mu^2). \end{aligned} \tag{14}$$

Here the coefficients J_n are multiplied by the functions

$$\mathcal{L}_{-1}(x) = \delta(x), \qquad \mathcal{L}_n(x) = \left[\frac{\ln^n x}{x}\right]_+, \tag{15}$$

where $n \geq 0$. Here $\mathcal{L}_{n\geq 0}(x)$ are the standard plus functions; see Eq. (A17). At $\mathcal{O}(\alpha_s^3)$ only $J_{-1}(\alpha_s)$ through $J_5(\alpha_s)$ are nonzero. The results are summarized in Eq. (A16). In SCET the inclusive jet function is defined as

$$J(Qr^+, \mu) = \frac{-1}{4\pi N_c Q} \mathrm{Im}\left[i \int d^4x\, e^{ir\cdot x} \langle 0|\mathrm{T}\{\bar{\chi}_n(0) \frac{\bar{n}}{2} \chi_n(x)\}|0\rangle \right], \tag{16}$$

where the χ_n are quark fields multiplied by collinear Wilson lines. The hemisphere jet function has been computed at $\mathcal{O}(\alpha_s)$ [58,59] and $\mathcal{O}(\alpha_s^2)$ [60]. Its anomalous dimension is known at three loops and can be obtained from Ref. [61]. At the order N^{3}LL$'$ we need the $\mathcal{O}(\alpha_s^3)$ corrections to the jet function. From the anomalous dimension we know the logarithmic terms, J_0 to J_{-5} in Eq. (14), at three loops. In the nonlogarithmic term J_{-1} at $\mathcal{O}(\alpha_s^3)$ there is an unknown coefficient j_3 (which we define as the constant nonlogarithmic 3-loop coefficient in the position space hemisphere jet function). We estimate a range for j_3 from the largest value obtained from the three Padé approximations for the position space hemisphere jet function that one can construct from the available results. This gives $j_3 = 0 \pm 3000$ for the range of variation in our theory error analysis. We note that for the $\mathcal{O}(\alpha_s^3)$ coefficient h_3 the corresponding Padé estimate $h_3 = 0 \pm 10\,000$ covers the exact value given in Eq. (12).

The renormalization group factors of the thrust jet function U_J^τ and thrust soft function U_S^τ sum up large logs involving the jet and the soft scales. The required cusp and noncusp anomalous dimensions are fully known at three loops, but again there is dependence on the four-loop cusp anomalous dimension Γ_3^{cusp}. This dependence is included when we scan this parameter as described above in our description of the hard evolution.

The hadronic thrust soft function S_τ describes soft radiation between the two jets. It is defined by

$$S_\tau(k, \mu) = \frac{1}{N_c} \langle 0|\mathrm{tr} \bar{Y}_{\bar{n}}^T Y_n \delta(k - i\hat{\partial}) Y_n^\dagger \bar{Y}_{\bar{n}}^*|0\rangle, \tag{17}$$

where $Y_n = Y_n(0)$ and $\bar{Y}_{\bar{n}} = \bar{Y}_{\bar{n}}(0)$ are defined below Eq. (6). The soft function factorizes into a partonic perturbative part S_τ^{part} and a nonperturbative part S_τ^{mod}, $S_\tau = S_\tau^{\text{part}} \otimes S_\tau^{\text{mod}}$, as discussed in detail in Sec. II D. This factorization has already been used above in Eqs. (4) and (11).

At the partonic level the soft function is

$$S_\tau^{\text{part}}(k, \mu) = \frac{1}{\mu} \sum_{n=-1}^{\infty} S_n[\alpha_s(\mu)] \mathcal{L}_n(k/\mu), \tag{18}$$

where S_{-1} to S_5 are the only nonzero coefficients at $\mathcal{O}(\alpha_s^3)$, and $\mathcal{L}_n(x)$ is defined in Eq. (15). Results for these $S_k(\alpha_s)$ are summarized in Eq. (A14). S_τ^{pert} was calculated at $\mathcal{O}(\alpha_s)$ in Ref. [14,15]. At $\mathcal{O}(\alpha_s^2)$ the nonlogarithmic correction was determined in Refs. [20,62] using numerical output from EVENT2 [63,64]. The numerical constant that appears in the nonlogarithmic $\mathcal{O}(\alpha_s^2)$ term S_{-1} is referred to as s_2 (which is defined as the constant 2-loop coefficient in the logarithm of the position space soft function).

We use $s_2 = -39.1 \pm 2.5$ [62], and this uncertainty is taken into account in our theory error analysis.[8] The anomalous dimension of the soft function is a linear combination of the anomalous dimensions of the hard and jet functions which can be obtained from the consistency conditions [20,41]. As for the jet function we need the $\mathcal{O}(\alpha_s^3)$ corrections to $S_\tau^{\rm part}$. From its anomalous dimension we know the logarithmic terms at three loops, namely, S_0 to S_5 in Eq. (18). The only unknown is the $\mathcal{O}(\alpha_s^3)$ nonlogarithmic correction in S_{-1}, referred to as s_3 (which is defined as the constant nonlogarithmic term in the logarithm of the position space hemisphere soft function). Just like for the constant j_3 we estimate a value for s_3 from the largest value obtained from the three possible Padé approximations to the position space soft function that one can construct from the available results. This yields the range $s_3 = 0 \pm 500$, which we scan over in our theory error analysis.

As already mentioned, in Ref. [20] an analytic expression for the resummed singular thrust distribution was presented. Their derivation relies on the Laplace transform of the jet and soft functions. In our analysis we have derived the resummed cross section using two independent procedures, performing all convolutions either in momentum space (as presented in Appendix A) or in Fourier space. These two approaches have been implemented in two independent codes and we have checked that they give exactly the same results. We note that the Fourier transform method is equivalent to the Laplace procedure used by Becher and Schwartz in Ref. [20] through a contour deformation, and we find agreement with their quoted N^{3}LL formula including matrix elements and anomalous dimensions. Furthermore, we also agree with their result for the fixed-order singular terms up to $\mathcal{O}(\alpha_s^3)$.

In summary, the singular terms in the thrust factorization theorem are known at N^{3}LL order, up to the unknown constant $\Gamma_3^{\rm cusp}$. The effect of the cusp anomalous dimension at 4 loops is much smaller than one might estimate, so for numerical purposes the cross section is known at this order. The constants s_3 and j_3 only enter for our N^{3}LL$'$ order. For the singular terms they predominantly affect the peak region with spread into the tail region only due to renormalization group evolution. Thus in the tail region the numerically dominant N^{3}LL$'$ terms are all known. The uncertainties from $\Gamma_3^{\rm cusp}$, s_3, and j_3 are discussed more explicitly in Sec. VII.

D. Ω_1 and nonperturbative corrections

In this section we discuss nonperturbative corrections to the thrust distribution included in our analysis, as shown in Table II(b). We focus, in particular, on those associated to the first moment parameter Ω_1. Our analysis includes the OPE for the soft function in the tail region and combining perturbative and nonperturbative information to smoothly connect the peak and tail analyses. We also discuss our treatment of nonperturbative corrections in the far-tail region and for the nonsingular terms in the cross section.

In the tail region where $k \sim Q\tau \gg \Lambda_{\rm QCD}$ we can perform an operator product expansion of the soft function in Eq. (17). At tree level this gives [65,66]

$$S_\tau(k,\mu) = \delta(k) - \delta'(k) 2\bar\Omega_1 + \cdots, \tag{19}$$

where the nonperturbative matrix element $\bar\Omega_1$ is defined in the $\overline{\rm MS}$ scheme as

$$\bar\Omega_1 = \frac{1}{2N_c}\langle 0|{\rm tr}\bar Y_{\bar n}^T(0) Y_n(0) i\hat\partial Y_n^\dagger(0)\bar Y_{\bar n}^*(0)|0\rangle. \tag{20}$$

Dimensional analysis indicates that $\bar\Omega_1 \sim \Lambda_{\rm QCD}$. When the OPE is performed beyond tree level we must add perturbative corrections at a scale $\mu \simeq k$ to Eq. (19). The first operator in the OPE is the identity, and its Wilson coefficient is the partonic soft function. Thus $\delta(k) \to S_\tau^{\rm part}(k,\mu)$ when the matching of the leading power operator is performed at any fixed order in the perturbation theory. Here we derive the analog for the Wilson coefficient of the $\bar\Omega_1$ matrix element and prove that

$$S_\tau(k,\mu) = S_\tau^{\rm part}(k) - \frac{dS_\tau^{\rm part}(k)}{dk} 2\bar\Omega_1 + \cdots. \tag{21}$$

This result implies that the leading perturbative corrections that multiply the power correction are determined by the partonic soft function to all orders in the perturbation theory. The proof of Eq. (21) is given in Appendix B. The uniqueness of the leading power correction $\bar\Omega_1$ to all orders in the perturbative matching can be derived following Ref. [65], and we carry out an all-orders matching computation to demonstrate that the Wilson coefficient is $dS_\tau^{\rm part}(k)/dk$. At first order in $\bar\Omega_1/k \ll 1$ Eq. (21) shows that the perturbative corrections in the OPE are consistent with a simple shift to $S_\tau(k - 2\bar\Omega_1, \mu)$. This type of shift was first observed in the effective coupling model [35].

To smoothly connect the peak and tail regions we use a factorized soft function [16,18,38]

$$S_\tau(k,\mu) = \int dk' S_\tau^{\rm part}(k-k',\mu) S_\tau^{\rm mod}(k'), \tag{22}$$

where $S_\tau^{\rm part}$ is a fixed-order perturbative $\overline{\rm MS}$ expression for the partonic soft function and $S_\tau^{\rm mod}$ contains the nonperturbative ingredients. In the tail region this expression can be expanded for $k' \ll k$ and reduces to precisely the OPE in Eq. (21) with the identification

$$2\bar\Omega_1 = \int dk' k' S_\tau^{\rm mod}(k'), \tag{23}$$

and normalization condition $\int dk' S_\tau^{\rm mod}(k') = 1$ [16]. All moments of $S_\tau^{\rm mod}(k')$ exist so it has an exponential tail, whereas the tail for $S_\tau^{\rm part}(k)$ is a power law. In the peak region the full nonperturbative function $S_\tau^{\rm mod}(k)$ becomes

[8] Note that in Ref. [62] our s_2 was called s_1.

relevant, and Eq. (22) provides a nonperturbative function whose μ dependence satisfies the $\overline{\rm MS}$ renormalization group equation (RGE) for the soft function. In position space the convolution in Eq. (22) is a simple product, making it obvious that Eq. (22) provides a completely general parametrization of the nonperturbative corrections. The complete basis of functions used to parameterize $S_\tau^{\rm mod}(k)$ in the peak region is discussed in Sec. IV.

The expression in Eq. (22) also encodes higher order power corrections of type 1 from Eq. (9) through the moments $2^i\bar\Omega_i = \int dk k^i S_\tau^{\rm mod}(k)$, which for tree level matching in the OPE can be identified as the matrix elements $\langle 0|{\rm tr}\bar Y_{\bar n}^T(0)Y_n(0)(i\hat\partial)^i Y_n^\dagger(0)\bar Y_{\bar n}^*(0)|0\rangle/N_c$. For $i \geq 2$ perturbative α_s corrections to the soft function OPE would have to be treated in a manner similar to Appendix B to determine the proper Wilson coefficients and whether additional operators beyond the powers $(i\hat\partial)^i$ start contributing. The treatment of perturbative corrections to these higher order nonperturbative corrections is beyond the level required for our analysis.

Using Eq. (22) the hadronic version of the singular factorization theorem which involves S_τ immediately yields Eq. (11) and the first term in Eq. (4). The conversion of $S_\tau^{\rm part}(k)$ and $\bar\Omega_1$ from $\overline{\rm MS}$ to a renormalon-free scheme is discussed in Sec. II F.

Next we turn to the effect of $\Lambda_{\rm QCD}$ power corrections on the nonsingular terms in the cross section in Eq. (4). The form of these power corrections can be constrained by factorization theorems for subleading power corrections when $\tau \ll 1$ and by carrying out an OPE analysis for power corrections to the moments of the thrust distribution. In the following we consider both of these.

Based on the similarity of the analysis of power corrections to thrust with those in $B \to X_s\gamma$ [67,68], the factorization theorems for the nonsingular corrections involve subleading hard functions, jet functions, and soft functions. They have the generic structure $H_Q^{(a,b)}(Q,\tau,x_i) \otimes J_\tau^{(a)}(s_j,x_i) \otimes S_\tau^{(b)}(Q\tau, s_j/Q)$, where the x_i and s_j are various convolution variables. Here $S_\tau^{(b)}$ includes the leading order soft function in Eq. (17) as well as power suppressed soft functions. Neglecting nonperturbative corrections the nonsingular cross section yields terms we refer to as kinematic power corrections of type 2 in Eq. (9). If we do not wish to sum large logs in the nonsingular partonic terms, they can be treated in fixed-order perturbation theory and determined from the full fixed-order computations. In the tail region these τ-suppressed terms grow and become much more important than the $\Lambda_{\rm QCD}/Q$ power corrections of type 3 from subleading soft functions. In the transition to the far-tail region, near $\tau = 1/3$, they become just as important as the leading perturbative singular terms. In this region there are large cancellations between the singular and nonsingular terms (shown below in Fig. 7), and one must be careful with the treatment of the nonsingular terms not to spoil this.

We require the nonsingular cross-section terms to yield perturbative corrections at leading power in $\Lambda_{\rm QCD}$ that are consistent with the fixed-order results and with multijet thresholds. Our treatment of power corrections in the nonsingular terms is done in a manner consistent with these goals and with the OPE for the first moment of the thrust distribution. To achieve this we use

$$\int dk' \frac{d\hat\sigma_{\rm ns}}{d\tau}\Big(\tau - \frac{k'}{Q}, \frac{\mu_{\rm ns}}{Q}\Big) S_\tau^{\rm mod}(k'), \tag{24}$$

where $d\hat\sigma_{\rm ns}/d\tau$ is the partonic nonsingular cross section in the fixed-order perturbation theory, whose determination we discuss in Sec. II E. Equation (24) is independent of the renormalization scale $\mu_{\rm ns}$ order by order in its series expansion in $\alpha_s(\mu_{\rm ns})$. The convolution with the same $S_\tau^{\rm mod}(k')$ as the singular terms allows the perturbative corrections in $d\hat\sigma_s/d\tau + d\hat\sigma_{\rm ns}/d\tau$ to smoothly recombine into the fixed-order result in the far-tail region as required by the multijet thresholds. Equation (24) yields the second term in Eq. (4). We will treat the conversion of $\bar\Omega_1$ and $S_\tau^{\rm mod}$ to a renormalon-free scheme in the same manner as for the singular cross section, which again for consistency requires a perturbative subtraction for the partonic $d\hat\sigma_{\rm ns}/d\tau$ that we treat in Sec. II F.

Note that Eq. (24) neglects the fact that not all of the τ dependence in $d\hat\sigma_{\rm ns}/d\tau$ must necessarily be convoluted with $S_\tau^{\rm mod}$. This causes a deviation which is $\sim\alpha_s\tau\Lambda_{\rm QCD}/(Q\tau)$ and hence is at the same level as other power corrections that we neglect. The largest uncertainty from our treatment of $d\hat\sigma_{\rm ns}/d\tau$ arises from the fact that we do not sum $\ln\tau$ terms, which would require anomalous dimensions for the subleading soft and hard functions for these nonsingular terms. These logs are most important in the peak region and less relevant in the tail region. The size of missing higher order nonsingular terms such as log enhanced terms will be estimated by varying the scale $\mu_{\rm ns}$.

Our setup is also consistent with the OPE for the first moment of the thrust distribution. Equation (4) yields

$$\int d\tau\, \tau \frac{d\sigma}{d\tau} = \int d\tau\, \tau\Big[\frac{d\hat\sigma_s}{d\hat\tau} + \frac{d\hat\sigma_{\rm ns}}{d\hat\tau}\Big] + \sum_I \sigma_0^I \frac{2\bar\Omega_1}{Q} + \cdots, \tag{25}$$

where the ellipses denote $\mathcal{O}(\alpha_s\Lambda_{\rm QCD}/Q)$ and $\mathcal{O}(\Lambda_{\rm QCD}^2/Q^2)$ power corrections. In Appendix C we demonstrate that a direct OPE computation for the thrust moment also gives the same result and, in particular, involves precisely the same matrix element $\bar\Omega_1$ at this order. The theoretical expression in Eq. (4) simultaneously includes the proper matrix elements that encode power corrections in the peak region and tail region and for moments of the thrust distribution. This implies a similar level of precision for the multijet region. Although Eq. (4) does not encode

all $\alpha_s\Lambda_{\rm QCD}/Q$ corrections, it turns out that the ones it does encode, involving Ω_1, numerically give an accurate description of the multijet cross section. (This is visible in Fig. 18 and will be discussed further in Sec. VII.) This agreement provides additional support for our treatment of nonperturbative corrections in the nonsingular cross section in Eq. (24).

E. Nonsingular distribution

The nonsingular partonic thrust distribution $d\hat{\sigma}_{\rm ns}/d\tau$ accounts for contributions in the thrust distribution that are kinematically power suppressed. We write

$$\frac{d\hat{\sigma}_{\rm ns}}{d\tau}(\tau) = \sum_I \sigma_0^I e^{-2(\delta(R,\mu_s)/Q)(\partial/\partial\tau)} f^I\left(\tau, \frac{\mu_{\rm ns}}{Q}\right), \qquad (26)$$

with the same superscript I notation for different currents as in Eq. (11). The presence of the $\delta(R, \mu_S)$-dependent exponent arises because $S_\tau^{\rm mod}$ depends on Ω_1 and we use the same renormalon-free definition for Ω_1 as for the singular terms. In our numerical evaluation we integrate by parts so that the $\partial/\partial\tau$ derivative acts on $S_\tau^{\rm mod}$ in Eq. (4). This exponent is discussed in detail in Sec. II F.

In this section we discuss our determination of the functions f^I in pure QCD with massless quarks, while the generalization to include m_b effects is discussed in Sec. II G and to include QED effects in Sec. II H. For pure QCD there is one function $f^v_{\rm qcd} = f^{uv}_{\rm qcd} = f^{dv}_{\rm qcd} = f^{bv}_{\rm qcd}$ for the vector current and functions $f^{ua}_{\rm qcd} = f^{da}_{\rm qcd}$ and $f^{ba}_{\rm qcd}$ for the axial-vector currents. In general f^I is the partonic fixed-order distribution where the singular terms which are already contained in $d\hat{\sigma}_{\rm s}/d\tau$ are subtracted to avoid double counting. Setting the renormalization scale $\mu_{ns} = Q$ they have the form

$$\begin{aligned} f^v_{\rm qcd}(\tau, 1) &= \frac{\alpha_s}{2\pi} f_1(\tau) + \frac{\alpha_s^2}{(2\pi)^2} f_2(\tau) + \frac{\alpha_s^3}{(2\pi)^3} f_3(\tau) + \cdots, \\ f^{ua}_{\rm qcd}(\tau, 1) &= f^{da}_{\rm qcd}(\tau, 1) = f^v_{\rm qcd}(\tau, 1), \\ f^{ba}_{\rm qcd}(\tau, 1) &= f^v_{\rm qcd}(\tau, 1) + \frac{\alpha_s^2}{(2\pi)^2} f_{\rm singlet}(\tau, r_t), \end{aligned} \qquad (27)$$

where $\alpha_s = \alpha_s(Q)$ and $r_t = Q^2/(4m_t^2)$. The required results for $f^I(\tau, \mu_{\rm ns}/Q)$ can be obtained by shifting $\alpha_s(Q)$ to $\alpha_s(\mu_{\rm ns})$ using the fixed-order relation between these couplings at $\mathcal{O}(\alpha_s^2)$.

The full $\mathcal{O}(\alpha_s)$ partonic thrust distribution has been known analytically for a long time [69]. For the one-loop nonsingular distribution it gives

$$\begin{aligned} f_1(\tau) = \frac{4}{3\tau(\tau-1)}\Big[&(-6\tau^2 + 6\tau - 4)\log\Big(\frac{1}{\tau} - 2\Big) + 9\tau^3 \\ &- 3\tau^2 - 9\tau + 3\Big]\theta\Big(\frac{1}{3} - \tau\Big) + \frac{4}{3\tau}[3 + 4\log(\tau)]. \end{aligned} \qquad (28)$$

This result is plotted in Fig. 3. The kink at $\tau = 1/3$ appears because the full one-loop distribution vanishes at this value with a nonzero slope, and there is an exact cancellation between the fixed-order singular and nonsingular one-loop expressions. For $\tau > 1/3$ the one-loop nonsingular distribution is precisely the negative of the one-loop fixed-order singular distribution.

The $\mathcal{O}(\alpha_s^2)$ and $\mathcal{O}(\alpha_s^3)$ QCD distributions are available in numeric form from the FORTRAN programs EVENT2 [63,64] and EERAD3 [3] (see also Refs. [4–6]), respectively. These programs are used to derive results for our $f_2(\tau)$ and $f_3(\tau)$ nonsingular distributions in a manner discussed below. At $\mathcal{O}(\alpha_s^2)$ there is also the singlet correction $f_{\rm singlet}(\tau, r)$ for the axial-vector contribution arising from the large bottom-top mass splitting. The three-parton quark-antiquark-gluon cut from Fig. 2 contributes to the nonsingular distribution, and we have included this contribution analytically [70]. The formula for $f_{\rm singlet}(\tau, r)$ is given in Eq. (A30). There is also a contribution from the four-parton cut. Its contribution to $f_{\rm singlet}(\tau, r)$ is unknown, but it is tiny for the total cross section [56] and can therefore be safely neglected.

At $\mathcal{O}(\alpha_s^2)$ we use linear binned EVENT2 results for $\tau > 0.095$ and log-binning results for $\tau < 0.095$ each obtained from runs with 10^{10} events and infrared cutoff $y_0 = 10^{-8}$. For $\tau > 0.095$ (using a 0.005 bin size) the resulting statistical uncertainties in the nonsingular distribution are always below the percent level and negligible and we can use an interpolation of numerical tables for $f_2(\tau)$. For $\tau < 0.095$ the singular terms dominate the distribution which leads to large cancellations and an enhancement of the statistical uncertainties. Here we use the ansatz $f_2(\tau) = \sum_{i=0}^3 a_i \ln^i\tau + \tau\sum_{i=2}^3 b_i \ln^i\tau$ and fit the coefficients a_i and b_i to the EVENT2 output, including the constraint that the integral over the full distribution reproduces the known $\mathcal{O}(\alpha_s^2)$ coefficient for the total cross section. The result has the form $f_2(\tau) + \epsilon_2\delta_2(\tau)$, where f_2 represents the best fit and δ_2 is the 1-sigma error function with all correlations included. The term ϵ_2 is a parameter which we vary during our α_s-Ω_1 fit procedure to account for the error. Here f_2

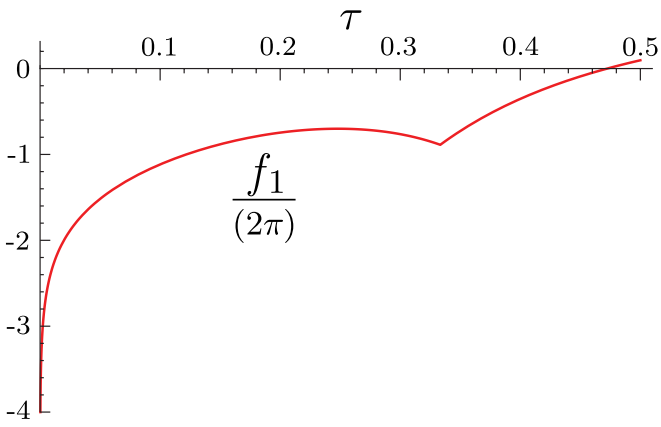

FIG. 3 (color online). $\mathcal{O}(\alpha_s)$ nonsingular thrust distribution.

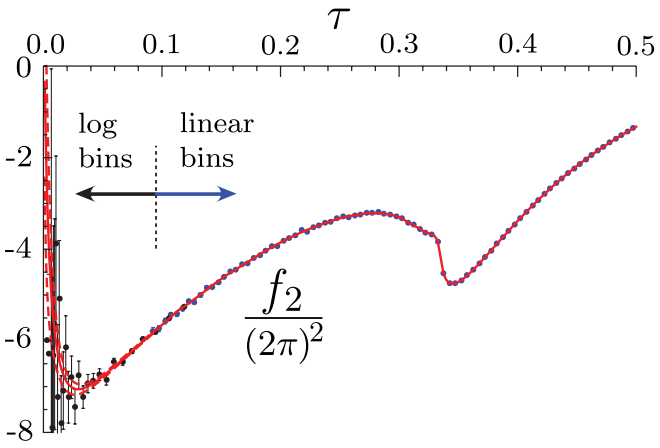

FIG. 4 (color online). $\mathcal{O}(\alpha_s^2)$ nonsingular thrust distribution.

and δ_2 also depend on the coefficient s_2 in the partonic soft function S_τ which is known only numerically. In Fig. 4 we plot the EVENT2 data we used, along with our $f_2(\tau)$ with $s_2 = -39.1$. The dashed curves show the result for $\epsilon_2 = \pm 1$, with the region in between corresponding to the 1-sigma error band.

For the determination of f_3 at $\mathcal{O}(\alpha_s^3)$ we implement a similar approach as for f_2, using results from EERAD3 [3] computed with 6×10^7 events for the three leading color structures and 10^7 events for the three subleading ones, using an infrared cutoff $y_0 = 10^{-5}$. We employ linearly binned results with 0.01 bin size for $\tau > 0.315$ (keeping the statistical error below the percent level) and with 0.005 bin size for $\tau < 0.315$. For the fit for $\tau < 0.315$ our ansatz function has the form $f_3(\tau) = \sum_{i=1}^{5} c_i \ln^i \tau$ and the result has the form $f_3(\tau) + \epsilon_3 \delta_3(\tau)$, with f_3 being the best fit and δ_3 the 1-sigma error function. The constant ϵ_3 is the analog of ϵ_2 and is varied in the error analysis. We note that f_3 and δ_3 depend on the constant s_2 and on the constants s_3 and j_3 that account for the unknown nonlogarithmic terms in the $\mathcal{O}(\alpha_s^3)$ soft and jet functions. This dependence is included

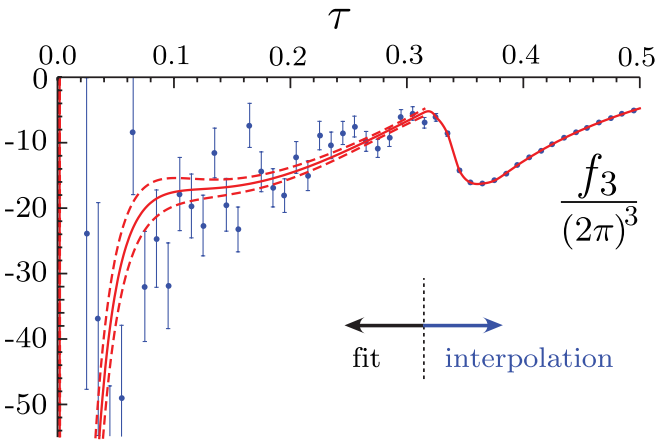

FIG. 5 (color online). $\mathcal{O}(\alpha_s^3)$ nonsingular thrust distribution. For simplicity we only show the data binned with 0.01 bin size.

in our error analysis. In Fig. 5 we plot the EERAD3 data with bin size 0.01, along with our $f_3(\tau)$ with $s_2 = -39.1$, $h_3 = 8998.08$, and $j_3 = s_3 = 0$. The dashed curves show the result for $\epsilon_3 = \pm 1$, with the region in between corresponding to the 1-sigma error band.

In our analysis we use the values -1, 0, and 1 for ϵ_2 and ϵ_3 to account for the numerical uncertainties of our fit functions in the small τ region. The nonsingular partonic distribution depends on one common renormalization scale $\mu_{\rm ns}$ which is varied in our theory error analysis as given in Sec. III.

F. Gap formalism

The partonic soft function $S_\tau^{\rm part}(k)$ computed perturbatively in $\overline{\rm MS}$ has an $\mathcal{O}(\Lambda_{\rm QCD})$ renormalon ambiguity. The same renormalon is present in the partonic $\overline{\rm MS}$ thrust cross section with or without resummation. This is associated with the fact that the partonic threshold at $k = 0$ in $S_\tau^{\rm part}(k)$ is not the same as the physical hadronic threshold for the distribution of soft radiation that occurs in $S_\tau(k)$. One can see this explicitly in the large-β_0 approximation, where it is associated to a pole at $u = 1/2$ in the Borel transform [16]

$$B[S_\tau^{\rm part}(k,\mu)]\Big(u \approx \frac{1}{2}\Big) = \mu \frac{16 C_F e^{-5/6}}{\pi \beta_0 (u - \frac{1}{2})} \frac{\partial}{\partial k} S_\tau^{\rm part}(k,\mu). \quad (29)$$

This result shows that $S_\tau^{\rm part}(k)$ in the $\overline{\rm MS}$ scheme suffers from the renormalon ambiguity for all $k \geq 0$. The $\overline{\rm MS}$ matrix element $\bar{\Omega}_1$ defined in Eq. (20) also has an $\mathcal{O}(\Lambda_{\rm QCD})$ renormalon ambiguity. Together, the renormalons in this power correction and in the perturbative series for $S_\tau^{\rm part}(k)$ combine to give a soft function $S_\tau(k)$ that is free from this $\mathcal{O}(\Lambda_{\rm QCD})$ renormalon. If left unsubtracted, this renormalon ambiguity leads to numerical instabilities in perturbative results for the thrust distribution and in the large order dependence for the determination of the soft nonperturbative function $S_\tau^{\rm mod}$. In this section we resolve this problem by switching to a new scheme for Ω_1. This scheme change induces subtractions on $d\sigma^{\rm part}/d\tau$ that render it free of this renormalon. We start by reviewing results from Ref. [16].

Consider a class of soft nonperturbative functions with a gap parameter Δ, which only have support for $k \geq \Delta$, so $S_\tau^{\rm mod}(k) \to S_\tau^{\rm mod}(k - 2\Delta)$. Here the $\overline{\rm MS}$ moment relation in Eq. (23) becomes

$$2\Delta + \int dk\, k S_\tau^{\rm mod}(k) = 2\bar{\Omega}_1, \quad (30)$$

where Δ accounts for the complete renormalon ambiguity contained in $\bar{\Omega}_1$. We can now obtain a renormalon-free definition for Ω_1 by splitting Δ into a nonperturbative component $\bar{\Delta}(R, \mu_S)$ that is free of the $\mathcal{O}(\Lambda_{\rm QCD})$ renormalon and a suitably defined perturbative series $\delta(R, \mu_S)$ that

has the same renormalon ambiguity as $\bar{\Omega}_1$. The parameter Δ is scheme and renormalization group invariant, while $\bar{\Delta}$ and δ individually depend on the subtraction scale R and in general also on the soft scale μ_S. Writing

$$\Delta = \bar{\Delta}(R, \mu_S) + \delta(R, \mu_S), \tag{31}$$

the factorization of perturbative and nonperturbative components in Eq. (22) becomes

$$\begin{aligned} S_\tau(k, \mu_S) &= \int dk' S_\tau^{\text{part}}(k - k' - 2\delta, \mu_S) S_\tau^{\text{mod}}(k' - 2\bar{\Delta}) \\ &= \int dk' [e^{-2\delta(\partial/\partial k)} S_\tau^{\text{part}}(k - k', \mu_S)] S_\tau^{\text{mod}}(k' - 2\bar{\Delta}). \end{aligned} \tag{32}$$

Here the exponential operator induces perturbative subtractions [in powers of $\alpha_s(\mu_S)$] on the $\overline{\text{MS}}$ series in $S_\tau^{\text{part}}(k)$ that render it free of the renormalon. This exponential modifies perturbative results for the cross section in the manner we have shown earlier in Eqs. (11) and (26). The convolution of the nonsingular cross section with S_τ^{mod} in Eq. (24) now becomes

$$\int dk' \frac{d\hat{\sigma}_{\text{ns}}}{d\tau}\left(\tau - \frac{k'}{Q}, \frac{\mu_{\text{ns}}}{Q}\right) S_\tau^{\text{mod}}(k' - 2\bar{\Delta}). \tag{33}$$

Furthermore, with Eq. (32) the result in Eq. (30) becomes

$$2\bar{\Delta}(R, \mu_S) + \int dk\, k\, S_\tau^{\text{mod}}(k) = 2\Omega_1(R, \mu_S), \tag{34}$$

where $\Omega_1(R, \mu_S)$ is renormalon-free. Combining Eqs. (34) and (30) we see that the scheme conversion formula from $\overline{\text{MS}}$ to the new scheme is

$$\Omega_1(R, \mu_S) = \bar{\Omega}_1 - \delta(R, \mu_S). \tag{35}$$

Thus, the precise scheme for $\Omega_1(R, \mu_S)$ is specified by the choice of the subtraction series $\delta(R, \mu_S)$. Note that in general the gap parameter $\bar{\Delta}$ is an additional nonperturbative parameter that can be determined together with other parameters in the function S_τ^{mod} from fits to experimental data. However, in the tail region the power corrections are dominated by a single parameter, $\Omega_1(R, \mu_S)$, which encodes the dependence on $\bar{\Delta}$.

In Ref. [62] a convenient scheme for $\delta(R, \mu_S)$ was derived (based on a scheme proposed in Ref. [71]) where

$$\delta(R, \mu) = \frac{R}{2} e^{\gamma_E} \frac{d}{d\ln(ix)} [\ln S_\tau(x, \mu)]|_{x=(iRe^{\gamma_E})^{-1}}. \tag{36}$$

Here $S_\tau(x, \mu)$ is the position space partonic soft function, and the fact that we write this result for S_τ rather than for the hemisphere soft function explains the extra factor of $1/2$ relative to the formula in Ref. [62]. The cutoff parameter R, having mass dimension 1, is a scale associated with the removal of the infrared renormalon. To achieve the proper cancellation of the renormalon in Eq. (32) one has to expand $\delta(R, \mu_S)$ together with $S_\tau^{\text{part}}(k, \mu_S)$ order by order in $\alpha_s(\mu_S)$. The perturbative series for the subtraction is

$$\delta(R, \mu_S) = e^{\gamma_E} R \sum_{i=1}^{\infty} \alpha_s^i(\mu_S) \delta_i(R, \mu_S), \tag{37}$$

where the $\delta_{i\geq 2}$ depend on both the adjoint Casmir $C_A = 3$ and the number of light flavors in combinations that are unrelated to the QCD beta function. For five light flavors the one-, two-, and three-loop coefficients are [62]

$$\begin{aligned} \delta_1(R, \mu_S) &= -0.848\,826 L_R, \\ \delta_2(R, \mu_S) &= -0.156\,279 - 0.466\,63 L_R - 0.517\,864 L_R^2, \\ \delta_3(R, \mu_S) &= 0.075\,683\,1 + 0.015\,453\,86 s_2 - 0.622\,467 L_R \\ &\quad - 0.777\,219 L_R^2 - 0.421\,261 L_R^3, \end{aligned} \tag{38}$$

with $L_R = \ln(\mu_S/R)$. We will refer to the scheme defined by Eq. (36) as the R-gap scheme for Ω_1.

From the power counting $\bar{\Omega}_1 \sim \Lambda_{\text{QCD}}$ one expects that a cutoff $R \sim 1$ GeV should be used, such that $\Omega_1 \sim \Lambda_{\text{QCD}}$ and the perturbation theory in $\alpha_s(R)$ remains applicable. We refer to this as the power counting criterion for R. Since in the tail region $\mu_S \sim Q\tau \gg 1$ GeV the factors of L_R in Eq. (38) are then large logs. To avoid large logarithms in the subtractions $\delta_i(R, \mu_S)$ it is essential to choose $R \sim \mu_S$, so that the subtraction scale R is dependent on τ much like the soft scale μ_S. We refer to this as the large-log criterion for R. To resolve the conflict between these two criteria and sum the large logs while keeping $\bar{\Delta}(R, \mu_S \sim R)$ renormalon-free, we make use of R evolution [39,40]. Formulas for the gap case were given in Ref. [62] and are reviewed here. In this scheme $\bar{\Delta}(R, \mu)$ satisfies an R-RGE and μ-RGE

$$\begin{aligned} R\frac{d}{dR}\bar{\Delta}(R, R) &= -R \sum_{n=0}^{\infty} \gamma_n^R \left(\frac{\alpha_s(R)}{4\pi}\right)^{n+1}, \\ \mu\frac{d}{d\mu}\bar{\Delta}(R, \mu) &= 2Re^{\gamma_E} \sum_{n=0}^{\infty} \Gamma_n^{\text{cusp}} \left(\frac{\alpha_s(\mu)}{4\pi}\right)^{n+1}, \end{aligned} \tag{39}$$

so that $\gamma_\Delta^\mu = -2e^{\gamma_E}\Gamma^{\text{cusp}}[\alpha_s]$. For five flavors the anomalous dimension coefficients up to three loops are

$$\begin{aligned} \gamma_0^R &= 0, \\ \gamma_1^R &= -43.954\,260, \\ \gamma_2^R &= 1615.422\,28 + 54.619\,554\,1 s_2, \end{aligned} \tag{40}$$

while the coefficients Γ_n^{cusp} are given in Eq. (A26). The solution of Eq. (39) at N^{k}LL is

$$\begin{aligned} \bar{\Delta}(R, \mu) &= \bar{\Delta}(R_\Delta, \mu_\Delta) + Re^{\gamma_E}\omega[\Gamma^{\text{cusp}}, \mu, R] \\ &\quad + R_\Delta e^{\gamma_E}\omega[\Gamma^{\text{cusp}}, R_\Delta, \mu_\Delta] \\ &\quad + \Lambda_{\text{QCD}}^{(k)} D^{(k)}[\alpha_s(R), \alpha_s(R_\Delta)], \end{aligned} \tag{41}$$

where the resummed $\omega[\Gamma^{\rm cusp}, \mu, \mu_0]$ is given in Eq. (A23) and the resummed $D^{(k)}[\alpha_s(R), \alpha_s(R_\Delta)]$ is given in Eq. (A31). Both the gap subtraction and R-evolution equations at $\mathcal{O}(\alpha_s^3)$ depend on the constant s_2 which we vary within its errors in our theory error scan. In our analysis, when quoting numerical results, we always use the parameter $\bar\Delta(R_\Delta, \mu_\Delta)$ at the reference scales $R_\Delta = \mu_\Delta = 2$ GeV to satisfy the power counting criterion for R. We then use Eq. (41) to run up to the scale $R \sim \mu_S$ in order to satisfy the large-log criterion. The precise R value is a function of τ, $R = R(\tau)$, and given in Sec. III with our discussion of the profile functions. The RGE solution for $\bar\Delta(R, \mu_S)$ in Eq. (41) yields a similar solution for a running $\Omega_1(R, \mu_S)$ using Eq. (34). In Fig. 6 we show the result for the running $\Omega_1(R, R)$ with the boundary value $\Omega_1(R_\Delta, \mu_\Delta) = 0.323$ GeV. The anomalous dimension and $R(\tau)$ profile function cause an increase in the size of the power correction for increasing τ and for increasing Q.

Note that our R-gap subtraction scheme differs from the subtractions in the low-scale effective coupling model of Ref. [35], which is not based on the factorization of the soft large angle radiation but on the assumption that the $\mathcal{O}(\Lambda_{\rm QCD})$ renormalon ambiguity is related entirely to the low-energy behavior of the strong coupling α_s. In the effective coupling model the subtractions involve logarithms $\ln(\mu/\mu_I)$, where μ is the usual renormalization scale of perturbation theory and μ_I is the low-momentum subtraction scale, which is set to $\mu_I = 2$ GeV. The scale μ_I plays a role very similar to the scale R in the R-gap scheme. These logarithms are the analogs of L_R in Eq. (38), and, since $\mu \propto Q$, these logarithms also become large. In the effective coupling model an appropriate resummation formalism for large logs in the subtractions remains an open question.

In Fig. 7 we plot the absolute value of four components of our cross section for our complete QCD result at N^{3}LL$'$ order in the R-gap scheme at $Q = m_Z$. The cross-section

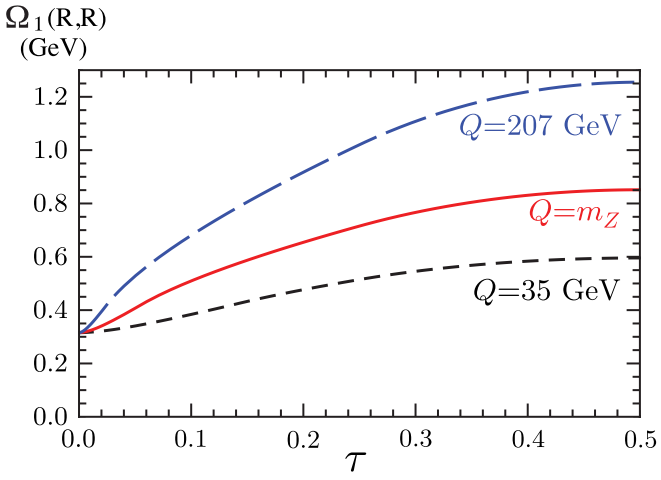

FIG. 6 (color online). The running of $\Omega_1(R, R)$ with $R = R(\tau)$, plotted as a function of τ for $Q = 35, 91.2, 207$ GeV.

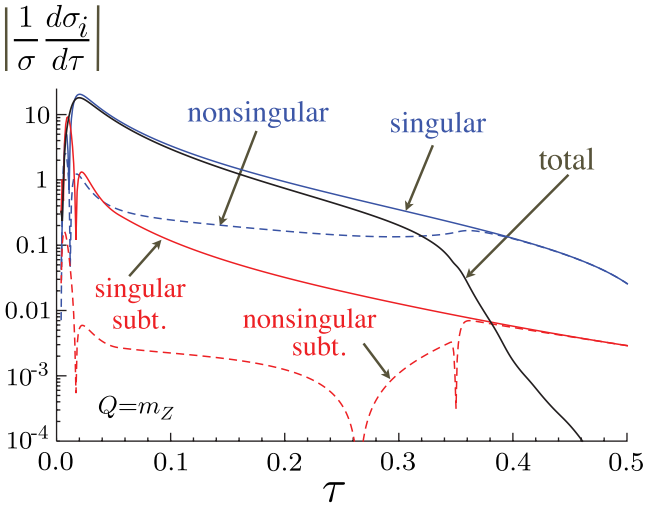

FIG. 7 (color online). Components of the pure QCD cross section. Here $\Omega_1 = 0.35$ GeV and $\alpha_s(m_Z) = 0.114$.

components include the singular terms (solid blue line), nonsingular terms (dashed blue line), and separately the contributions from terms that involve the subtraction coefficients δ_i, for both singular subtractions (solid red line) and nonsingular subtractions (dashed red line). The sum of these four components gives the total cross section (solid black line). The subtraction components are a small part of the cross section in the tail region but have an impact at the level of precision obtained in our computation. In the peak region at very small τ the solid red singular subtraction grows to be the same size as the solid blue singular term and is responsible for yielding a smooth positive definite total cross section. In both the peak and tail regions the singular cross section dominates over the nonsingular cross section. But as we approach the threshold $\tau \sim 1/3$ for the far-tail region they appear with opposite signs and largely cancel. This is clear from the figure where individually the singular and nonsingular lines are larger than the total cross section in this region. The same cancellation occurs for the singular subtraction and nonsingular subtraction terms.

G. Bottom mass effects

In this work we implement bottom mass effects using the SCET factorization framework for massive quarks [14,41]. We include m_b dependence in the kinematics, which starts at tree level, and in the $\mathcal{O}(\alpha_s)$ corrections in the partonic singular and nonsingular distributions. We also account for the resummation of large logs and for hadronization effects in the m_b-dependent terms. The mass dependent factorization theorem implies that the renormalization group summation of logarithms is identical to the one for massless quarks and that all power corrections of type 1 from Eq. (9) are described by the nonperturbative soft function $S_\tau^{\rm mod}$ already defined for the massless case [14,41]. We have already indicated this with the

convolution $\Delta d\hat{\sigma}_b/d\tau \otimes S_\tau^{\rm mod}$ shown in Eq. (4). Since for the numerical analysis in this work we fit to data in the tail region, where $Q\tau > 6$ GeV, and since the massive quark thrust factorization theorem implies for the soft scale $\mu_S \sim Q\tau > 6$ GeV, we do not have to account for any flavor threshold in the renormalization group evolution and can always use $n_f = 5$. The mass dependent factorization theorem further implies that the only nontrivial m_b dependence in the singular distribution arises in the thrust jet function. Thus the jet scale $\mu_J \sim Q\sqrt{\tau} \gg m_b$ for the region of our fit and we use the $\overline{\rm MS}$ bottom mass $\bar{m}_b(\mu_J)$ to parameterize the m_b corrections with $\bar{m}_b(\bar{m}_b) = 4.2$ GeV as our input value. Using the $\overline{\rm MS}$ mass rather than the pole mass avoids the appearance of large higher order effects related to the $\mathcal{O}(\Lambda_{\rm QCD})$ pole mass renormalon.

We implement the partonic bottom mass corrections as an additive term to the massless partonic N^{3}LL$'$ cross section. These corrections come from the production of bottom quarks by the virtual γ or Z:

$$\frac{\Delta d\hat{\sigma}_b}{d\tau} = \frac{d\hat{\sigma}_b}{d\tau} - \frac{d\hat{\sigma}_b^{\bar{m}_b=0}}{d\tau}, \tag{42}$$

where both $d\hat{\sigma}_b/d\tau$ and $d\hat{\sigma}_b^{\bar{m}_b=0}/d\tau$ are computed at NNLL. Because the effect of $\bar{m}_b \neq 0$ in $\Delta d\hat{\sigma}_b/d\tau$ is expected to be a percent level correction to the tail cross section, we anticipate that the NNLL level of precision suffices. (This is also justified *a posteriori* by the relatively small effect of the m_b corrections on our fit results.)

An important aspect in the discussion of the finite quark mass effects is in which way hadron and heavy quark masses need to be accounted for in the definition of thrust in Eq. (1). In the experimental analyses Monte Carlo generators are used to convert the actual measurements to the momentum variables needed to compute τ, and this conversion depends on hadron masses. Since the final-state stable hadrons are light, these effects are related to nonperturbative physics. Theoretically they are therefore implicitly encoded within our fit of the nonperturbative corrections. In the partonic theoretical computation light hadron masses are neglected in the computation of the τ distribution, and it is consistent to set $\sum_i |\vec{p}_i| = Q$ in the denominator of Eq. (1).

To understand how the heavy quark masses affect the definition of thrust in Eq. (1) we recall that the partonic computation relies on the inclusive nature of the measurements and that, experimentally, only light and long-lived hadrons reach the detectors and are accounted for in the $\vec{p}_i$ momenta that enter in computing τ. Thus for heavy hadrons containing bottom (or charm) quarks, it is their light and long-lived hadronic decay products that enter the particle sum $\sum_i$. Because of energy conservation it is therefore necessary to set $\sum_i |\vec{p}_i| = Q$ in the denominator of the thrust definition of Eq. (1) for the leading power partonic computations involving heavy quarks. On the other hand, due to three-momentum conservation, it is consistent to use the heavy quark three-momentum in the numerator of Eq. (1) for the partonic computations. This makes the partonic thrust computations involving heavy quarks simple because we do not need to explicitly account for the heavy quark decay in the calculations. Together with the relation $\sum_i |\vec{p}_i| = Q$ in the denominator of Eq. (1) this induces a shift of the observed thrust distribution for b quarks to larger τ values. Comparing to the massless quark situation, the small-τ end point is moved from 0 to

$$\tau_b^{\rm min} = 1 - \sqrt{1 - 4\bar{m}_b^2/Q^2}, \tag{43}$$

where $\bar{m}_b = \bar{m}_b(\mu_J)$. At tree level this shifts $\delta(\tau) \to \delta(\tau - \tau_b^{\rm min})$. For the fixed-order result at $\mathcal{O}(\alpha_s)$ the three-jet end point is moved from $1/3$ to $\tau_b^{\rm 3jet} = 5/3 - 4/3\sqrt{1 - 3\bar{m}_b^2/Q^2}$. At leading order in $\bar{m}_b^2/Q^2 \ll 1$ we have $\tau_b^{\rm min} = 2\bar{m}_b^2/Q^2 + \mathcal{O}(\bar{m}_b^4/Q^4)$ and $\tau_b^{\rm 3jet} = 1/3 + 2\bar{m}_b^2/Q^2 + \mathcal{O}(\bar{m}_b^4/Q^4)$, so the shift is the same for both end points. Numerically, for $\bar{m}_b = 4.2$ GeV and $Q = (35, 91.2, 207)$ GeV, τ is shifted by $(0.029, 0.004, 0.0008)$. This shift is also observed experimentally in flavor tagged thrust analyses [72–74].

In the following we outline the method used to compute the partonic $d\hat{\sigma}_b/d\tau$. Like for the massless case the distribution is divided into singular and nonsingular parts:

$$\frac{d\hat{\sigma}_b}{d\tau} = \frac{d\hat{\sigma}_b^{\rm s}}{d\tau} + \frac{d\hat{\sigma}_b^{\rm ns}}{d\tau}. \tag{44}$$

The implementation of the bottom mass effects into the singular distribution $d\hat{\sigma}_b^{\rm s}/d\tau$ follows the NLL$'$ analysis in Ref. [41], except that the evolution in the present work is incorporated fully at NNLL order and that the exact partonic threshold at $\tau = \tau_b^{\rm min}$ is accounted for:

$$\begin{aligned}\frac{d\hat{\sigma}_b^{\rm s}}{d\tau} &= Q\sigma_0^b\Big(\frac{\bar{m}_b}{Q}\Big) H_Q^v(Q,\mu_H) U_H(Q,\mu_H,\mu) \\ &\quad\times \int ds ds' J_{\tau b}(s',\bar{m}_b,\mu_J) U_J^\tau(s-s',\mu,\mu_J) \\ &\quad\times \int dk U_S^\tau(k,\mu,\mu_S) e^{-2(\delta(R,\mu_s)/Q)(\partial/\partial\tau)} \\ &\quad\times S_\tau^{\rm part}\Big(Q\tau - Q\tau_b^{\rm min} - \frac{s}{Q} - k, \mu_S\Big) \\ &\quad + (\overline{\rm MS}\text{-pole mass scheme change terms}),\end{aligned} \tag{45}$$

where $\sigma_0^b(x) = \sigma_0^{bv}\sqrt{1-4x^2}(1+2x^2) + \sigma_0^{ba}(1-4x^2)^{3/2}$. Perturbative bottom mass effects in the soft function start at two loops, so at $\mathcal{O}(\alpha_s)$ $S_\tau^{\rm part}$ remains unchanged. Since we have $\bar{m}_b/Q \ll 1$, only the thrust jet function for bottom quark production, $J_{\tau b}(s,\bar{m}_b,\mu)$ [75], receives modifications from the finite m_b. These modifications lead to a shift of the partonic threshold of the thrust jet function from invariant mass $p^2 = 0$ to $p^2 = \bar{m}_b^2$. In $J_{\tau b}(s,\bar{m}_b,\mu)$ the variable $s = p^2 - \bar{m}_b^2$, and the presence of the mass leads

to $\tau_b^{\min}$ in Eq. (45). It also gives a more complicated form for $\mathcal{O}(\alpha_s)$ corrections in $J_{\tau b}$ involving regular functions of m_b^2/s in addition to singular terms $\propto \delta(s)$ and $[\ln^k(s/\mu^2)/(s/\mu^2)]_+$ familiar from the massless quark jet function. More details and explicit formulas can be found in Refs. [14,41].

The bottom quark mass effects in the nonsingular partonic distribution $d\hat{\sigma}_b^{\rm ns}/d\tau$ are more complicated since finite mass effects at $\mathcal{O}(\alpha_s)$ differ for vector and axial-vector current induced jet production:

$$\frac{d\hat{\sigma}_b^{\rm ns}}{d\tau} = e^{-2(\delta(R,\mu_s)/Q)(\partial/\partial\tau)}\Big[\sigma_0^{bv} f_b^v\Big(\tau, \frac{\bar{m}_b}{Q}, \frac{\mu_{\rm ns}}{Q}\Big) + \sigma_0^{ba} f_b^a\Big(\tau, \frac{\bar{m}_b}{Q}, \frac{\mu_{\rm ns}}{Q}\Big)\Big] + (\overline{\rm MS}\text{-pole mass scheme change terms}). \quad (46)$$

In our analysis we implement analytic expressions for the nonsingular functions f_b^v and f_b^a. The full $\mathcal{O}(\alpha_s)$ distributions for $\tau > 0$ can be obtained from integrating the known double differential $b\bar{b}$ energy distribution for vector-induced and axial-vector-induced production, respectively; see e.g. Refs. [76,77].[9] The corresponding $\mathcal{O}(\alpha_s)$ coefficient of the $\delta(\tau - \tau_b^{\min})$ term is obtained using the one-loop correction to the total $b\bar{b}$ cross section as a constraint. To determine the nonsingular distributions $f_b^{v,a}$ we proceed much like for the massless case and subtract the singular contributions expanded to $\mathcal{O}(\alpha_s)$ from the full $\mathcal{O}(\alpha_s)$ distribution. Further details and explicit formulas for $f_b^{v,a}$ will be given in a future publication.

H. QED corrections

For the electroweak corrections to the thrust distribution we can distinguish purely weak contributions and QED effects. The dominant effects to jet production from the purely weak interactions are given by virtual one-loop corrections to the hard Wilson coefficient H_Q. Since the contribution of the singular thrust distribution $d\hat{\sigma}_s/d\tau$ dominates in the τ ranges we use for our fits as well as in the total cross section $\sigma_{\rm tot} = \int d\tau d\sigma/d\tau$ (see Fig. 7), the purely weak corrections largely drop out when the distribution is normalized to the total cross section. This is consistent with the explicit computations carried out in Refs. [43,44], where purely weak corrections were found to be tiny. In our analysis we therefore neglect purely weak loop effects.

For QED corrections the situation is more complicated because, apart from virtual effects which again largely cancel in the normalized distribution, one also has corrections due to initial-state and final-state radiation. In addition, one has to account for the fact that the treatment of QED effects in the thrust measurements depends on the experiment. In general, using Monte Carlo simulations, all experimental data were corrected to eliminate the effects from initial-state radiation. However, they differ concerning the treatment of final-state photon corrections, which were either eliminated or included in the corrected data sets. In Sec. VI we review information on the approach followed by the various experimental collaborations. Since many experiments did not remove final-state radiation, we have configured a version of our code that adds final-state photons and QED Sudakov effects and does so on an experiment by experiment basis. A parametric estimate of the potential impact of these QED effects on the measurement of $\alpha_s(m_Z)$ is $\sim -0.244\alpha_{\rm em}/(C_F\alpha_s) \sim -1\%$, where 0.244 is the average of the square of the electromagnetic charges for the five lightest flavors.

We implement the leading set of QED corrections to all components that go into the main factorization formula of Eq. (4) in the massless quark limit counting $\alpha_{\rm em} \sim \alpha_s^2$ to make a correspondence with Table II and remembering to include cross terms such as terms of $\mathcal{O}(\alpha_{\rm em}\alpha_s)$. Exceptions where QED corrections are not included are the gap subtraction $\delta(R, \mu_S)$ and the R-evolution equation for the gap parameter $\bar{\Delta}$. This is because QED effects do not lead to $\mathcal{O}(\Lambda_{\rm QCD})$ infrared renormalon ambiguities. Most of the required QED results can be obtained in a straightforward manner from modifications of the known QCD corrections.

Our implementation of QED effects is briefly described as follows: For the evolution of the strong coupling we included the $\mathcal{O}(\alpha_s^2\alpha_{\rm em})$ corrections to the QCD beta function. There are also effects from the evolution of the QED coupling $\alpha_{\rm em}(\mu)$ which we define in the $\overline{\rm MS}$ scheme. In the beta function for the QED coupling $\alpha_{\rm em}$ we account for the dominant $\mathcal{O}(\alpha_{\rm em}^2)$ and the next-to-leading $\mathcal{O}(\alpha_{\rm em}^2\alpha_s)$ contributions. For the full singular partonic distribution which includes both QCD and QED effects we have

$$\frac{d\hat{\sigma}_{\rm s}}{d\tau} = Q\sum_I \sigma_0^I H_Q^I(Q, \mu_H) U_H^I(Q, \mu_H, \mu) \times \int ds ds' J_\tau^I(s', \mu_J) U_J^{\tau I}(s - s', \mu, \mu_J) \times \int dk U_S^{\tau I}(k, \mu, \mu_S) e^{-2(\delta(R,\mu_s)/Q)(\partial/\partial\tau)} \times S_\tau^{{\rm part}I}\Big(Q\tau - \frac{s}{Q} - k, \mu_S\Big), \quad (47)$$

where all factors now depend on the index I due to their dependence on the electromagnetic charges $q^{I=uv,ua} = +2/3$ and $q^{I=dv,da,bv,ba} = -1/3$. We implement one-loop QED corrections in the hard factor H_Q^I, the jet function J_τ^I, and the soft functions $S_\tau^{{\rm part}I}$. In the renormalization group evolution factors U_H^I, $U_J^{\tau I}$, and $U_S^{\tau I}$ we account for the one-loop QED corrections to the cusp and the noncusp anomalous dimensions. In the nonsingular partonic distribution $d\hat{\sigma}_{\rm ns}/d\tau$ the same approach is employed. Here the

[9] Results for bottom mass corrections at $\mathcal{O}(\alpha_s^2)$ were determined in Refs. [78–80] but are not used in our analysis due to the small effect the bottom mass corrections have in our fits.

$\mathcal{O}(\alpha_{\rm em})$ contributions that are analogous to the $\mathcal{O}(\alpha_s)$ terms are included by writing the full functions f^I to be used in Eq. (26) as

$$f^I\left(\tau, \frac{\mu_{\rm ns}}{Q}\right) = f^I_{\rm qcd}\left(\tau, \frac{\mu_{\rm ns}}{Q}\right) + \frac{3\alpha(\mu)(q^I)^2}{8\pi} f_1(\tau). \quad (48)$$

The 1% parametric estimate and the moderate size of the QED effects we observe from the results of our fits justifies the neglect of higher order QED effects. A more precise treatment of QED effects is also not warranted given the level of accuracy of the Monte Carlo generators used to correct the experimental data. More details and explicit formulas for the QED corrections discussed here will be given in a future publication.

III. PROFILE FUNCTIONS

The factorization formula for the singular partonic distribution $d\hat{\sigma}_s/d\tau$ in Eq. (11) is governed by three renormalization scales: the hard scale μ_H, the jet scale μ_J, and the soft scale μ_S. To avoid large logarithms appearing in the corrections to the hard coefficient H_Q, the jet function J_τ, and the soft function S_τ, the corresponding scales must satisfy the following theoretical constraints in the three τ regions:

$$\begin{aligned}
&\text{(1) peak:} && \mu_H \sim Q, && \mu_J \sim \sqrt{\Lambda_{\rm QCD} Q}, && \mu_S \gtrsim \Lambda_{\rm QCD};\\
&\text{(2) tail:} && \mu_H \sim Q, && \mu_J \sim Q\sqrt{\tau}, && \mu_S \sim Q\tau;\\
&\text{(3) far tail:} && \mu_H = \mu_J = \mu_S \sim Q. && && (49)
\end{aligned}$$

In the peak region, where the full nonperturbative function $S^{\rm mod}_\tau$ is relevant we have $\mu_H \gg \mu_J \gg \mu_S \sim \Lambda_{\rm QCD}$. In the tail region, where the nonperturbative effects are described by a series of moments of the soft function we have $\mu_H \gg \mu_J \gg \mu_S \gg \Lambda_{\rm QCD}$. To achieve an accurate theoretical description, we resum logarithms of τ in the peak and tail regions where μ_H, μ_J, and μ_S are separated. Finally, in the far-tail region the partonic contributions are described by usual fixed-order perturbation theory, and a proper treatment of fixed-order multijet thresholds requires that the three μ parameters merge close together in the far-tail region and become equal at $\tau = 0.5$, with $\mu_H = \mu_J = \mu_S \sim Q \gg \Lambda_{\rm QCD}$. Thus in the far-tail region logarithms of τ are not summed. The merging of μ_H, μ_J, and μ_S in the far-tail region is of key importance for the cancellations between singular and nonsingular cross sections shown in Fig. 7. To obtain a continuous factorization formula that is applicable in all three regions we use τ-dependent renormalization scales, which we call *profile functions*. These are smooth functions of τ which satisfy the theoretical constraints listed in Eq. (49).

In addition to the three renormalization scales of the singular partonic distribution there are two more scales: $\mu_{\rm ns}$ and R. The renormalization scale $\mu_{\rm ns}$ governs the perturbative series for the function f^I contained in the nonsingular partonic distribution $d\hat{\sigma}_{\rm ns}/d\tau$. The subtraction scale R arises when we implement the gap subtractions in the R-gap scheme for Ω_1 that remove the $\mathcal{O}(\Lambda_{\rm QCD})$ renormalon contained in the $\overline{\rm MS}$ soft function. This R also corresponds to the end point of the R evolution for $\bar{\Delta}(R, \mu_S)$ given in Eq. (41). To avoid large logarithms in the subtraction $\delta(R, \mu_S)$, the value of R needs to be chosen of order μ_S and is therefore also a function of τ.

The factorization formula (4) is formally invariant under $\mathcal{O}(1)$ changes of the profile function scales, that is, changes that do not modify the hierarchies. The residual dependence on the choice of profile functions constitutes one part of the theoretical uncertainties and provides a method to estimate higher order perturbative corrections. We adopt a set of six parameters that can be varied in our theory error analysis which encode this residual freedom while still satisfying the constraints in Eq. (49).

For the profile function at the hard scale, we adopt

$$\mu_H = e_H Q, \quad (50)$$

where e_H is a free parameter which we vary from $1/2$ to 2 in our theory error analysis.

For the soft profile function we use the form

$$\mu_S(\tau) = \begin{cases} \mu_0 + \frac{b}{2t_1}\tau^2, & 0 \le \tau \le t_1, \\ b\tau + d, & t_1 \le \tau \le t_2, \\ \mu_H - \frac{b}{1-2t_2}\left(\frac{1}{2} - \tau\right)^2, & t_2 \le \tau \le \frac{1}{2}. \end{cases} \quad (51)$$

Here, t_1 and t_2 represent the borders between the peak, tail, and far-tail regions. μ_0 is the value of μ_S at $\tau = 0$. Since the thrust value where the peak region ends and the tail region begins is Q-dependent, we define the Q-independent parameter $n_1 = t_1(Q/1\ {\rm GeV})$. To ensure that $\mu_S(\tau)$ is a smooth function, the quadratic and linear forms are joined by demanding continuity of the function and its first derivative at $\tau = t_1$ and $\tau = t_2$, which fixes $b = 2(\mu_H - \mu_0)/(t_2 - t_1 + \frac{1}{2})$ and $d = [\mu_0(t_2 + \frac{1}{2}) - \mu_H t_1]/(t_2 - t_1 + \frac{1}{2})$. In our theory error analysis we vary the free parameters n_1, t_2, and μ_0.

The profile function for the jet scale is determined by the natural relation between the hard, jet, and soft scales:

$$\mu_J(\tau) = (1 + e_J(\tfrac{1}{2} - \tau)^2)\sqrt{\mu_H \mu_S(\tau)}. \quad (52)$$

The term involving the free $\mathcal{O}(1)$ parameter e_J implements a modification to this relation and vanishes in the multijet region where $\tau = 1/2$. We use a variation of e_J to include the effect of such modifications in our estimation of the theoretical uncertainties.

For the subtraction scale R the choice $R = \mu_S(\tau)$ ensures that we avoid large logarithms in the $\delta_i(R, \mu_S)$ subtractions for the soft function. In the peak region, however, it is convenient to deviate from this choice so that the $\mathcal{O}(\alpha_s)$ subtraction term $\delta_1(R, \mu_S) = -0.848\,826 \ln(\mu_S/R)$ is nonzero [see Eq. (38)]. We therefore use the form

$$R(\tau) = \begin{cases} R_0 + \mu_1\tau + \mu_2\tau^2, & 0 \le \tau \le t_1, \\ \mu_S(\tau), & t_1 \le \tau \le 0.5. \end{cases} \quad (53)$$

Imposing continuity of $R(\tau)$ and its first derivative at $\tau = t_1$ requires $\mu_1 = (2d - 2R_0 + bt_1)/t_1$ and $\mu_2 = (-d + R_0)/t_1^2$. The only free parameter is R_0, which sets the value of R at $\tau = 0$. We take $R_0 = 0.85\mu_0$ to give the one-loop subtraction $\delta_1(R, \mu_S)$ the appropriate sign to cancel the renormalon in the peak region. Since our focus here is not the peak region, we leave further discussion of the appropriate choice of R_0 to a future publication.

In our theory error analysis we vary $\mu_{\rm ns}$ to account for our ignorance on the resummation of logarithms of τ in the nonsingular corrections. We account for the possibilities

$$\mu_{\rm ns}(\tau) = \begin{cases} \mu_H, & n_s = 1, \\ \mu_J(\tau), & n_s = 0, \\ \frac{1}{2}(\mu_J(\tau) + \mu_S(\tau)), & n_s = -1. \end{cases} \quad (54)$$

We do not include the choice $\mu_{\rm ns} = \mu_S$ since we find that the choice of this small scale enhances the nonsingular contributions in an unnatural way.

In total, we have introduced six free parameters which we vary to account for renormalization scale uncertainties. In our analysis we use the following central values and variations: $\mu_0 = 2^{+0.5}_{-0.5}$ GeV, $n_1 = 5^{+3}_{-3}$, $t_2 = 0.25^{+0.05}_{-0.05}$, $e_J = 0^{+1}_{-1}$, $e_H = 2^h$ with $h = 0^{+1}_{-1}$, and $n_s = (-1, 0, 1)$. In Fig. 8 we show the form of the profile functions for $Q = m_Z = 91.2$ GeV and all profile parameters at their central values. The dashed lines represent the functions $Q\sqrt{\tau}$ and $Q\tau$ which were the central choices for $\mu_J(\tau)$ and $\mu_S(\tau)$ used in Ref. [20] but which do not meet in the multijet region. In order for our profile for $\mu_S(\tau)$ to join smoothly onto μ_H and $\mu_J(\tau)$ it is necessary for $\mu_S(\tau)$ to have a slope $\sim 2Q\tau$ in the tail region. Since ln(2) is not large our profiles sum the same lnτ's as with the choice in Ref. [20] but satisfy the criteria necessary to treat the multijet thresholds.[10]

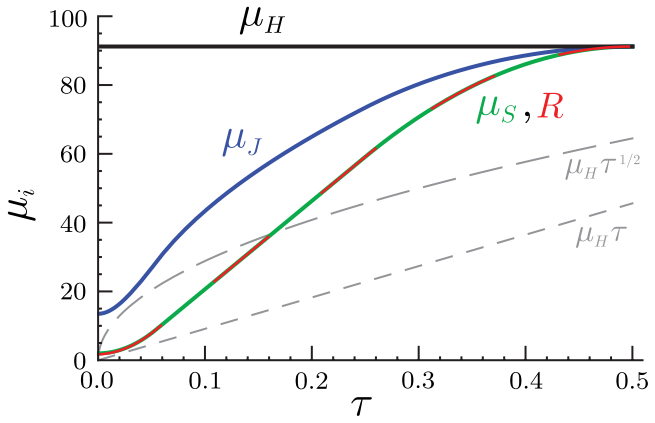

FIG. 8 (color online). Profile functions for the renormalization scales $\mu_J(\tau)$ and $\mu_S(\tau)$ and subtraction scale $R(\tau)$ that appear in the factorization theorem. Shown are results for the central parameter values at $Q = m_Z$.

IV. NONPERTURBATIVE MODEL FUNCTION

The soft nonperturbative function $S_\tau^{\rm mod}(k)$ parameterizes the dominant nonperturbative hadronic effects in the thrust distribution. It describes the hadronization contributions that arise from how soft hadrons that are radiated in between the jets enter the thrust variable in Eq. (1). It is normalized, has the property $S_\tau(0) = 0$, is positive definite, and has support for $k \ge 0$. To keep the representation of $S_\tau^{\rm mod}$ as much as possible independent of a particular analytic parametrization we adopt the approach of Ref. [38] and write the soft nonperturbative function as a linear combination of an infinite set of basis functions which can in principle describe any function with the properties mentioned above. The model function we use has the form

$$S_\tau^{\rm mod}(k, \lambda, \{c_i\}) = \frac{1}{\lambda}\Big[\sum_{n=0}^{N} c_n f_n\Big(\frac{k}{\lambda}\Big)\Big]^2, \quad (55)$$

where the basis functions are [38]

$$f_n(z) = 8\sqrt{\frac{2z^3(2n+1)}{3}}e^{-2z}P_n(g(z)),$$
$$g(z) = \frac{2}{3}(3 - e^{-4z}(3 + 12z + 24z^2 + 32z^3)) - 1, \quad (56)$$

and P_n are Legendre polynomials. For $\sum_i c_i^2 = 1$ the norm of $S_\tau^{\rm mod}(k)$ is unity: $\Omega_0 = 1$. The choice of basis in Eqs. (55) and (56) depends on specifying one dimensionful parameter λ which is characteristic of the width of the soft function. With $N = \infty$ the parameter λ would be redundant, but in practice we truncate the sum in Eq. (55) at a finite N, and then λ is effectively an additional parameter of the model function.

In this work we fit to experimental thrust data in the tail region where the predominant effects of the soft model function are described by its first moment $\Omega_1(\lambda, \bar{\Delta}, \{c_i\})$. As explained below, we use the second moment $\Omega_2(\lambda, \bar{\delta}, \{c_i\})$ to validate our error analysis and confirm the validity of neglecting this parameter in the fit. Since in the tail region the exact form of the soft model function is not relevant, we take $N = 2$ setting $c_{n>2} = 0$. Variations of the parameter c_1 are highly correlated with variations of λ and are hence not necessary for our purposes, so we set $c_1 = 0$. For this case

[10] In Ref. [23] where NLL resummation is achieved by exponentiation, the log resummation is turned off at a predefined threshold $\tau_{\rm max}$ with the log-R method [21]. In this approach the transition to fixed order results in the multijet region is linear and hence different from ours.

$$\Omega_1 = \bar{\Delta} + \frac{\lambda}{2}[c_0^2 + 0.201\,354 c_0 c_2 + 1.100\,31 c_2^2],$$
$$\Omega_2 = \bar{\Delta}^2 + \bar{\Delta}\lambda[c_0^2 + 0.201\,354 c_0 c_2 + 1.100\,31 c_2^2] + \frac{\lambda^2}{4}[1.25 c_0^2 + 1.036\,21 c_0 c_2 + 1.788\,59 c_2^2], \quad (57)$$

and the normalization condition $c_0^2 + c_2^2 = 1$ can be used to eliminate $c_0 > 0$. Recall that in the soft model function in the factorization theorem we must use $S_\tau^{\rm mod}(k - 2\bar{\Delta}(R, \mu_S), \lambda, \{c_i\})$, where $R = R(\tau)$ and $\mu_S = \mu_S(\tau)$ are determined by the profile functions. When we quote numbers for parameters we use $\bar{\Delta} = \bar{\Delta}(R_\Delta, \mu_\Delta)$ and hence $\Omega_{1,2} = \Omega_{1,2}(R_\Delta, \mu_\Delta)$ with reference scales $\mu_\Delta = R_\Delta = 2$ GeV. The running between the scales (R, μ_S) and (R_Δ, μ_Δ) is determined by Eq. (41).

For our default fit in the tail region only the parameter Ω_1 is numerically relevant so without loss of generality we can take $c_0 = 1$ and $c_2 = 0$ and set $\bar{\Delta}(R_\Delta, \mu_\Delta) = 0.05$ GeV. In this case all higher moments $\Omega_{n>1}$ are determined as a function of Ω_1 and $\bar{\Delta}$. For example, we have $\Omega_2 = (\bar{\Delta}^2 - 2\bar{\Delta}\Omega_1 + 5\Omega_1^2)/4$ for the second moment.

In Sec. VII we analyze the dependence of our fit results on changes of Ω_2. Because c_2 has a rather strong correlation to Ω_2, we implement these Ω_2 variations by using Eq. (57) and setting c_2 to nonzero values. In this case we can hold Ω_1 fixed by a suitable choice of λ for a given c_2.

To obtain results from our code that do not include nonperturbative corrections we can simply turn them off by setting $S_\tau^{\rm mod}(k) = \delta(k)$ and $\bar{\Delta} = \delta = 0$.

V. NORMALIZATION AND CONVERGENCE

The experimental data are normalized to the total number of events. In our prediction we therefore need to normalize the distribution to the total cross section; i.e. we have to calculate $(1/\sigma)d\sigma/d\tau$. Since the factorization formula in Eq. (4) is valid for all thrust values we have the option to use either the integral of our $d\sigma/d\tau$ distribution for the norm or the available fixed-order result for the total hadronic cross section.

The fixed-order total cross section is

$$\sigma_{\rm tot}^{\rm FO} = \sum \sigma_0^I R^I, \qquad R^{uv} = R^{dv} = R^{ua} = R^{da} = R_{\rm Had},$$
$$R^{ba} = R_{\rm Had} + R_A + \frac{\alpha_s^2}{3\pi^2} I(r_t), \qquad R^{bv} = R_{\rm Had} + R_V. \quad (58)$$

Here $R_{\rm Had}$ is the pure QCD cross section for massless quarks, $R_{A,V}$ are mass corrections depending on m_b/Q, and $I(r_t)$ is the isosinglet correction from the axial anomaly and large top-bottom mass splitting [56]. Setting $\mu = Q$ the QCD cross sections for massless quarks at three loops is

$$R_{\rm Had} = 1 + 0.318\,309\,9\alpha_s(Q) + 0.142\,784\,9\alpha_s^2(Q) - 0.411\,757\alpha_s^3(Q). \quad (59)$$

We refer to the review in Ref. [81] for a discussion of the fixed-order hadronic cross section. We note that the α_s series for the fixed-order hadronic cross section exhibits an excellent and fast convergence. At $\mathcal{O}(\alpha_s^3)$ the perturbative uncertainty is much below the per mille level and hence entirely negligible for the purpose of our analysis.

In the R-gap scheme in pure QCD, from a numerical analysis at $Q = m_Z$, we find at N^{3}LL$'$ order that the integrated norm of the thrust distribution for the default setting of all theory parameters (see Table III) gives about $0.99\sigma_{\rm tot}^{\rm FO}$ at $\mathcal{O}(\alpha_s^3)$. However, we also find that the perturbative uncertainty of the integrated norm (determined by the theory scan as described in Sec. VI) is about $\pm 2.5\%$, which is substantially larger than for the fixed-order cross section. This larger uncertainty is due to the perturbative errors of the thrust distribution in the peak region. At N^{3}LL$'$ order we therefore employ the fixed-order cross section to normalize the thrust distribution we use for the fits.

At the lower orders in the R-gap scheme (N^{3}LL, NNLL$'$, NNLL, and NLL$'$) we find that the integrated norm for central theory parameters is more appropriate since the order-by-order convergence to $\sigma_{\rm tot}^{\rm FO}$ is substantially slower than that of the rapid converging fixed-order QCD result in Eq. (59). Again we find that the large perturbative uncertainties in the peak region render the perturbative errors of the integrated norm larger than those of the fixed-order norm. We therefore evaluate the integrated norms at the lower orders with the theory parameters fixed at their default values (see Table III). This means that to estimate the theoretical errors in our fits to experimental data at orders below N^{3}LL$'$ in the R-gap scheme, we vary the theory parameters only for the distribution and not for the norm computation. In the $\overline{\rm MS}$ scheme for $\bar{\Omega}_1$ we also

TABLE III. Theory parameters relevant for estimating the theory uncertainty, their default values, and the range of values used for the theory scan during the fit procedure.

Parameter	Default value	Range of values
μ_0	2 GeV	1.5 to 2.5 GeV
n_1	5	2 to 8
t_2	0.25	0.20 to 0.30
e_J	0	-1, 0, 1
e_H	1	0.5 to 2.0
n_s	0	-1, 0, 1
s_2	-39.1	-36.6 to -41.6
$\Gamma_3^{\rm cusp}$	1553.06	-1553.06 to $+4659.18$
j_3	0	-3000 to $+3000$
s_3	0	-500 to $+500$
ϵ_2	0	-1, 0, 1
ϵ_3	0	-1, 0, 1

adopt the integrated norm at all orders. When we evaluate the thrust distribution with log resummation but without nonperturbative effects we use the same normalization choices as for the R-gap scheme, which makes comparison to earlier work in Sec. IX easier. For the situation where the cross section is evaluated at fixed order, without resummation or nonperturbative effects, we use the appropriate fixed-order normalization at each order.

As discussed in Sec. VI, to compare with the binned experimental data we integrate our theoretical expression for the distribution $(1/\sigma)(d\sigma/d\tau)$ over each bin $[\tau_1, \tau_2]$. A potential alternative is to use theoretical results for the cumulant

$$\Sigma(\tau) = \int_0^\tau d\tau' \frac{1}{\sigma}\frac{d\sigma}{d\tau}(\tau'). \tag{60}$$

Here one sums large logs of τ rather than τ', and the SCET-based cumulant has τ-dependent profiles $\Sigma(\tau, \mu_i(\tau))$. The presence of $\mu_i(\tau)$ implies that the derivative of the cumulant is not precisely equal to the distribution:

$$\frac{d}{d\tau}\Sigma(\tau, \mu_i(\tau)) = \frac{1}{\sigma}\frac{d\sigma}{d\tau}(\tau, \mu_i(\tau)) + \frac{d\mu_i(\tau)}{d\tau} \times \frac{\partial}{\partial\mu_i}\int_0^\tau d\tau' \frac{d\sigma}{d\tau'}(\tau', \mu_i(\tau)). \tag{61}$$

The difference coming from the second term in Eq. (61) can be numerically important for certain observables. To test this we consider using for the cross section integrated over the bin $[\tau_1, \tau_2]$ the theoretical expression

$$\Sigma(\tau_2, \mu_i(\tilde\tau_2)) - \Sigma(\tau_1, \mu_i(\tilde\tau_1)), \tag{62}$$

and will examine several choices for $\tilde\tau_{1,2}$.

One simple possibility is to use $\tilde\tau_1 = \tau_1$ and $\tilde\tau_2 = \tau_2$, so that $\Sigma(\tau_2, \mu_i(\tau_2)) - \Sigma(\tau_1, \mu_i(\tau_1))$ is used. In this case there is a spurious contribution from outside the $[\tau_1, \tau_2]$ bin associated to the second term in Eq. (61):

$$\Sigma(\tau_1, \mu_i(\tau_2)) - \Sigma(\tau_1, \mu_i(\tau_1)) \simeq (\tau_2 - \tau_1)\frac{d\mu_i(\tau_1)}{d\tau}\frac{\partial}{\partial\mu_i}\int_0^{\tau_1} d\tau' \frac{d\sigma}{d\tau'}(\tau', \mu_i(\tau_1)), \tag{63}$$

where the $\simeq$ holds under the approximation that the derivatives do not change very much across the bin. With our default setup the deviation of this simple choice for the cumulants from our integrated result for the distribution is 2%–8% for $\tau \in [0.1, 0.3]$, bin size $\tau_2 - \tau_1 = 0.01$, and $Q = 91.2$ GeV.[11] In the far-tail region $\tau_1 \in [0.3, 0.45]$, where the cross section becomes small, the deviation grows from 8% to 1000%. These deviations are dominated by the spurious contribution. The size of the spurious contribution is not reduced by increasing the bin size to $\tau_2 - \tau_1 = 0.05$ and is only mildly dependent on Q. Any choice in Eq. (62) where $\tilde\tau_1 \neq \tilde\tau_2$ leads to a spurious contribution from $\tau \in [0, \tau_1]$.

If we instead use $\tilde\tau_1 = \tilde\tau_2 = (\tau_1 + \tau_2)/2$, then the spurious contribution is identically zero. In this case the difference between Eq. (62) and our integrated thrust distribution is reduced to 0.5% for $\tau_1 \in [0.1, 0.3]$ and for $\tau_1 \in [0.3, 0.45]$ grows from 0.5% to only 20%. Although dramatically reduced, the difference to the integrated distribution in the far-tail region is still quite sizable. This discrepancy occurs because only for the distribution $(1/\sigma)(d\sigma/d\tau)$ can the $\mu_i(\tau)$ profile functions be constructed such that they satisfy exactly the multijet region criteria discussed in Sec. III. Because of the above issues, and since the binned data sets are intended as representations of the thrust distribution, we have determined that our approach of integrating the thrust distribution is conceptually the best.

In the rest of this section we discuss the perturbative behavior of the thrust distribution in the tail region. The values of the physical parameters used in our numerical analysis are collected in Eq. (A4). For our lower order fits we always use the four-loop beta function in the running of the strong coupling constant, as mentioned in the caption of Table II. Furthermore, we always consider five active flavors in the running and do not implement bottom threshold corrections, since our lowest scale in the profile functions (the soft scale μ_S) is never smaller than 6 GeV in the tail where we perform our fit.

In Fig. 9 we display the normalized thrust distribution in the tail thrust range $0.15 < \tau < 0.30$ at the different orders taking $\alpha_s(m_Z) = 0.114$ and $\Omega_1(R_\Delta, \mu_\Delta) = 0.35$ GeV as reference values and neglecting m_b and QED corrections. We display the case $Q = m_Z$ where the experimental measurements from LEP-I have the smallest statistical uncertainties. The qualitative behavior of the results agrees with other c.m. energies. The colored bands represent the theoretical errors of the predictions at the respective orders, which have been determined by the scan method described in Sec. VI.

In Fig. 9(a) we show the $\mathcal{O}(\alpha_s)$ (light/yellow), $\mathcal{O}(\alpha_s^2)$ (medium/purple), and $\mathcal{O}(\alpha_s^3)$ (dark/red) fixed-order thrust distributions without summation of large logarithms. The common renormalization scale is chosen to be the hard scale μ_H. In the fixed-order results the higher order corrections are quite large and our error estimation obviously underestimates the theoretical uncertainty of the fixed-order predictions. This panel including the error bands is very similar to the analogous figures in Refs. [4,6]. This emphasizes the importance of summing large logarithms.

In Fig. 9(b) the fully resummed thrust distributions at NLL′ (yellow), NNLL (green), NNLL′ (purple), N^{3}LL (blue), and N^{3}LL′ (red) order are shown but without implementing the soft nonperturbative function $S_\tau^{\rm mod}$ or the renormalon subtractions related to the R-gap scheme.

[11] For the profile functions used by Becher and Schwartz [20], discussed in Sec. IX, this deviation has similar size but opposite sign.

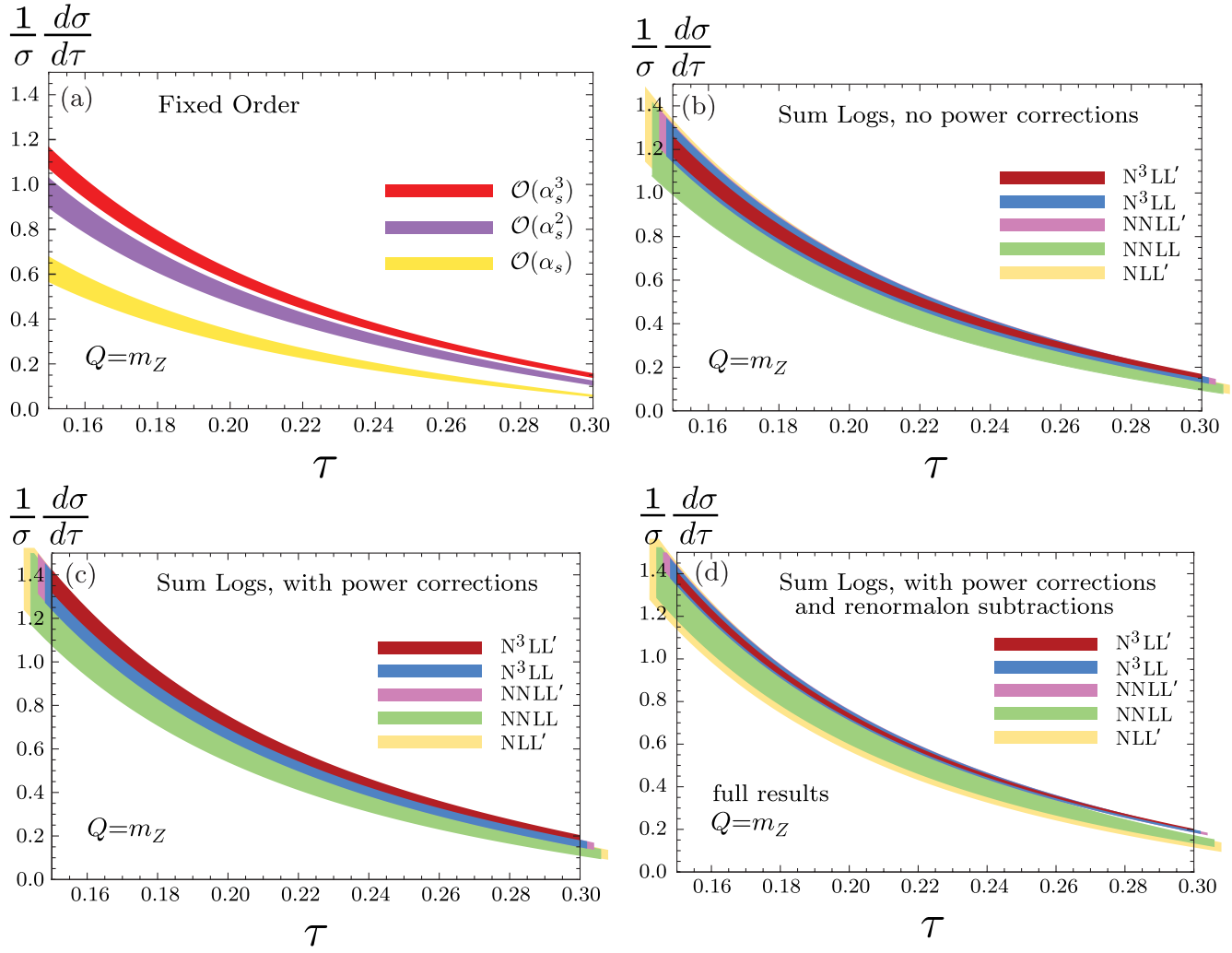

FIG. 9 (color online). Theory scan for errors in pure QCD with massless quarks. The panels are (a) fixed-order, (b) resummation with no nonperturbative function, (c) resummation with a nonperturbative function using the $\overline{\text{MS}}$ scheme for $\bar{\Omega}_1$ without renormalon subtraction, and (d) resummation with a nonperturbative function using the R-gap scheme for Ω_1 with renormalon subtraction.

The yellow NLL′ error band is mostly covered by the green NNLL order band, and similarly the purple NNLL′ band is covered by the blue N^{3}LL one. Moreover the blue N^{3}LL band is within the purple NNLL band. Compared to the fixed-order results, the improvement coming from the systematic summation of large logarithms is obvious. In particular, we see that our way of estimating theoretical uncertainties is appropriate once the logarithms are properly summed. At N^{3}LL and at N^{3}LL′ order the relative uncertainties of these resummed thrust distributions in the tail region $\tau \in [0.1, 0.3]$ are about $\pm 7.8\%$ and $\pm 4.6\%$, respectively.

The results shown in Fig. 9(c) are very similar to Fig. 9(b) but now include also the soft nonperturbative function S_τ^{mod} without renormalon subtractions, where $\bar{\Omega}_1$ is defined in the $\overline{\text{MS}}$ scheme. In the tail region the soft nonperturbative function leads to a horizontal shift of the distribution towards larger thrust values by an amount $\delta\tau \propto 2\bar{\Omega}_1/Q$. This is clearly visible by comparing the values at $\tau = 0.15$ where the curves intersect the y axis. Concerning the uncertainty bands and the behavior of predictions at the different orders the results are very similar to those in Fig. 9(b).

Finally, in Fig. 9(d) we show the results with summation of large logarithms including the soft model function with renormalon subtractions, where Ω_1 is defined in the R-gap scheme. In the R-gap scheme the convergence of perturbation theory is improved, and correspondingly the size of the uncertainties from the same variation of the theory parameters is decreased. The decrease of the uncertainties is clearly visible comparing the blue N^{3}LL and the red N^{3}LL′ uncertainty bands with Fig. 9(c). The relative uncertainties of the thrust distribution at N^{3}LL and at N^{3}LL′ order in the tail region $\tau \in [0.1, 0.3]$ are now about $\pm 3.4\%$ and $\pm 1.7\%$, respectively. This improvement illustrates the numerical impact of the $\mathcal{O}(\Lambda_{\text{QCD}})$ renormalon contained in the partonic soft function and shows the importance of eliminating the $\mathcal{O}(\Lambda_{\text{QCD}})$ renormalon.

VI. EXPERIMENTAL DATA AND FIT PROCEDURE

Experimental data for thrust are available for various c.m. energies Q between 14 and 207 GeV. In our analysis we fit the factorization formula (4) in the tail region to extract α_s and Ω_1. As our default data set we use the thrust range $6/Q \leq \tau \leq 0.33$, and we only employ data from $Q \geq 35$ GeV. The lower boundary $6/Q$ removes data in the peak where higher order moments $\Omega_{i\geq 2}$ become important, while the upper boundary of 0.33 removes data in the far-tail region where the $\alpha_s \Lambda_{\rm QCD}/Q$ power corrections become more important. We take $Q \geq 35$ GeV since a more sophisticated treatment of b quark effects is required at lower energies. The data we use are from TASSO with $Q = \{35, 44\}$ GeV [82], AMY with $Q = 55.2$ GeV [83], JADE with $Q = \{35, 44\}$ GeV [84], SLD with $Q = 91.2$ GeV [85], L3 with $Q = \{41.4, 55.3, 65.4, 75.7, 82.3, 85.1, 91.2, 130.1, 136.1, 161.3, 172.3, 182.8, 188.6, 194.4, 200.0, 206.2\}$ GeV [72,86], DELPHI with $Q = \{45, 66, 76, 89.5, 91.2, 93, 133, 161, 172, 183, 189, 192, 196, 200, 202, 205, 207\}$ GeV [87–90], OPAL with $Q = \{91, 133, 161, 172, 177, 183, 189, 197\}$ GeV [91–93], and ALEPH with $Q = \{91.2, 133, 161, 172, 183, 189, 200, 206\}$ GeV [94]. (For TASSO and AMY we have separated statistical and systematic errors using information from the experimental papers.) All data are given in binned form, and we therefore integrate Eq. (4) over the same set of bins to obtain appropriate theory results for the fit to the experimental numbers. For the case that either $\tau = 6/Q$ or $\tau = 0.33$ are located within an experimental bin, that bin is excluded from the data set if more than half of it lies outside the chosen interval. For the $Q > m_Z$ data we removed five bins with downward fluctuations that were incompatible at the >10-sigma level with the cross section implied by neighboring data points and other experimental data in the same region. The list of these bins is L3 (136.1 GeV): [0.25, 0.275]; DELPHI (161 GeV): [0.32, 0.40]; DELPHI (183 GeV): [0.08, 0.09]; DELPHI (196 GeV): [0.16, 0.18]; and ALEPH (200 GeV): [0.16, 0.20].[12] Our default global data set contains a total of 487 bins. In the numerical analysis performed in Sec. VII we also examine alternative global data sets with different τ ranges.

The data sets were corrected by the experiments to eliminate the QED effects from initial-state radiation using bin-by-bin correction factors determined from Monte Carlo simulations. The primary aim of these corrections was to eliminate the effective reduction of the c.m. energy available for the production of the hadronic final state. In addition, in the data sets from the TASSO, L3, and ALEPH Collaborations the effects from final-state radiation of photons were eliminated, while they have been fully included in the data sets from the AMY, JADE, SLD, DELPHI, and OPAL Collaborations. It should also be noted that the approaches used by the experiments to treat photon radiation were dependent on the c.m. energy Q. For the $Q = m_Z$ data any radiation of initial-state photons is naturally suppressed as the effective c.m. energy for the hadronic final state gets shifted away from the Z pole. Therefore no specific photon cuts were applied for the $Q = m_Z$ data prior to the application of the bin-by-bin correction factors. For the data taken off the Z pole for either $Q < m_Z$ or $Q > m_Z$ the effects of initial-state radiation are substantial and explicit hard photon cuts were applied in the data taking prior to the application of the bin-by-bin correction procedure. We therefore consider the $Q = m_Z$ data sets as more reliable concerning the treatment of QED effects.

Since the size of the QED effects we find in the measurements of α_s and the soft function moment Ω_1 is comparable to the experimental uncertainties (see the results and discussions in Sec. VII), a less Monte Carlo dependent treatment of QED radiation would be certainly warranted. (See Ref. [44] for a recent discussion of QED radiation based on full one-loop matrix elements.) However, given that the impact of QED corrections we find for α_s and Ω_1 is still smaller than the current theoretical uncertainties from QCD, we use for our default numerical analysis the theory code with QED effects switched on, as described in Sec. II H. In Sec. VII we also present results when QED corrections are neglected for all data sets and for the case when they are neglected only for the TASSO, L3, and ALEPH data sets.

For the fitting procedure we use a χ^2 analysis, where we combine the statistical and the systematic experimental errors into the correlation matrix. We treat the statistical errors of all bins as independent. The systematic errors of the bins are correlated, but—unfortunately—practically no information on the correlation is given in the experimental publications. We therefore have to rely on a correlation model. For our analysis we assume as the default that within one thrust data set, i.e. for the set of thrust bins obtained by one experiment at one Q value, the systematic experimental errors are correlated in the minimal overlap model used by the LEP QCD working group [91,94]. In the minimal overlap model the off-diagonal entries of the experimental covariance matrix for the bins i and j within one data set are equal to $[\min(\Delta_i^{\rm sys}, \Delta_j^{\rm sys})]^2$, where $\Delta_{i,j}^{\rm sys}$ are the systematic errors of the bins i and j. This model implies a positive correlation of systematic uncertainties within each thrust data set. As a cross-check that our default correlation model does not introduce a strong bias we also carry out fits where the experimental systematic errors are assumed to be uncorrelated. Details are given in Sec. VII.

[12]Four out of these bins lie in our $\tau \in [6/Q, 0.33]$ default fit range. If they are included in the default data set, then for our final fit in Eq. (68) the $\chi^2 = 439$ increases by +81 and the central fit values show a slight decrease to $\alpha_s(m_Z) = 0.1132$ and a slight increase to $\Omega_1 = 0.336$ GeV.

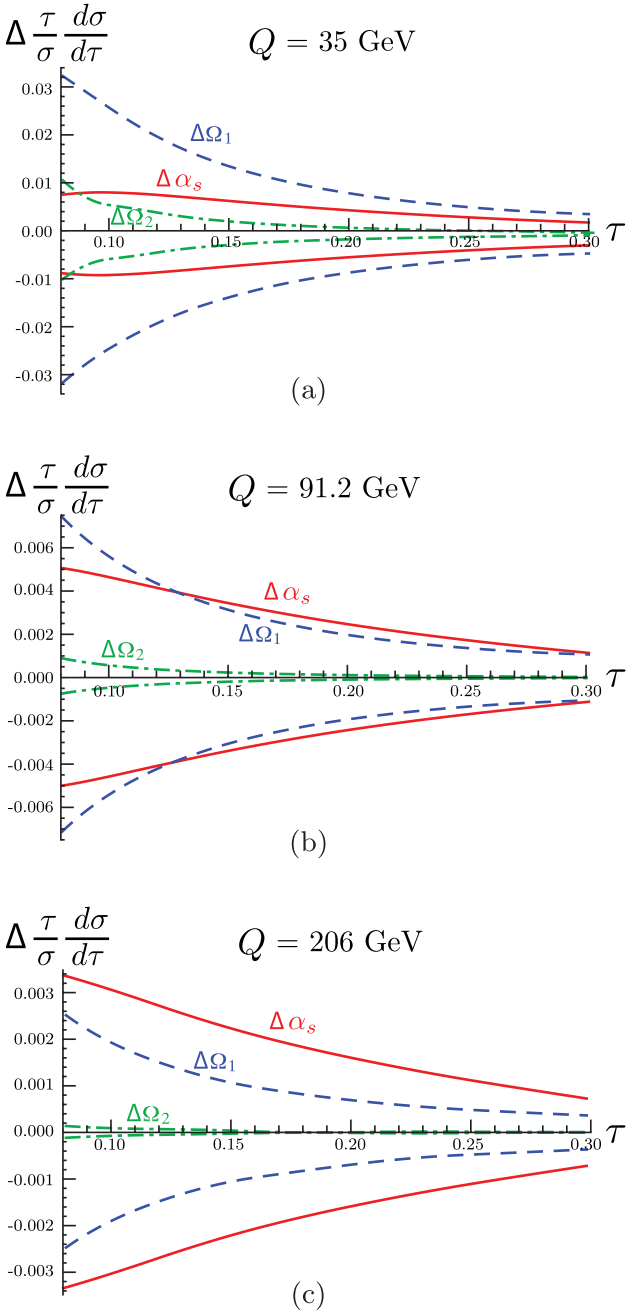

FIG. 10 (color online). Difference between default cross section and the cross section varying only one parameter as a function of τ. We vary $\alpha_s(m_Z)$ by ± 0.001 (solid red curves), $2\Omega_1$ by ± 0.1 GeV (dashed blue curves), and c_2 by ± 0.5 (dash-dotted green curves). The plot is shown for three different values of the center-of-mass energy: (a) $Q = 35$ GeV, (b) $Q = 91.2$ GeV, and (c) $Q = 206$ GeV.

To estimate the theoretical errors in the α_s-Ω_1 plane at any order and for any approximation used for the factorization formula (4), we carry out independent fits for 500 different sets of theory parameters which are randomly chosen in the ranges discussed in the previous sections and summarized in Table III. We take the area covered by the points of the best fits in the α_s-Ω_1 plane as the theory uncertainty treated like 1-sigma.[13] We emphasize that this method to estimate theoretical errors is more conservative than the error band method [26] employed, for example, in Refs. [20,22]. However, our method required considerably more computer power and it was necessary to use the Tier-2 centers at Garching and the Massachusetts Institute of Technology, as well as clusters at the Max Planck Institut and the University of Arizona. In Sec. VII we also present the outcome of other ways to estimate the theoretical error.

It is an important element of our analysis that we carry out global fits to the data from all values of $Q \geq 35$ (and all experiments). This is motivated by the strong degeneracy between α_s and Ω_1 in the tail region which can only be lifted when data from different Q values are simultaneously included in the fits.[14] In Fig. 10 the difference $d\sigma/d\tau - (d\sigma/d\tau)_{\text{default}}$ is displayed for $0.08 \leq \tau \leq 0.30$ and $Q = 35, 91.2$, and 206 GeV. Here $(d\sigma/d\tau)_{\text{default}}$ is the cross section for the default setting of the theory parameters with $\alpha_s(m_Z) = 0.114$ and $\Omega_1 = 0.35$ GeV, and for $d\sigma/d\tau$ we vary either $\alpha_s(m_Z)$ by ± 0.001 (solid red curves) or $2\Omega_1$ by ± 0.1 GeV (dashed blue curves) from their default values. The figures show that in the tail region changes in α_s can be compensated by changes in Ω_1. This degeneracy makes it impossible to determine α_s and Ω_1 simultaneously with small uncertainties from tail fits that use data from one Q value (or from a narrow range of Q values). On the other hand, we see that the correlation is Q-dependent when considering a large enough range of Q values. In our fits it is particularly important to include, apart from the data from $Q = m_Z$, the low-energy data from JADE, TASSO, and AMY and the high energy data from the LEP-II experiments. Although the errors in these analyses are larger than from the high-statistics $Q = m_Z$ run at LEP-I these data sets are essential for breaking the degeneracy and simultaneously extracting α_s and Ω_1.

VII. NUMERICAL ANALYSIS

Having explained all ingredients of the factorization formula (4) and the fit procedure we are now in the position to discuss the numerical results of our analysis based on a global fit to the experimental data for $Q \geq 35$ GeV in the tail region. In the tail region the dominant power corrections are encoded in the first moment Ω_1 [see Eq. (6)], so we can determine $\alpha_s(m_Z)$ and Ω_1 from a simultaneous fit. In this section we examine in detail the numerical results of

[13]This corresponds to a 1-sigma error (68% C.L.) in α_s as well as in Ω_1.

[14]The presence of this degeneracy is presumably also related to why Monte Carlo generators that are tuned to LEP data tend to have smaller hadronization corrections at $Q = m_Z$ than at larger Q values. See Sec. IX.

our fits concerning the treatment of the perturbative, hadronization, and experimental errors, QED and bottom mass corrections, and their dependence on the choice of the data set. We note that the values quoted for Ω_1 in the R-gap scheme are given for reference scales $R_\Delta = \mu_\Delta = 2$ GeV; see Sec. II F.

A. Theory scan

In Fig. 11 the best fit points of the theory parameters scan in the α_s-$2\Omega_1$ plane are displayed at NLL′ (brown), NNLL (magenta), NNLL′ (green), N^{3}LL (blue), and N^{3}LL′ (red) order. The fit results at N^{3}LL′ order include bottom mass and QED corrections. In Fig. 11(a) the results

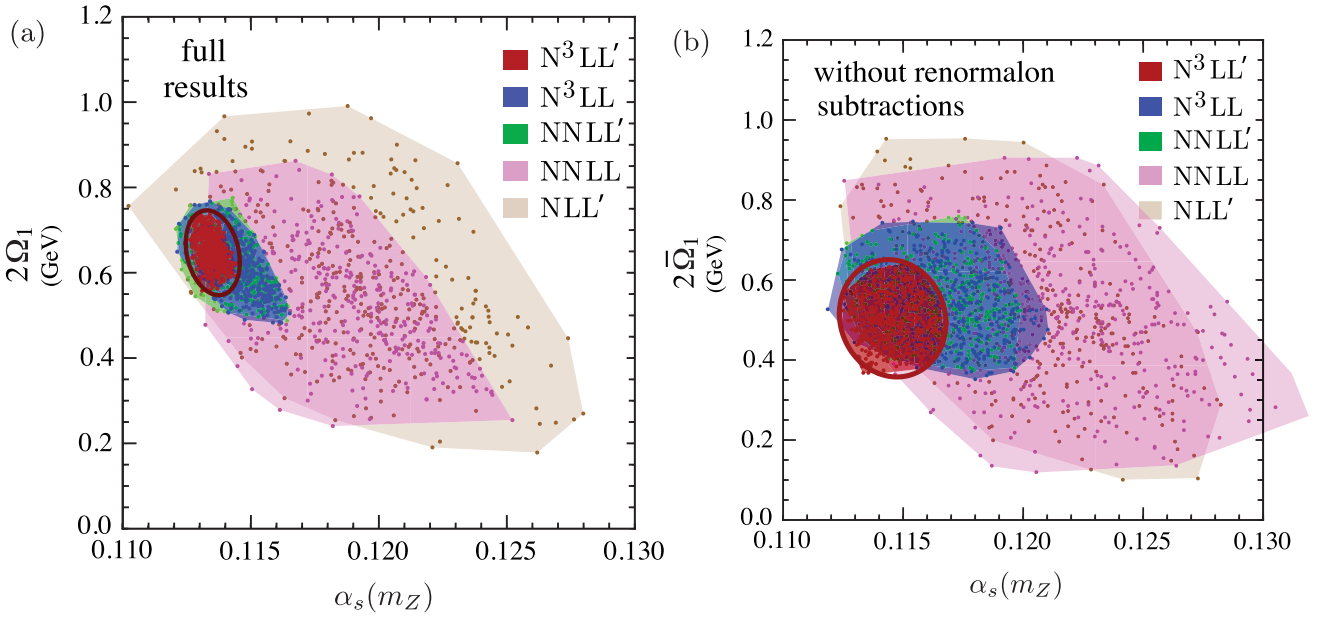

FIG. 11 (color online). Distribution of best fit points in the $\alpha_s(m_Z)$-$2\Omega_1$ and $\alpha_s(m_Z)$-$2\bar{\Omega}_1$ planes. Panel (a) shows results including perturbation theory, resummation of the logs, the soft nonperturbative function, and Ω_1 defined in the R-gap scheme with renormalon subtractions. Panel (b) shows the results as in panel (a) but with $\bar{\Omega}_1$ defined in the $\overline{\text{MS}}$ scheme without renormalon subtractions. In both panels the respective total (experimental + theoretical) 39% C.L. standard error ellipses are displayed (thick dark red lines), which correspond to 1 sigma (68% C.L.) for either one-dimensional projection.

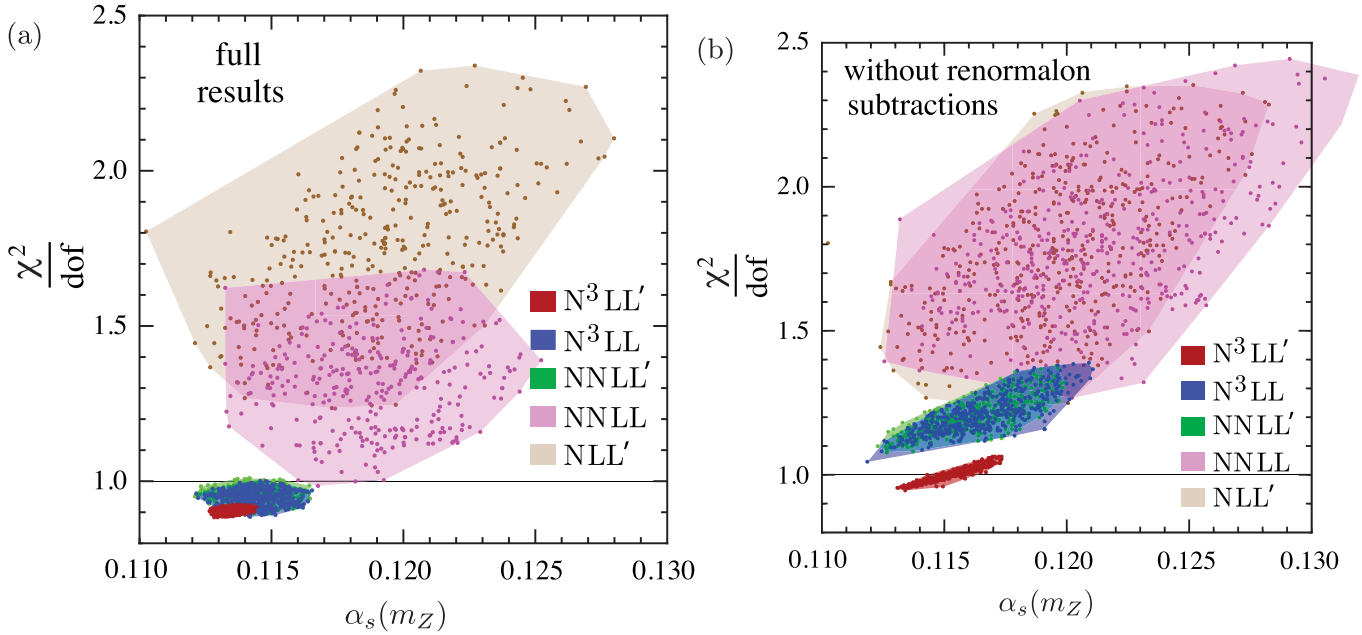

FIG. 12 (color online). Distribution of best fit points in the $\alpha_s(m_Z)$-χ^2/dof plane. Panel (a) shows the χ^2/dof values of the points given in Fig. 11(a). Panel (b) shows the χ^2/dof values of the points given in Fig. 11(b).

TABLE IV. Theory errors from the parameter scan and central values for $\alpha_s(m_Z)$ at various orders. The N^{3}LL$'$ value above the blank row is our final scan result, while the N^{3}LL$'$ values below the blank row show the effect of leaving out the QED corrections and leaving out both the b mass and QED, respectively. The central values are the average of the maximal and minimal values reached from the scan.

Order	$\alpha_s(m_Z)$ (with $\bar{\Omega}_1^{\overline{\rm MS}}$)	$\alpha_s(m_Z)$ (with $\Omega_1^{\rm Rgap}$)
NLL$'$	0.1203 ± 0.0079	0.1191 ± 0.0089
NNLL	0.1222 ± 0.0097	0.1192 ± 0.0060
NNLL$'$	0.1161 ± 0.0038	0.1143 ± 0.0022
N^{3}LL	0.1165 ± 0.0046	0.1143 ± 0.0022
N^{3}LL$'$ (full)	0.1146 ± 0.0021	**0.1135 ± 0.0009**
N^{3}LL$'_{(\rm QCD+m_b)}$	0.1153 ± 0.0022	0.1141 ± 0.0009
N^{3}LL$'_{(\rm pure\ QCD)}$	0.1152 ± 0.0021	0.1140 ± 0.0008

in the R-gap scheme with renormalon subtractions are shown, and in Fig. 11(b) the results in the $\overline{\rm MS}$ scheme without gap subtractions are given.

At each order 500 fits were carried out with the theory parameters randomly chosen in the ranges given in Table III. As described in Sec. VI, we take the size of the area in the α_s-$2\Omega_1$ plane covered by the best fit points as a measure for the theoretical uncertainties. To visualize the theoretical uncertainties we have colored the respective areas according to the orders. The fit results clearly show a substantial reduction of the theoretical uncertainties with increasing orders. Explicit numerical results for the respective central values (determined by the mean of the respective maximal and minimal values) and the theory errors (determined by half of the difference between maximal and minimal values) for α_s and Ω_1 are given in Tables IV and V, respectively. We will consider these theory errors as 1-sigma. At N^{3}LL$'$ order with Ω_1 in the R-gap scheme the theory error for $\alpha_s(m_Z)$ is ± 0.0009 compared to ± 0.0021 with $\bar{\Omega}_1$ in the $\overline{\rm MS}$ scheme. Also at NNLL$'$ and N^{3}LL we see that the removal of the $\mathcal{O}(\Lambda_{\rm QCD})$ renormalon leads to a reduction of the theoretical uncertainties by about a factor of 2 in comparison to the results with $\bar{\Omega}_1$ in the $\overline{\rm MS}$ scheme without renormalon subtraction. The proper treatment of the renormalon subtraction is thus a substantial part of a high-precision analysis for Ω_1 as well as for α_s.

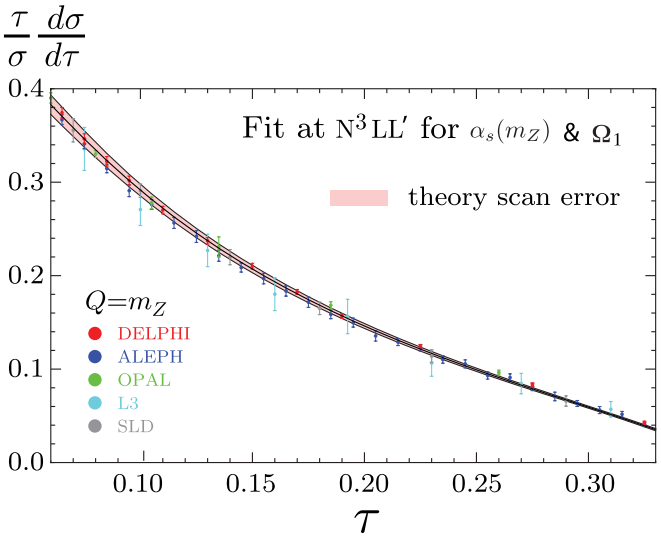

FIG. 13 (color online). Thrust distribution at N^{3}LL$'$ order and $Q = m_Z$ including QED and m_b corrections using the best fit values for $\alpha_s(m_Z)$ and Ω_1 in the R-gap scheme given in Eq. (68). The pink band represents the perturbative error determined from the scan method described in Sec. VI. Data from DELPHI, ALEPH, OPAL, L3, and SLD are also shown.

It is instructive to analyze the minimal χ^2 values for the best fit points shown in Fig. 11. In Fig. 12 the distributions of the best fits in the α_s-$\chi^2_{\rm min}$/dof plane are shown using the color scheme of Fig. 11. Figure 12(a) displays the results in the R-gap scheme, and Fig. 12(b) the ones in the $\overline{\rm MS}$ scheme. For both schemes we find that the $\chi^2_{\rm min}$ values and the size of the covered area in the α_s-$\chi^2_{\rm min}$/dof plane systematically decrease with increasing order. While the analysis in the $\overline{\rm MS}$ scheme for $\bar{\Omega}_1$ leads to $\chi^2_{\rm min}$/dof values around unity and thus an adequate description of the entire global data set at N^{3}LL$'$ order, we see that accounting for the renormalon subtraction in the R-gap scheme leads to a substantially improved theoretical description having $\chi^2_{\rm min}$/dof values below unity already at NNLL$'$ and N^{3}LL orders, with the N^{3}LL$'$ order result slightly lower at $\chi^2_{\rm min}$/dof $\simeq 0.91$. This demonstrates the excellent description of the experimental data contained in our global data set. It also validates the smaller theoretical uncertainties we obtain for α_s and Ω_1 at N^{3}LL$'$ order in the R-gap scheme.

As an illustration of the accuracy of the fit, in Fig. 13 we show the theory thrust distributions at $Q = m_Z$ for the full N^{3}LL$'$ order with the R-gap scheme for Ω_1, for the default theory parameters and the corresponding best fit values shown in bold in Tables IV and V. The pink band displays the theoretical uncertainty from the scan method. The fit

TABLE V. Theory errors from the parameter scan and central values for Ω_1 defined at the reference scales $R_\Delta = \mu_\Delta = 2$ GeV in units of GeV at various orders. The N^{3}LL$'$ value above the blank row is our final scan result, while the N^{3}LL$'$ values below the blank row show the effect of leaving out the QED corrections and leaving out both the b mass and QED, respectively. The central values are the average of the maximal and minimal values reached from the scan.

Order	$\bar{\Omega}_1$ ($\overline{\rm MS}$)	Ω_1 (R-gap)
NLL$'$	0.264 ± 0.213	0.293 ± 0.203
NNLL	0.256 ± 0.197	0.276 ± 0.155
NNLL$'$	0.283 ± 0.097	0.316 ± 0.072
N^{3}LL	0.274 ± 0.098	0.313 ± 0.071
N^{3}LL$'$ (full)	0.252 ± 0.069	**0.323 ± 0.045**
N^{3}LL$'_{(\rm QCD+m_b)}$	0.238 ± 0.070	0.310 ± 0.049
N^{3}LL$'_{(\rm pure\ QCD)}$	0.254 ± 0.070	0.332 ± 0.045

result is shown in comparison with data from DELPHI, ALEPH, OPAL, L3, and SLD and agrees very well. (Note that the theory values displayed are actually binned according to the ALEPH data set and then joined by a smooth interpolation.)

B. Band method

It is useful to compare our scan method to determine the perturbative errors with the error band method [26] that was employed in the analyses of Refs. [20,22,25]. In the error band method first each theory parameter is varied separately in the respective ranges specified in Table III while the rest are kept fixed at their default values. The resulting envelope of all these separate variations with the fit parameters $\alpha_s(m_Z)$ and Ω_1 held at their best fit values determines the error bands for the thrust distribution at the different Q values. Then, the perturbative error is determined by varying $\alpha_s(m_Z)$ keeping all theory parameters to their default values and the value of the moment Ω_1 to its best fit value. The resulting perturbative errors of $\alpha_s(m_Z)$ for our full N^{3}LL$'$ analysis in the R-gap scheme are given in the first line of Table VI. In the second line the corresponding errors for $\alpha_s(m_Z)$ in the $\overline{\rm MS}$ scheme for $\bar{\Omega}_1$ are displayed. The left column gives the error when the band method is applied such that the $\alpha_s(m_Z)$ variation leads to curves strictly inside the error bands for all Q values. For this method it turns out that the band for the highest Q value is the most restrictive and sets the size of the error. The resulting error for the N^{3}LL$'$ analysis in the R-gap scheme is more than a factor of 2 smaller than the error obtained from our theory scan method, which is shown in the right column. Since the high Q data have a much lower statistical weight than the data from $Q = m_Z$, we do not consider this method to be sufficiently conservative and conclude that it should not be used. The middle column gives the perturbative error when the band method is applied such that the $\alpha_s(m_Z)$ variation minimizes a χ^2 function which puts equal weight to all Q and thrust values. This second band method is more conservative, and for the N^{3}LL$'$ analyses in the R-gap and the $\overline{\rm MS}$ schemes the resulting errors are only 10% smaller than in the scan method that we have adopted. The advantage of the scan method we use is that the fit takes into account theory uncertainties including correlations.

C. Effects of QED and the bottom mass

Given the high precision we can achieve at N^{3}LL$'$ order in the R-gap scheme for Ω_1, it is a useful exercise to examine also the numerical impact of the corrections arising from the nonzero bottom quark mass and the QED corrections. In Fig. 14 the distributions of the best fit points in the α_s-$2\Omega_1$ plane at N^{3}LL$'$ in the R-gap scheme are displayed for pure massless QCD (light green points), including the bottom mass corrections (medium blue points) and the bottom mass as well as the QED corrections (dark red points). The distribution of the best fit points with bottom mass and QED corrections (dark red points) was already shown in Fig. 11(a). The large black dots represent the corresponding central values. The corresponding numerical results are shown at the bottom of Tables IV and V.

We see that the QED and bottom quark mass effects are somewhat smaller than the theoretical errors of the N^{3}LL$'$ analysis but not negligible. Moreover we find that the qualitative impact of the QED and the bottom quark mass effects is quite intuitive: The nonzero bottom quark mass primarily causes a horizontal shift of the thrust distribution towards larger τ values, since the small-τ threshold for massive quark production is moved to a finite τ value. Here this is compensated primarily by a reduced value of Ω_1. Concerning QED effects, they cause an effective increase of the coupling strength in the final-state interactions leading primarily to a decrease of α_s in the fit.

As explained in Sec. VI the experimental correction procedures applied to the AMY, JADE, SLD, DELPHI, and OPAL data sets were designed to eliminate initial-state photon radiation, while those of the TASSO, L3, and ALEPH Collaborations eliminated initial- and final-state radiation. It is straightforward to test for the effect of these differences in the fits by using our theory code with QED effects turned on or off depending on the data set. Since our

TABLE VI. Theoretical uncertainties for $\alpha_s(m_Z)$ obtained at N^{3}LL$'$ order from two versions of the error band method and from our theory scan method. The uncertainties in the R-gap scheme (first line) include renormalon subtractions, while the ones in the $\overline{\rm MS}$ scheme (second line) do not and are therefore larger. The same uncertainties are obtained in the analysis without the nonperturbative function (third line). Larger uncertainties are obtained from a pure $\mathcal{O}(\alpha_s^3)$ fixed-order analysis (lowest line). Our theory scan method is more conservative than the error band method.

	Band method 1	Band method 2	Our scan method
N^{3}LL$'$ with $\Omega_1^{R\,\rm gap}$	0.0004	0.0008	0.0009
N^{3}LL$'$ with $\bar{\Omega}_1^{\overline{\rm MS}}$	0.0016	0.0019	0.0021
N^{3}LL$'$ without $S_\tau^{\rm mod}$	0.0018	0.0021	0.0034
$\mathcal{O}(\alpha_s^3)$ fixed-order	0.0018	0.0026	0.0046

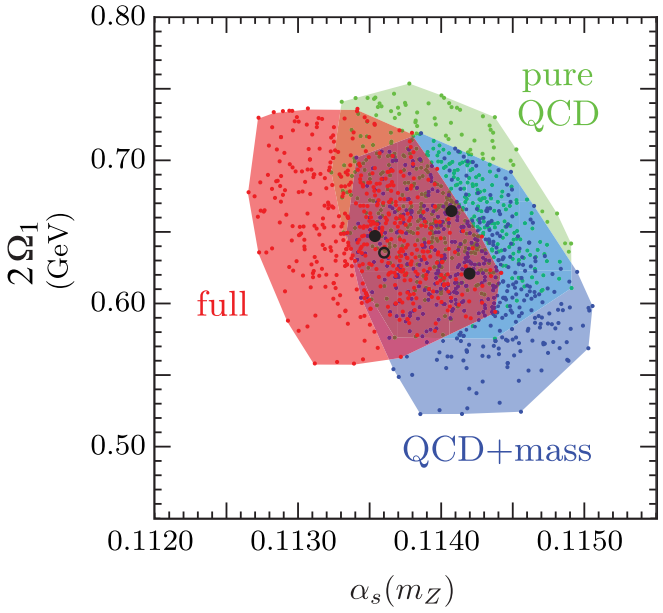

FIG. 14 (color online). Distribution of best fit points at N^{3}LL$'$ order with Ω_1 in the R-gap scheme in pure QCD (light green), including m_b effects (medium blue) and including m_b effects and QED corrections (dark red). Solid circles indicate the central points for these three cases. The hollow circle represents the central point from the global fit with QED corrections neglected for the data from TASSO, L3, and ALEPH but included for all other data sets.

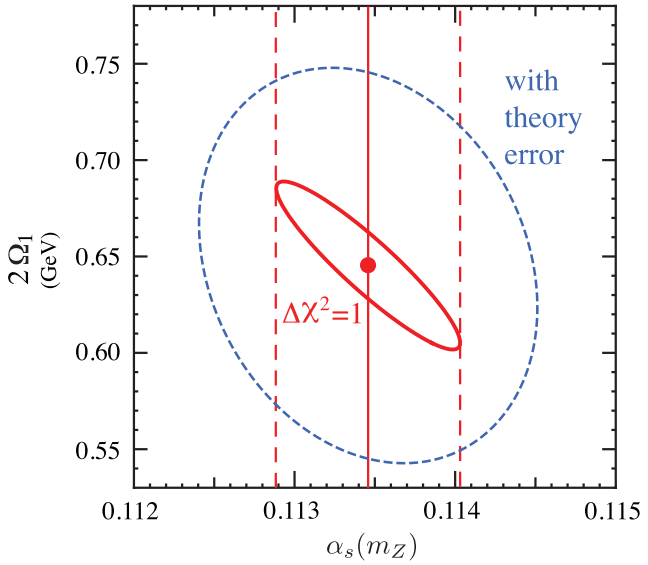

FIG. 15 (color online). Experimental 1-sigma standard error ellipse (red solid) in the α_s-$2\Omega_1$ plane. The larger ellipse shows the total uncertainty including theory errors (blue dashed). The fit is at N^{3}LL$'$ order in the R-gap scheme for Ω_1 using the central values of the correlation matrix given in Eq. (64). The center of the ellipse are the central values of our final result given in Eq. (68).

χ^2 procedure treats data from different experiments as uncorrelated it is also easy to implement this technically. Using our N^{3}LL$'$ order code in the R-gap scheme we obtain the central values $\alpha_s(m_Z) = 0.1136$ and $\Omega_1 = 0.318$ GeV, indicated by the hollow circle in Fig. 14. Comparing to our default results given in Tables IV and V, which are based on the theory code where QED effects are included for all data sets, we see that the central value for α_s is larger by 0.0001 and the one for Ω_1 is smaller by 0.006 GeV. This shift is substantially smaller than our perturbative error and justifies our choice to use the theory code with QED effects included as the default code for our analysis.

D. Hadronization and experimental error

An important element in the construction of the χ^2 function used for our fit procedure is the correlation model for the systematic uncertainties given for the experimental thrust bins. The results discussed above rely on the minimal overlap model for the systematic experimental errors explained in Sec. VI. The 1-sigma ellipse based on the central values of Eq. (64) and centered around $(\alpha_s, 2\Omega_1) = (0.1135, 0.647\ \text{GeV})$ is shown in Fig. 15 by the red solid ellipse. This ellipse yields the experimental errors and hadronization uncertainty related to Ω_1 in our analysis. We find that the size and correlation coefficients of the 1-sigma error ellipses at N^{3}LL$'$ order of all fits made in our theory scan are very similar, and hence we can treat the theory error and these hadronization and experimental errors as independent.

The correlation matrix of the red solid error ellipses is $(i, j = \alpha_s, 2\Omega_1)$

$$V_{ij} = \begin{pmatrix} \sigma^2_{\alpha_s} & \sigma_{\alpha_s}\sigma_{2\Omega_1}\rho_{\alpha\Omega} \\ \sigma_{\alpha_s}\sigma_{2\Omega_1}\rho_{\alpha\Omega} & \sigma^2_{2\Omega_1} \end{pmatrix} = \begin{pmatrix} 3.29(16)\times 10^{-7} & -2.30(12)\times 10^{-5}\ \text{GeV} \\ -2.30(12)\times 10^{-5}\ \text{GeV} & 1.90(18)\times 10^{-3}\ \text{GeV}^2 \end{pmatrix}, \tag{64}$$

where the correlation coefficient is significant and reads

$$\rho_{\alpha\Omega} = -0.9176(60). \tag{65}$$

The numbers in the parentheses represent the variance from the theory scan. From Eq. (64) it is straightforward to extract the experimental error for α_s and Ω_1 and the error due to variations of Ω_1 and α_s, respectively:

$$\begin{aligned} \sigma^{\text{exp}}_{\alpha_s} &= \sigma_{\alpha_s}\sqrt{1-\rho^2_{\alpha\Omega}} = 0.0002, \\ \sigma^{\text{exp}}_{\Omega_1} &= \sigma_{\Omega_1}\sqrt{1-\rho^2_{\alpha\Omega}} = 0.009\ \text{GeV}, \\ \sigma^{\Omega_1}_{\alpha_s} &= \sigma_{\alpha_s}|\rho_{\alpha\Omega}| = 0.0005, \\ \sigma^{\alpha_s}_{\Omega_1} &= \sigma_{\Omega_1}|\rho_{\alpha\Omega}| = 0.020\ \text{GeV}. \end{aligned} \tag{66}$$

For α_s, the error due to Ω_1 variations is the dominant part of the hadronization uncertainty. The blue dashed ellipse in Fig. 15 shows the total error in our final result quoted in Eq. (68) below.

The correlation exhibited by the red solid error ellipse in Fig. 15 is indicated by the line describing the semimajor axis

$$\frac{\Omega_1}{41.5\ \text{GeV}} = 0.1213 - \alpha_s(m_Z). \tag{67}$$

Note that extrapolating this correlation to the extreme case where we neglect the nonperturbative corrections ($\Omega_1 = 0$) gives $\alpha_s(m_Z) \to 0.1213$. This value is consistent with the fits in Refs. [22,25] shown in Table I, which are dominated by $Q = m_Z$ where the Monte Carlo hadronization uncertainties are smallest.

E. Individual theory scan errors

It is a useful exercise to have a closer look at the size of the theory uncertainties caused by the variation of each of the theory parameters we vary in our fit procedure in order to assess the dominant sources of theory errors. In Fig. 16 two bar charts are shown for the variation of the best fit values for $\alpha_s(m_Z)$ and $\Omega_1(R_\Delta, \mu_\Delta)$ at N^{3}LL$'$ order in the R-gap scheme with our default theory parameters. The bars show individual up-down variations of each of the theory parameters in the ranges given in Table III. The changes of the best fit values related to up variations of the theory parameters are given in dark blue, and those related to down variations are given in light green.

We see that the dominant theory uncertainties are related to variations of the profile functions (n_1, t_2, e_J, e_H) and the renormalization scale parameter (n_s) for the nonsingular partonic distribution $d\hat{\sigma}_{\text{ns}}/d\tau$. The uncertainties related to the numerical errors of the perturbative constants (s_2, s_3, and j_3) as well as the numerical errors in the extraction of

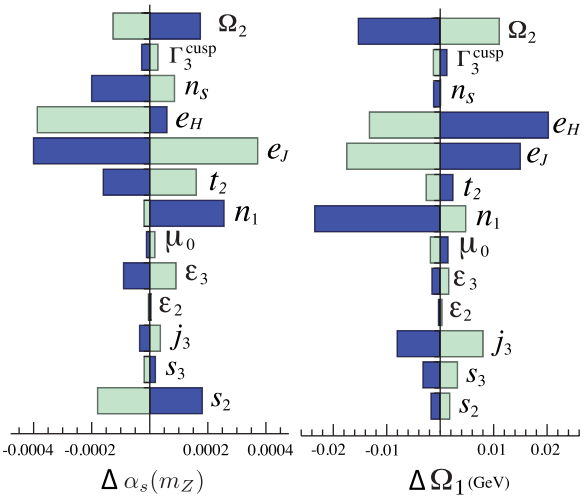

FIG. 16 (color online). Variations of the best fit values for $\alpha(m_Z)$ and Ω_1 from up (dark shaded blue) and down (light shaded green) variations for the theory parameters with respect to the default values and in the ranges given in Table III. For the variation of the moment Ω_2 we use $\Omega_2/\Omega_1^2 = 1.18^{+0.32}_{-0.18}$ as explained in the text.

the nonsingular distribution for small τ values (ϵ_2 and ϵ_3) are—with the exception of s_2—much smaller and do not play an important role. The theory error related to the unknown 4-loop contribution to the cusp anomalous dimension is negligible. Adding quadratically the symmetrized individual errors shown in Fig. 16 for each parameter, we find 0.0006 for α_s and 0.029 for Ω_1. This is about 2/3 of the theoretical uncertainty we have obtained by the theory parameter scan, and it demonstrates that the theory parameter scan represents a more conservative method to estimate the theory error.

In Fig. 16 we have also shown the variation of the best fit values for $\alpha_s(m_Z)$ and $\Omega_1(R_\Delta, \mu_\Delta)$ due to variations of the second soft function moment parameter Ω_2. Our default choice for the parametrization of the soft function S_τ^{mod} uses $c_0 = 1$ and $c_{n>0} = 0$ with $\bar{\Delta}(R_\Delta, \mu_\Delta) = 0.05$ GeV. In this case λ is the only variable parameter of the soft model function S_τ^{mod}, and Ω_2 is predetermined by Eq. (57) with $c_2 = 0$. As explained in Sec. IV we modify Ω_2 by setting c_2 to nonzero values. It is instructive to discuss the Ω_2 values one should consider. From the Cauchy-Schwarz inequality one can show that $\Omega_2/\Omega_1^2 \geq 1$, giving a strict lower bound on Ω_2. This bound can only be reached if S_τ^{mod} is a delta function. Moreover, if S_τ^{mod} is positive definite, vanishing at $k = 0$, has a width of order Λ_{QCD}, has its maximum at a k value of order Λ_{QCD}, and has an exponential falloff for large k, then one finds $\Omega_2/\Omega_1^2 < 1.5$. We therefore adopt the range $1 \leq \Omega_2/\Omega_1^2 \leq 1.5$ as a conservative Ω_2 variation to carry out an error estimate. For our default parametrization we have $\Omega_2/\Omega_1^2 = 1.18$ and changing c_2 between ± 0.5 gives a variation of Ω_2/Ω_1^2 between 1.05 and 1.35. We find that the best fit values for α_s and Ω_1 are smooth linear functions of Ω_2/Ω_1^2 which allows for a straightforward extrapolation to the conservative range between 1.0 and 1.5. The results for the variations of the best fit values for $\alpha_s(m_Z)$ and Ω_1 for $\Omega_2/\Omega_1^2 = 1.18^{+0.32}_{-0.18}$ read $(\delta\alpha_s(m_Z))_{\Omega_2} = {}^{+0.00017}_{-0.00013}$ and $(\delta\Omega_1)_{\Omega_2} = {}^{+0.011}_{-0.015}$ and are also shown in Fig. 16. The symmetrized version of these errors are included in our final results. For our final results for $\alpha_s(m_Z)$ we add the uncertainties from Ω_1 and the one from Ω_2 quadratically giving the total hadronization error. For $\Omega_1(R_\Delta, \mu_\Delta)$ we quote the error due to Ω_2 separately.

F. Final results

As our final result for $\alpha_s(m_Z)$ and $\Omega_1(R_\Delta, \mu_\Delta)$, obtained at N^{3}LL$'$ order in the R-gap scheme for Ω_1, including bottom quark mass and QED corrections we obtain

$$\begin{aligned}\alpha_s(m_Z) &= 0.1135 \pm (0.0002)_{\text{exp}} \pm (0.0005)_{\text{hadr}} \\ &\quad \pm (0.0009)_{\text{pert}}, \\ \Omega_1(R_\Delta, \mu_\Delta) &= 0.323 \pm (0.009)_{\text{exp}} \pm (0.013)_{\Omega_2} \\ &\quad \pm (0.020)_{\alpha_s(m_Z)} \pm (0.045)_{\text{pert}}\ \text{GeV},\end{aligned} \tag{68}$$

where $R_\Delta = \mu_\Delta = 2$ GeV and we quote individual 1-sigma errors for each parameter. Equation (68) is the main result of this work. In Figs. 15 (blue dashed line) and 11(a) (thick dark red line) we have displayed the corresponding combined total (experimental + theoretical) standard error ellipse. To obtain the combined ellipse we take the theory uncertainties given in Tables IV and V together with the Ω_2 uncertainties, adding them in quadrature. The central values in Eq. (68) are determined by the average of the respective maximal and minimal values of the theory scan and are very close to the central values obtained when running with our default theory parameters. The fit has $\chi^2/\text{dof} = 0.91$ with a variation of ± 0.03 for the displayed scan points. Having added the theory scan and Ω_2 uncertainties reduces the correlation coefficient in Eq. (65) to $\rho^{\text{total}}_{\alpha\Omega} = -0.212$. As a comparison we have also shown in Fig. 11(b) the combined total (experimental + theoretical) error ellipse at N^{3}LL$'$ in the $\overline{\text{MS}}$ scheme for $\bar{\Omega}_1$ where the $\mathcal{O}(\Lambda_{\text{QCD}})$ renormalon is not subtracted.

Since our treatment of the correlation of the systematic experimental errors is based on the minimal overlap model, it is instructive to also examine the results treating all the systematic experimental errors as uncorrelated. At N^{3}LL$'$ order in the R-gap scheme the results that are analogous to Eqs. (68) read $\alpha_s(m_Z) = 0.1141 \pm (0.0002)_{\text{exp}} \pm (0.0005)_{\text{hadr}} \pm (0.0010)_{\text{pert}}$ and $\Omega_1(R_\Delta, \mu_\Delta) = 0.303 \pm (0.006)_{\text{exp}} \pm (0.013)_{\Omega_2} \pm (0.022)_{\alpha_s} \pm (0.055)_{\text{pert}}$ GeV with a combined correlation coefficient of $\rho^{\text{total}}_{\alpha\Omega} = -0.180$. The results are compatible with the results of Eqs. (68) and indicate that the ignorance of the exact correlation of the systematic experimental errors does not crucially affect the outcome of the fit.

G. Data set choice

We now address the question to which extent the results of Eqs. (68) depend on the thrust ranges contained in the global data set used for the fits. Our default global data set accounts for all experimental thrust bins for $Q \geq 35$ in the intervals $[\tau_{\text{min}}, \tau_{\text{max}}] = [6/Q, 0.33]$. (See Sec. VI for more details.) This default global data set is the outcome of a compromise that (i) keeps the τ interval large to increase statistics, (ii) sets τ_{min} sufficiently large such that the impact of the soft function moments Ω_i with $i \geq 2$ is small, and (iii) takes τ_{max} sufficiently low to exclude the far-tail region where the missing order $\alpha_s \Lambda_{\text{QCD}}/Q$ corrections potentially become important.

In Fig. 17 the best fits and the respective experimental 39% and 68% C.L. error ellipses for the default values of the theory parameters given in Table III are shown for global data sets based on different τ intervals. The results for the various τ intervals are each given in different colors. The results for our default global data set is given in red, and the subscript "strict" for some intervals means that bins are included in the data set if more than half their

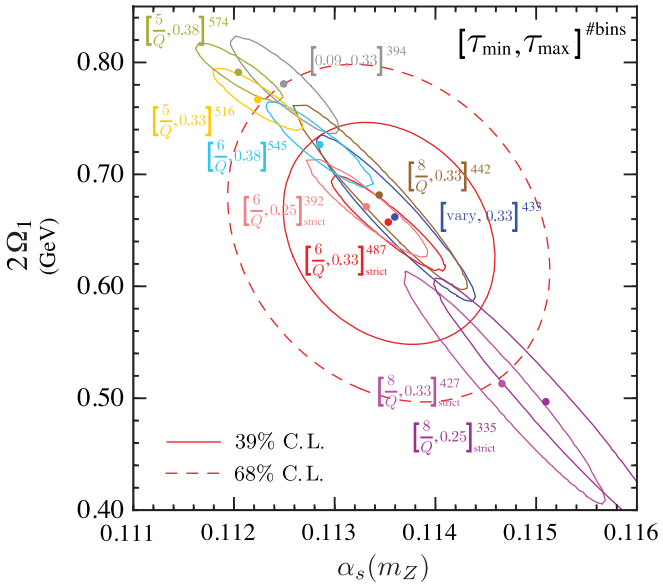

FIG. 17 (color online). The smaller elongated ellipses show the experimental 39% C.L. error (1 sigma for α_s) and best fit points for different global data sets at N^{3}LL$'$ order in the R-gap scheme and including bottom quark mass and QED effects. The default theory parameters given in Table III are employed. The larger ellipses show the combined theoretical plus experimental error for our default data set with 39% C.L. (solid line, 1 sigma for one dimension) and 68% C.L. (dashed line).

range is contained within the interval. For intervals without a subscript the criterion for selecting bins close to the boundaries of the τ interval is less strict and generically, if the τ_{min} and τ_{max} values fall in such bins, these bins are included. The numbers in superscript for each of the τ intervals given in the figure refer to the total number of bins contained in the global data set. We observe that the main effect on the outcome of the fit is related to the choice of τ_{min} and to the total number of bins. Interestingly all error ellipses have very similar correlation and are lined up approximately along the line

$$\frac{\Omega_1}{50.2\ \text{GeV}} = 0.1200 - \alpha_s(m_Z). \tag{69}$$

Lowering τ_{min} increases the dependence on Ω_2 and leads to smaller α_s and larger Ω_1 values. On the other hand, increasing τ_{min} leads to a smaller data set and to larger experimental error ellipses and hence to larger uncertainties.

It is an interesting but expected outcome of the fits that the pure experimental error for α_s (the uncertainty of α_s for fixed central Ω_1) depends fairly weakly on the τ range and the size of the global data sets shown in Fig. 17. If we had a perfect theory description, then we would expect that the centers and the sizes of the error ellipses would be statistically compatible. Here this is not the case, and one should interpret the spread of the ellipses shown in Fig. 17 as being related to the theoretical uncertainty contained in

our N^{3}LL$'$ order predictions. In Fig. 17 we have also displayed the combined (experimental and theoretical) 39% C.L. standard error ellipse from our default global data set which was already shown in Fig. 11(a) (and is 1-sigma, 68% C.L., for either one-dimensional projection). We also show the 68% C.L. error ellipse by a dashed red line, which corresponds to 1-sigma knowledge for both parameters. As we have shown above, the error in both the dashed and solid larger ellipses is dominated by the theory scan uncertainties; see Eqs. (68). The spread of the error ellipses from the different global data sets is compatible with the 1-sigma interpretation of our theoretical error estimate and hence is already represented in our final results.

H. Analysis without power corrections

Using the simple assumption that the thrust distribution in the tail region is proportional to α_s and that the main effect of power corrections is a shift of the distribution in τ, we have estimated in Sec. I that a 300 MeV power correction will lead to an extraction of α_s from $Q = m_Z$ data that is $\delta\alpha_s/\alpha_s \simeq (-9 \pm 3)\%$ lower than an analysis without power corrections. In our theory code we can easily eliminate all nonperturbative effects by setting $S_\tau^{\rm mod}(k) = \delta(k)$ and $\bar{\Delta} = \delta = 0$. At N^{3}LL$'$ order and using our scan method to determine the perturbative uncertainty a global fit to our default data set yields $\alpha_s(m_Z) = 0.1241 \pm (0.0034)_{\rm pert}$ which is indeed 9% larger than our main result in Eq. (68) which accounts for nonperturbative effects. It is also interesting to do the same fit with a purely fixed-order code, which we can do by setting $\mu_S = \mu_J = \mu_H$ to eliminate the summation of logarithms. The corresponding fit yields $\alpha_s(m_Z) = 0.1295 \pm (0.0046)_{\rm pert}$, where the displayed error has again been determined from the theory scan which in this case accounts for variations of μ_H and the numerical uncertainties associated with ϵ_2 and ϵ_3.

These results have been collected in Table VII together with the α_s results of our analyses with power corrections in the R-gap and the $\overline{\rm MS}$ schemes. For completeness we have also displayed the respective χ^2/dof values which were determined by the average of the maximal and the minimum values obtained in the scan. A detailed comparison of central fit values with Refs. [20,22] is given below in Sec. IX. Note that our fixed-order perturbative uncertainty of ± 0.0046 is 60% larger than the ± 0.0029 perturbative uncertainty quoted in Ref. [22] at this order. Also our uncertainty of ± 0.0034 at N^{3}LL$'$ without $S_\tau^{\rm mod}$ is significantly larger than the ± 0.0012 perturbative uncertainty of Ref. [20] at this order. This highlights the more conservative nature of our scan method for perturbative errors.

VIII. FAR-TAIL AND PEAK PREDICTIONS

The factorization formula (4) can be simultaneously used in the peak, tail, and far-tail regions. To conclude the discussion of the numerical results of our global analysis in the tail region, we use the results obtained from this tail fit to make predictions in the peak and the far-tail regions.

In Fig. 18 we compare predictions from our full N^{3}LL$'$ code in the R-gap scheme (solid red line) to the accurate ALEPH data at $Q = m_Z$ in the far-tail region. As input for $\alpha_s(m_Z)$ and Ω_1 we use our main result of Eq. (68) and all other theory parameters are set to their default values (see Table III). We find excellent agreement within the theoretical uncertainties (pink band). Key features of our theoretical result in Eq. (4) that are important in this far-tail region are (i) the nonperturbative correction from Ω_1, (ii) the merging of $\mu_S(\tau)$, $\mu_J(\tau)$, and μ_H toward $\mu_S = \mu_J = \mu_H$ at $\tau = 0.5$ in the profile functions, which properly treats the cancellations occurring at multijet thresholds, and (iii) integrating the theoretical distribution over experimental bins, rather than taking the difference of cumulants $\Sigma(\tau_2, \mu_i(\tau_2)) - \Sigma(\tau_1, \mu_i(\tau_1))$, as discussed in Sec. V. To illustrate the importance of Ω_1 we show the long-dashed red line in Fig. 18 which has the same value of $\alpha_s(m_Z)$ but turns off the nonperturbative corrections. To illustrate the importance of the treatment of multijet thresholds in our profile function, we take the Becher and Schwartz (BS) profile which does not account for the thresholds (the BS profile is defined and discussed below in Sec. IX) and use the smaller $\alpha_s(m_Z)$ and larger Ω_1 that are obtained from the global fit in this case. The result is shown by the solid light blue line in Fig. 18, which begins to deviate from the data for $\tau > 0.36$ and gives a cross section that does not fall to zero at $\tau = 0.5$. The fact that $\alpha_s(m_Z)$ is smaller by 0.0034 for the light blue line, relative to the solid red line, indicates that the proper theoretical description of the cross section in the far-tail region has an

TABLE VII. Comparison of global fit results for our full analysis to a fit where the renormalon is not canceled with $\bar{\Omega}_1$, a fit without $S_\tau^{\rm mod}$ [meaning without power corrections with $S_\tau^{\rm mod}(k) = \delta(k)$], and a fit at fixed order without power corrections and log resummation. All results include bottom mass and QED corrections.

	$\alpha_s(m_Z) \pm$ (pert. error)	χ^2/(dof)
N^{3}LL$'$ with $\Omega_1^{R\,\rm gap}$	0.1135 ± 0.0009	0.91
N^{3}LL$'$ with $\bar{\Omega}_1^{\overline{\rm MS}}$	0.1146 ± 0.0021	1.00
N^{3}LL$'$ without $S_\tau^{\rm mod}$	0.1241 ± 0.0034	1.26
$\mathcal{O}(\alpha_s^3)$ fixed-order without $S_\tau^{\rm mod}$	0.1295 ± 0.0046	1.12

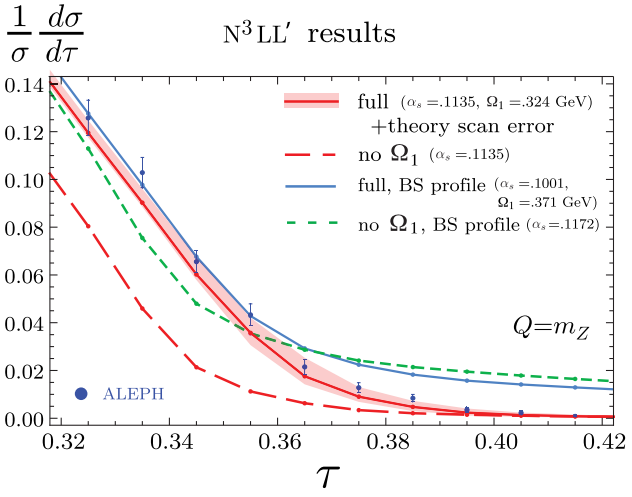

FIG. 18 (color online). Thrust distributions in the far-tail region at N^{3}LL′ order with QED and m_b corrections included at $Q = m_Z$ together with data from ALEPH. The red solid line is the cross section in the R-gap scheme using $\alpha_s(m_Z)$ and Ω_1 obtained from fits using our full code; see Eq. (68). The light red band is the perturbative uncertainty obtained from the theory scan method. The red dashed line shows the distribution with the same α_s but without power corrections. The light solid blue line shows the result of a full N^{3}LL′ fit with the BS profile that does not properly treat the multijet thresholds. The short-dashed green line shows predictions at N^{3}LL′ with the BS profile, without power corrections, and with the value of $\alpha_s(m_Z)$ obtained from the fit in Ref. [20]. All theory results are binned in the same manner as the experimental data and then connected by lines.

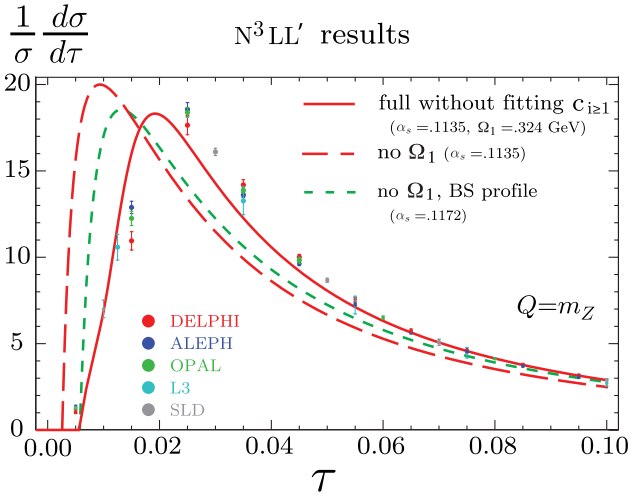

FIG. 19 (color online). Thrust cross section for the result of the N^{3}LL′ fit, with QED and m_b corrections included at $Q = m_Z$. The red solid line is the cross section in the R-gap scheme using $\alpha_s(m_Z)$ and Ω_1 obtained from fits using our full code; see Eq. (68). The red dashed line shows the distribution with the same α_s but without power corrections. The short-dashed green line shows predictions at N^{3}LL′ with the BS profile, without power corrections, and with the value of $\alpha_s(m_Z)$ obtained from the fit in Ref. [20]. Data from ALEPH, DELPHI, L3, SLD, and OPAL are also shown.

important impact on the fit done in the tail region. The final curve shown in Fig. 18 is the short-dashed green line, which is the result at the level of precision of the analysis by Becher and Schwartz in Ref. [20] (except that we integrate the theory distribution over the experimental bins rather than using a difference of cumulants). It uses the BS profile, has no power corrections, and has the value of α_s obtained from the fit in Ref. [20]. It also misses the $Q = m_Z$ data in this region. The results of other $\mathcal{O}(\alpha_s^3)$ thrust analyses, such as Davison and Webber [23] and Dissertori *et al.* [22,25], significantly undershoot the data in this far-tail region.[15] To the best of our knowledge, the theoretical cross section presented here is the first to obtain predictions in this far-tail region that agree with the data. Note that our analysis does include some $\mathcal{O}(\alpha_s^k \Lambda_{\rm QCD}/Q)$ power corrections through the use of Eq. (24). It does not account for the full set of $\mathcal{O}(\alpha_s \Lambda_{\rm QCD}/Q)$ power corrections as indicated in Eq. (4) [see also Table II(b)], but the agreement with the experimental data seems to indicate that missing power corrections may be smaller than expected.

Unbinned predictions for the thrust cross section at $Q = m_Z$ in the peak region are shown in Fig. 19. The green dashed curve shows the result at the level of precision in Becher and Schwartz, that is, N^{3}LL′, with the BS profile, without power corrections, and with the value of $\alpha_s(m_Z) = 0.1172$ obtained from their fit. This purely perturbative result peaks to the left of the data. With the smaller value of $\alpha_s(m_Z)$ obtained from our fit, the result with no power corrections peaks even slightly further to the left, as shown by the long-dashed red curve. In contrast, the red solid curve shows the prediction from our full N^{3}LL′ code in the R-gap scheme with our central fit values of $\alpha_s(m_Z)$ and Ω_1 given in Eq. (68). It clearly indicates that the value of Ω_1 obtained from the fit in the tail region shifts the theory prediction in the peak region much closer to the experimental data. The residual difference between the solid red theory curve and the experimental data can be attributed to the fact that the peak is sensitive to power corrections from higher moments, $\Omega_{k\geq 2}$, which have not been fit in our analysis. In our theoretical cross-section result this would correspond to fitting $\bar{\Delta}(R_\Delta, \mu_\Delta)$ and a subset of the higher coefficients $c_{i\geq 1}$. The $c_{i\geq 1}$ were all set to zero in the curves shown here. Perturbative uncertainties also must be accounted for in analyzing the peak region. We leave the presentation of results of this extended fit to a future publication.

IX. CROSS-CHECKS AND COMPARISONS

The result for $\alpha_s(m_Z)$ we obtain from our global N^{3}LL′ analysis in the R-gap scheme with 487 bins given in Eq. (68) is consistent at 1 sigma with the result of Davison and Webber [23] [$\alpha_s(m_Z) = 0.1164 \pm (0.0022)_{\rm hadr+exp} \pm (0.0017)_{\rm pert}$]. They also carried out a

[15]See the top panel of Fig. 9 in Ref. [23], the top left panel of Fig. 4 in Ref. [22], and the left panel of Fig. 2 in Ref. [25].

global thrust analysis with a total of 430 experimental bins. As explained in Sec. I, in their theory formula nonperturbative effects were included as a power correction in the effective coupling model which was fit from the experimental data, and their approach also accounts for a renormalon subtraction of the perturbative distribution. In these respects their analysis is similar to ours. However, it differs as their theory formula contains only resummation of logarithms at NLL order, and it also uses a different renormalon subtraction scheme which is based on the running coupling approximation for the subtraction corrections and does not account for the resummation of large logarithms. Moreover the separation of singular and nonsingular perturbative contributions and method to turn off the log resummation at large τ is not equivalent to the one we employ. The difference between their central value and perturbative error and our Eq. (68) can be attributed to these items. Their combined hadronization and experimental uncertainty utilizes an error rescaling using the value $\chi^2_{\rm min}/{\rm dof} = 1.09$ obtained for their best fit.

On the other hand, our main result for $\alpha_s(m_Z)$ given in Eq. (68) is smaller than the results of Dissertori *et al.* [22] by 2.9 sigma, of Dissertori *et al.* [25] by 2.2 sigma, and of Becher and Schwartz [20] by 1.6 sigma. (These results are displayed in Table I.) In these analyses $\alpha_s(m_Z)$ was determined from fits to data for individual Q values and, as explained in Sec. I, nonperturbative corrections and their associated uncertainty were taken from Monte Carlo generators in Dissertori *et al.* or left out from the fit and used to assign the hadronization uncertainty for the final result in Becher and Schwartz. It is possible to turn off pieces of our theoretical code to reproduce the perturbative precision of the codes used in Refs. [22][16] and [20]. It is the main purpose of the remainder of this section to show the outcome of the fits based on these modified theory codes. We show, in particular, that the main reason why the above results for $\alpha_s(m_Z)$ are higher than our result of Eq. (68) is related to the fact that the nonperturbative corrections extracted from Monte Carlo generators at $Q = m_Z$ are substantially smaller than and incompatible with the ones obtained from our fit of the field theory power correction parameter Ω_1. In Sec. I we already discussed why the use of Monte Carlo generators to estimate nonperturbative corrections in high-precision perturbative predictions is problematic.

We start with an examination related to the code used by Becher and Schwartz [20], which has N^{3}LL$'$ accuracy but does not include power corrections or renormalon subtractions. This treatment can be reproduced in our factorization formula by turning off the nonperturbative soft nonperturbative function by setting $S_\tau^{\rm mod}(k) = \delta(k)$ and $\bar\Delta = \delta = 0$. Moreover they used the central scale setting $\mu_H = Q$, $\mu_J = Q\sqrt{\tau}$, and $\mu_S = Q\tau$. We can reproduce this from our profile functions for $\mu_0 = n_1 = e_J = 0$, $t_2 = 3/2$, and $e_H = n_s = 1$, which we call the BS profile setting. The BS profile functions for $\mu_J(\tau)$ and $\mu_S(\tau)$ are shown by dashed curves in Fig. 8. (Note that the BS profile setting does not cause μ_S, μ_J, and μ_H to merge in the far-tail region and become equal at $\tau = 0.5$, which is needed to switch off the SCET resummation of logarithms in the multijet region to satisfy the constraints from multijet thresholds.) Becher and Schwartz set the $\mathcal{O}(\alpha_s^3)$ nonlogarithmic correction in the Euclidean hard factor $C(-q^2)$ to zero [with $H_Q = |C(q^2)|^2$ for $q^2 = Q^2 > 0$], which in our notation corresponds to $h_3 = 11\,771.50$ (somewhat larger than the now known h_3). We also set $s_2 = -40.1$ (see Refs. [20,62]) and $s_3 = -324.631$ for the nonlogarithmic $\mathcal{O}(\alpha_s^2)$ and $\mathcal{O}(\alpha_s^3)$ constants in the soft function (both within our range of uncertainties). The value for s_3 corresponds to setting the $\mathcal{O}(\alpha_s^3)$ nonlogarithmic corrections in the expanded position space soft function to zero. Finally, we also turn off our QED and bottom quark mass corrections and the $\mathcal{O}(\alpha_s^2)$ axial singlet corrections and use the fixed-order normalization from Eq. (59). For the fit procedure we follow Becher and Schwartz and analyze all ALEPH and OPAL data for individual Q values in the τ ranges given in their work and account only for statistical experimental errors in the χ^2 functions. The outcome of the fits for $\alpha_s(m_Z)$ at N^{3}LL$'$ order is given in the fourth column of Table VIII. The third column shows their central values and the respective statistical experimental errors as given in Ref. [20]. The numbers we obtain are 0.0001–0.0011 higher than their central values, and we attribute this discrepancy to the nonsingular contributions.[17] [Becher and Schwartz also used a difference of cumulants for their fits, as in Eq. (62) with the choice $\tilde\tau_1 = \tau_1$ and $\tilde\tau_2 = \tau_2$, rather than integrating $d\sigma/d\tau$ as we do for the table. The spurious contribution induced by this choice has a significant effect on the χ^2 values but a small effect on $\alpha_s(m_Z)$, changing the values shown in the table by ≤ 0.0003. For cumulants that use $\tilde\tau_1 = \tilde\tau_2 = (\tau_1 + \tau_2)/2$ with no spurious contribution, the difference from our integrated distribution results is reduced to ≤ 0.0001 for $\alpha_s(m_Z)$, and χ^2 values are almost unaffected.]

The numbers obtained at N^{3}LL$'$ above are significantly larger than our central fit result $\alpha_s(m_Z) = 0.1135$ shown in Eq. (68) obtained from our full code. These differences are mainly related to the nonperturbative power correction and partly due to the BS profile setting. To distinguish these two and other effects we can take the purely perturbative

[16]We do not attempt to reproduce the NLL/$\mathcal{O}(\alpha_s^3)$ code of Ref. [25] as the final outcome is similar to Ref. [22].

[17]Becher and Schwartz uncovered a numerical problem with the original EERAD3 code at very small τ, which correspondingly had an impact on the nonsingular function used in their analysis which was extracted from EERAD3. When their nonsingular distribution is updated to results from the new EERAD3 code they become significantly closer to ours, differing by $\lesssim 0.0002$. We thank M. Schwartz for correspondence about this and for providing us with their new fit values.

TABLE VIII. Comparison of the results for $\alpha_s(m_Z)$ quoted by Becher and Schwartz in Ref. [20] with results we obtain from our adapted code where power corrections, the m_b and QED corrections, and the $\mathcal{O}(\alpha_s^2)$ axial singlet corrections are neglected. The $\mathcal{O}(\alpha_s^3)$ nonlogarithmic constants h_3 and s_3 are set to the values used in Ref. [20] as described in the text. We follow the fit approach of Ref. [20] and employ their profile functions for the nonsingular, hard, jet, and soft scales, with results shown in the column labeled "our BS profile." In the last column we show results with this same code but using our default profile functions. The errors in parentheses in the third column are the statistical experimental uncertainty.

Experiment	Energy	BS result [20]	Our BS profile	Default profile
ALEPH	91.2 GeV	0.1168(1)	0.1170	0.1223
ALEPH	133 GeV	0.1183(37)	0.1187	0.1235
ALEPH	161 GeV	0.1263(70)	0.1270	0.1328
ALEPH	172 GeV	0.1059(80)	0.1060	0.1088
ALEPH	183 GeV	0.1160(43)	0.1166	0.1205
ALEPH	189 GeV	0.1203(22)	0.1214	0.1260
ALEPH	200 GeV	0.1175(23)	0.1182	0.1224
ALEPH	206 GeV	0.1140(23)	0.1149	0.1185
OPAL	91 GeV	0.1189(1)	0.1198	0.1251
OPAL	133 GeV	0.1165(38)	0.1175	0.1218
OPAL	177 GeV	0.1153(33)	0.1160	0.1200
OPAL	197 GeV	0.1189(14)	0.1197	0.1241
Average		**0.1172(10)**	**0.1180**	**0.1221**
Global fit (stat)	All Q		0.1188	0.1242
Global fit (stat + syst)	All Q		0.1192	0.1245

code described above and turn back to our default setting for the profile functions with the parameters given in Table III. The results are shown in the fifth column in Table VIII using again only statistical experimental errors in the χ^2 functions. The $\alpha_s(m_Z)$ values using our default profile functions are by 0.0028–0.0058 larger than for the BS profile setting in the fourth column.[18] (The fifth column results again integrate the distribution over each bin rather than using differences of cumulants, which for our profile is important for the reasons discussed in Sec. V.[19]) A similar difference arises from a global fit to our default data set of Sec. VI using the same fit procedure: For the BS profile setting we obtain $\alpha_s(m_Z) = 0.1189$, while the default profile setting gives $\alpha_s(m_Z) = 0.1242$ (second to last line of Table VIII). Using instead the χ^2 analysis of our main analysis which includes the experimental systematical errors we obtain $\alpha_s(m_Z) = 0.1192$ for the BS profile setting and $\alpha_s(m_Z) = 0.1245$ for the default profile setting (last line of Table VIII). The latter result is by 0.0110 larger than our 0.1135 central fit result in Eq. (68). This 10% effect is almost entirely coming from the power correction Ω_1. The difference of 0.3% to the full perturbative result of $\alpha_s(m_Z) = 0.1241$ given in Table VII illustrates the combined effect of the QED, the bottom quark mass, the $\mathcal{O}(\alpha_s^2)$ axial singlet corrections, and the $\mathcal{O}(\alpha_s^3)$ hard constant h_3.

Finally, let us examine the results related to the code used by Dissertori *et al.* in Ref. [22], which uses the fixed-order $\mathcal{O}(\alpha_s^3)$ results without a resummation of logarithms but accounts for nonperturbative corrections determined from the difference of running Monte Carlo generators in parton and hadron level modes. Since in this work we are not concerned with extracting the parton-hadron level transfer matrix from Monte Carlo generators, we use in the following our code neglecting power corrections by setting $S_\tau^{\rm mod}(k) = \delta(k)$, setting $\bar{\Delta} = \delta = 0$, and setting $\mu_H = \mu_J = \mu_S$. The latter switches off the log-resummation factors in Eq. (4) such that only the $\mathcal{O}(\alpha_s^3)$ fixed-order expression remains. We also include the m_b corrections but neglect QED effects. Since these modifications give us a code that does not contain nonperturbative corrections, the differences to Ref. [22] we obtain will serve as a quantitative illustration for the size of the hadronization corrections obtained by a transfer matrix from the Monte Carlo generators PYTHIA, HERWIG, and ARIADNE, tuned to global hadronic observables at m_Z.

For the fits for $\alpha_s(m_Z)$ we follow Dissertori *et al.* [22] analyzing ALEPH data for individual Q values in the τ ranges given in their work and accounting only for statistical experimental errors in the χ^2 functions. The results of Dissertori *et al.* and the outcome for our best fits are given

[18]With our full code, which accounts, in particular, for power corrections and renormalon subtractions, the shift due to the modified profile functions becomes smaller; shifts in $\alpha_s(m_Z)$ of 0.005 become 0.003.

[19]Using the cumulant method with $\tilde{\tau}_1 = \tau_1$ and $\tilde{\tau}_2 = \tau_2$ in Eq. (62), which has a spurious contribution, changes the values in the fifth column of Table III by about -0.003 to -0.005. On the other hand, using the cumulant method without a spurious contribution $\tilde{\tau}_1 = \tilde{\tau}_2 = (\tau_1 + \tau_2)/2$ changes the values in the fifth column by ≤ 0.0001.

TABLE IX. Comparison of the thrust results quoted in Ref. [22] with our numerical reproduction. For this numerical exercise we have used their procedure to get the error matrix for the experimental data. This amounts to considering only the statistical errors in an uncorrelated way, with the resulting experimental error shown in the third column. Whereas in the code of Ref. [22] hadronization corrections are included determined from Monte Carlo simulations, our numbers are based on a pure partonic code neglecting nonperturbative effects. We use the default value for the scale setting, i.e. $\mu = Q$.

Experiment	Energy	Dissertori *et al.* [22]	Our fixed-order code
ALEPH	91.2 GeV	0.1274(3)	0.1281
ALEPH	133 GeV	0.1197(35)	0.1289
ALEPH	161 GeV	0.1239(54)	0.1391
ALEPH	172 GeV	0.1101(72)	0.1117
ALEPH	183 GeV	0.1132(32)	0.1247
ALEPH	189 GeV	0.1140(20)	0.1295
ALEPH	200 GeV	0.1094(22)	0.1260
ALEPH	206 GeV	0.1075(21)	0.1214

in the third and fourth column of Table IX, respectively. We have also quoted the respective statistical errors from Ref. [22]. For the high-statistics data at $Q = m_Z$ our $\alpha_s(m_Z)$ result is larger than theirs, but the discrepancy amounts to only 0.0007, which is a 0.5% shift in $\alpha_s(m_Z)$. This illustrates the small size of the nonperturbative hadronization corrections encoded in the Monte Carlo transfer matrix at $Q = m_Z$. This is clearly incompatible with the size of the nonperturbative correction we have obtained from simultaneous fits of α_s and Ω_1, confirming the concerns on Monte Carlo hadronization corrections explained in Sec. I. Interestingly, with the exception of $Q = 172$ GeV, our fixed-order results for all Q are relatively stable and close to the result at $Q = m_Z$, while their $\alpha_s(m_Z)$ values, which use the transfer matrix for nonperturbative effects, are systematically lower for $Q > m_Z$ by 7%–13%. Thus the nonperturbative effects from the Monte Carlo transfer matrix are substantially larger for $Q > m_Z$.[20] The same behavior is also visible in the results of Ref. [25], which includes NLL resummation of logarithms. Since the transfer matrix is obtained from Monte Carlo generators tuned to the more accurate $Q = m_Z$ data, we believe that this issue deserves further investigation. To complete the discussion we use the same fixed-order theory code to quote results for a global fit to our default data set. Using the fit procedure as described in Sec. VI we obtain $\alpha_s(m_Z) = 0.1300 \pm (0.0047)_{\text{pert}}$. (The corresponding errors obtained from the error band method are given in the fourth line of Table VI.)

X. CONCLUSIONS

In this work we have provided a factorization formula for the thrust distribution in e^+e^- annihilation which incorporates the previously known $\mathcal{O}(\alpha_s^2)$ and $\mathcal{O}(\alpha_s^3)$ perturbative QCD corrections and summation of large logarithms at N^{3}LL order for the singular terms in the dijet limit where the thrust variable $\tau = 1 - T$ is small. The factorization formula used here incorporates a systematic description of nonperturbative effects with a soft function defined in field theory. The soft function describes the dynamics of soft particle radiation at large angles. We have also accounted for bottom mass and QED photon effects for fixed-order contributions as well as for the summation of QED logarithms. With specifically designed τ-dependent profile functions for the renormalization scales the factorization formula can be applied in the peak, tail, and far-tail regions of the thrust distribution. It has all nonperturbative effects accounted for up to terms of $\mathcal{O}(\alpha_s\Lambda_{\text{QCD}}/Q)$, which is parametrically smaller than the remaining perturbative uncertainty ($< 2\%$ for $Q = m_Z$) of the thrust distribution predictions in the tail region where we carried out the fits to the experimental data.

In the tail region, $2\Lambda_{\text{QCD}}/Q \ll \tau \lesssim 1/3$, the dominant effects of the nonperturbative soft function are encoded in its first moment Ω_1, which is a power correction to the cross section. Fitting to tail data at multiple Q's as we did in this work, the strong coupling $\alpha_s(m_Z)$ and the moment Ω_1 can be simultaneously determined. An essential ingredient to reduce the theoretical uncertainties to the level of $<2\%$ in the thrust distribution is our use of a short-distance scheme for Ω_1, called the R-gap scheme, that induces subtractions related to an $\mathcal{O}(\Lambda_{\text{QCD}})$ renormalon contained in the $\overline{\text{MS}}$ perturbative thrust cross section from large angle soft gluon radiation. The R-gap scheme introduces an additional scale that leads to large logarithms in the subtractions, and we carry out a summation of these additional logarithms with renormalization group equations in the variable R. The R-gap scheme reduces the perturbative uncertainties in our best highest order theory code by roughly a factor of 2 compared to the pure $\overline{\text{MS}}$ definition $\bar{\Omega}_1$, where renormalon effects are not treated.

[20]Note that the weighted average of the $Q > m_Z$ thrust results of Dissertori *et al.* is $\alpha_s(m_Z) = 0.1121$ and is consistent with our result in Eq. (68) within the larger uncertainties. Also note that the Q dependence of our $\Omega_1(R, R)/Q$ power correction is affected by its anomalous dimension; cf. Fig. 6.

The code we use in this analysis represents the most complete theoretical treatment of thrust existing at this time. As our final result we obtain

$$\alpha_s(m_Z) = 0.1135 \pm 0.0011,$$
$$\Omega_1(R_\Delta, \mu_\Delta) = 0.323 \pm 0.051 \text{ GeV}, \tag{70}$$

where α_s is defined in the $\overline{\text{MS}}$ scheme and Ω_1 in the R-gap scheme at the reference scales $R_\Delta = \mu_\Delta = 2$ GeV. Here the respective total 1-sigma errors are shown. The results with individual 1-sigma errors quoted separately for the different sources of uncertainties are given in Eq. (68). Neglecting the nonperturbative effects incorporated in the soft function, and in particular Ω_1, from the fits gives $\alpha_s(m_Z) = 0.1241$, which exceeds the result in Eq. (70) by 9%. This is consistent with a simple scaling argument one can derive from experimental data; see Eq. (3) in Sec. I.

Analyses of event shapes with a simultaneous fit of α_s and a power correction have been carried out earlier with the effective coupling model. Davison and Webber [23] analyzed the thrust distribution and determined $\alpha_s(m_Z) = 0.1164 \pm 0.0028$ also using $\mathcal{O}(\alpha_s^3)$ fixed-order input but implementing the summation of logarithms only at NLL order (for further discussion see Sec. IX). Recently Gehrmann, Jaquier, and Luisoni [95] analyzed moments of different event shape distributions, also with the effective coupling model, and obtained $\alpha_s(m_Z) = 0.1153 \pm 0.0029$ using fixed-order perturbation theory at $\mathcal{O}(\alpha_s^3)$. Both analyses neglected bottom mass and QED corrections. Our result in Eq. (70) is compatible with these analyses at 1 sigma but has smaller uncertainties.

These results and our result for $\alpha_s(m_Z)$ in Eq. (70) are substantially smaller than the results of event shape analyses employing input from Monte Carlo generators to determine nonperturbative effects. We emphasize that using parton-to-hadron level transfer matrices obtained from Monte Carlo generators to incorporate nonperturbative effects is not compatible with a high-order theoretical analysis such as ours, and thus analyses relying on such Monte Carlo input contain systematic errors in the determination of α_s from thrust data. The small effect of hadronization corrections on thrust observed in Monte Carlo generators at $Q = m_Z$ and the corresponding small shift in $\alpha_s(m_Z)$ do not agree with the 9% shift we have obtained from our fits as mentioned above. For the reasons discussed earlier, we believe Monte Carlo generators should not be used for hadronization uncertainties in higher order analyses.

Although our theoretical approach represents the most complete treatment of thrust at this time, and all sources of uncertainties known to us have been incorporated in our error budget, there are a number of theoretical issues related to subleading contributions that deserve further investigation. These issues include (i) the summation of logarithms for the nonsingular partonic cross section, (ii) the structure of the $\mathcal{O}(\alpha_s \Lambda_{\text{QCD}}/Q)$ power corrections, and (iii) analytic perturbative computations of the $\mathcal{O}(\alpha_s^2)$ and $\mathcal{O}(\alpha_s^3)$ nonlogarithmic coefficients s_2 and s_3 in the partonic soft function, the $\mathcal{O}(\alpha_s^3)$ nonlogarithmic coefficient j_3 in the partonic jet function, and the 4-loop QCD cusp anomalous dimension Γ_3^{cusp}. Concerning issue (i) we have incorporated in our analysis the nonsingular contributions in the fixed-order perturbation theory and estimated the uncertainty related to the higher order logarithms through the usual renormalization scale variation. Further theoretical work is needed to derive the renormalization group structure of subleading jet, soft, and hard functions in the nonsingular contributions and to use these results to sum the corresponding logarithms. Concerning issue (ii) we have shown that our theoretical description for the thrust distribution contains a remaining theoretical uncertainty from nonperturbative effects of order $\mathcal{O}(\alpha_s \Lambda_{\text{QCD}}/Q)$. Parametrically, this uncertainty is substantially smaller than the perturbative error of about 1.7% for the thrust distribution in the tail region at LEP-I energies

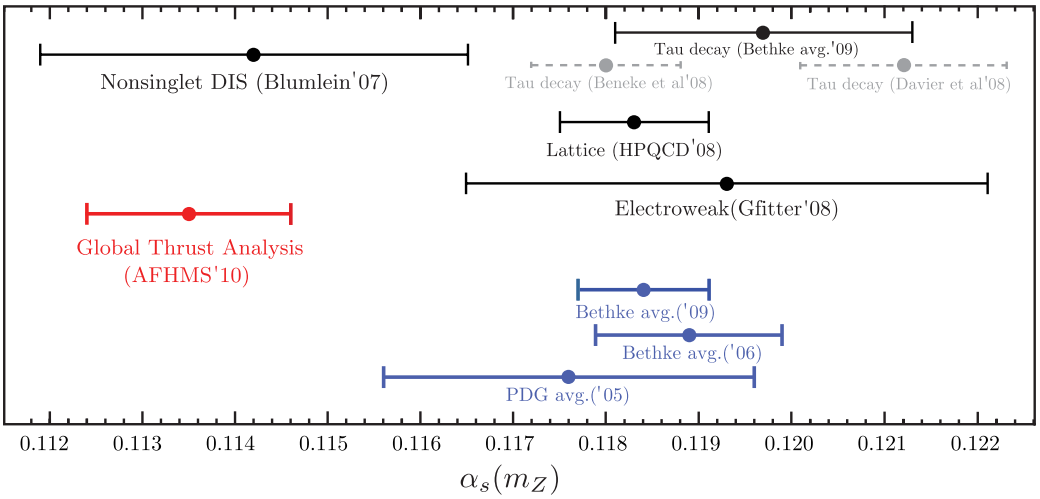

FIG. 20 (color online). Comparison of selected determinations of $\alpha_s(m_Z)$ defined in the $\overline{\text{MS}}$ scheme.

that is contained in our best theory code. Furthermore, our predictions in the far-tail region at $Q = m_Z$ appear to indicate that the dominant corrections of this order are already captured in our setup. Nevertheless a systematic analysis of these subleading effects is certainly warranted.

Apart from investigating these theoretical issues, it is also warranted to apply the high-precision approach using the soft-collinear effective theory to other event shape distributions in order to validate the result in Eq. (70). Event shapes that can be clearly treated with similar techniques are heavy jet mass, the C parameter, and angularities [96,97]. For many of these event shapes it has been proven field theoretically that the same parameter Ω_1 describes the leading power corrections in the tail region [65], although there might be caveats related to the experimental treatment of hadron masses [37,98]. Thus, one has the potential to extend the analysis done here to include additional data without additional parameters. An analysis for the heavy jet mass accounting for perturbative contributions at N^{3}LL in $\overline{\text{MS}}$ with different profile functions and a simple soft function model for power corrections without renormalon subtractions was recently carried out in Ref. [99], providing a first step in this direction. The final result for $\alpha_s(m_Z)$ obtained in Ref. [99] from the heavy jet mass spectrum is the result of a purely perturbative fit and, given the added uncertainty from neglecting power corrections, is fully consistent with our result.

To conclude this work we cannot resist comparing our result for $\alpha_s(m_Z)$ with the results of a selection of analyses using other techniques and observables, as shown in Fig. 20. We include a N^{3}LO analysis of data from deep inelastic scattering in the nonsinglet channel [100],[21] the recent HPQCD lattice determination based on fitting Wilson loops and the Υ-Υ' mass difference [105], the result from fits to electroweak precision observables based on the GFITTER package [106], and analyses of τ-decay data using the fixed-order [107] and contour-improved perturbation theory [108], together with an average of τ results from Ref. [109]. For a discussion on consistency with higher order terms in the τ-decay OPE see Ref. [110]. Finally we also show a collection of α_s averages from Refs. [109,111,112]. The deep inelastic scattering result is consistent with our fit result, whereas the deviation from HPQCD is 3.5σ. It is interesting to note that the high energy extractions from thrust and deep inelastic scattering appear to be smaller than the low-energy extractions from lattice and τ decays.

ACKNOWLEDGMENTS

This work was supported in part by the Director, Office of Science, Office of Nuclear Physics of the U.S. Department of Energy under Contracts No. DE-FG02-94ER40818 and No. DE-FG02-06ER41449 and the European Community's Marie-Curie Research Networks under Contracts No. MRTN-CT-2006-035482 (FLAVIAnet) and No. MRTN-CT-2006-035505 (HEPTOOLS). I. W. S. was also supported in part by the DOE OJI program, the Sloan Foundation, and the Alexander von Humboldt foundation. V. M. has been partially supported by a DFG "Eigenen Stelle" under Contract No. MA 4882/1-1. M. F. was supported in part by the German Academic Exchange Service (DAAD) D/07/44491. R. A., M. F. and I. W. S. thank the Max-Planck Institute for Physics for hospitality while parts of this work were completed. We thank Thomas Gehrmann for useful conversations on the experimental treatment of photon radiation and, in particular, for providing us with the most up-to-date numerical results from the program EERAD3 that made our N^{3}LL$'$ analysis possible. We are particularly indebted to Stefan Kluth for countless valuable discussions and information on experimental data and the usage of the program EVENT2. We are grateful to Daniel Wicke for useful discussions concerning the treatment of experimental data. We thank Thomas Hahn for computing support. M. F. thanks Sean Fleming for scientific advice. We thank T. Gehrmann, S. Kluth, M. Schwartz, and F. Tackmann for comments on the manuscript. We thank the Aspen Center for Physics for a stimulating environment when this work was finalized.

APPENDIX A: FORMULAS

In this appendix we collect all the remaining formulas used in our analysis for the case of massless quarks. The total hadronic cross section at tree level at the energies we are considering is

$$\sigma_0(Q) = \sum_{q\neq\text{top}} [\sigma^q_{ax}(Q) + \sigma^q_{\text{vec}}(Q)], \tag{A1}$$

where Q is the c.m. energy. For a quark of flavor q the tree level axial-vector and vector cross sections are

$$\begin{aligned}
\sigma_0^{qa} &= N_c \frac{4\pi\alpha^2}{3Q^2} \frac{Q^4(v_e^2 + a_e^2)a_q^2}{(m_Z^2 - Q^2)^2 + \frac{Q^4}{m_Z^2}\Gamma_Z^2}, \\
\sigma_0^{qv} &= N_c \frac{4\pi\alpha^2}{3Q^2}\Bigg[e_q^2 - \frac{2e_q v_q v_e Q^2(Q^2 - m_Z^2)}{(m_Z^2 - Q^2)^2 + \frac{Q^4}{m_Z^2}\Gamma_Z^2} \\
&\quad + \frac{Q^4(v_e^2 + a_e^2)v_q^2}{(m_Z^2 - Q^2)^2 + \frac{Q^4}{m_Z^2}\Gamma_Z^2}\Bigg],
\end{aligned} \tag{A2}$$

where e_q is the electric charge of the quark, and

$$v_q = \frac{T_3^q - 2e_q \sin^2\theta_W}{\sin(2\theta_W)}, \qquad a_q = \frac{T_3^q}{\sin(2\theta_W)}. \tag{A3}$$

Here T_3^q is the third component of the weak isospin, and θ_W is the weak mixing angle. For our numerics we use the following values:

[21] Analyses studying α_s with data that depends also on the gluon parton distribution function have been carried out in Refs. [101–104].

$$\sin^2\theta_W = 0.231\,19, \qquad m_Z = 91.187\ \text{GeV},$$
$$\Gamma_Z = 2.4952\ \text{GeV}, \qquad m_t = 172\ \text{GeV}, \tag{A4}$$
$$m_b = 4.2\ \text{GeV}, \qquad \alpha(m_Z) = 1/127.925.$$

1. Singular cross-section formula

To simplify the numerical evaluation of the singular part of the differential cross section given in Eq. (11) we take $\mu = \mu_J$ so that $U_J^\tau(s - s', \mu_J, \mu_J) = \delta(s - s')$ and express the result in the following form:

$$\int dk\, \frac{d\hat{\sigma}_s}{d\tau}\left(\tau - \frac{k}{Q}\right) S_\tau^{\text{mod}}(k - 2\bar{\Delta}(R, \mu_S))$$
$$= Q \sum_I \sigma_0^I H_Q^I(Q, \mu_H) U_H(Q, \mu_H, \mu_J)$$
$$\times \int dk\, P(Q, Q\tau - k, \mu_J)$$
$$\times e^{-2\delta(R,\mu_S)(d/dk)} S_\tau^{\text{mod}}(k - 2\bar{\Delta}(R, \mu_S)), \tag{A5}$$

where the perturbative corrections from the partonic soft function, jet function, and soft evolution factor are contained in $P(Q, k, \mu_J) = \int ds \int dk' J_\tau(s, \mu_J) \times U_S^\tau(k', \mu_J, \mu_S) S_\tau^{\text{part}}(k - k' - s/Q, \mu_S)$. The integrals in P can be carried out explicitly so that it is given by a simple set of functions. The soft nonperturbative function $S_\tau^{\text{mod}}(k - 2\bar{\Delta})$ is discussed in Sec. IV, and in Eq. (A5) we have integrated by parts so the derivative in the exponential with the $\delta(R, \mu_S)$ acts on this nonperturbative function. H_Q^I, J_τ, S_τ^{part}, and $\exp(-2\delta(R, \mu_S) d/dk)$ [cf. Eq. (37)] involve series in $\alpha_s(\mu_h)$, $\alpha_s(\mu_J)$, and $\alpha_s(\mu_S)$ with no large logs, and in our numerical analysis we expand the product of these series out, order by order in α_s. This expansion is crucial for $S_\tau^{\text{part}}(k, \mu_S)$ and $\exp(-2\delta(R, \mu_S) d/dk)$ since it is needed to allow the renormalon in the two series to cancel.

For simplicity where possible we give ingredients in a numerical form for SU(3) color with $n_f = 5$ active flavors. The vector hard function to $\mathcal{O}(\alpha_s^3)$ is [42,48–52]

$$H_Q^v(Q, \mu) = 1 + \alpha_s(\mu_h)(0.745\,808 - 1.273\,24 L_Q - 0.848\,826 L_Q^2) + \alpha_s^2(\mu_h)(2.275\,87 - 0.025\,103\,5 L_Q - 1.065\,92 L_Q^2$$
$$+ 0.735\,517 L_Q^3 + 0.360\,253 L_Q^4) + \alpha_s^3(\mu_h)(0.000\,503\,93 h_3 + 2.780\,92 L_Q - 2.856\,54 L_Q^2 - 0.147\,051 L_Q^3$$
$$+ 0.865\,045 L_Q^4 - 0.165\,638 L_Q^5 - 0.101\,931 L_Q^6), \tag{A6}$$

where $L_Q = \ln\frac{\mu_h}{Q}$ and from Eq. (12) we have $h_3 = 8998.080$. Our axial-vector hard function for b quarks has an extra two-loop singlet piece from the large top-bottom mass splitting, $H_Q^{ba} = H_Q^v + H_Q^{\text{singlet}}$. H_Q^{singlet} was given in Eq. (13) and involves the real function [56]

$$I_2(r_t) = 10\Phi(r_t)^2 + 6\gamma(r_t) + \frac{\pi^2}{3} - \frac{1}{r_t^2}\{\text{Cl}_2[2\Phi(r_t)]\Phi(r_t) + \text{Cl}_3[2\Phi(r_t)] - \Phi(r_t)^2 - \zeta(3)\}$$
$$- \frac{2}{r_t}\{2\Phi(r_t)\,\text{Cl}_2[4\Phi(r_t)] - 2\,\text{Cl}_3[2\Phi(r_t)] + \text{Cl}_3[4\Phi(r_t)] + [4\gamma(r_t) + 3]\Phi(r_t)^2 + \zeta(3)\}$$
$$+ \sqrt{\frac{1}{r_t} - 1}\left\{4(4h(r_t) + \gamma(r_t))\Phi(r_t) + 4\,\text{Cl}_2[4\Phi(r_t)] - 6\Phi(r_t) - 6\,\text{Cl}_2[2\Phi(r_t)] - \frac{\text{Cl}_2[2\Phi(r_t)] + 2\gamma(r_t)\Phi(r_t)}{r_t}\right\}, \tag{A7}$$

where $r_t = Q^2/(4m_t^2)$ and

$$\Phi(r_t) = \arcsin(\sqrt{r_t}), \qquad \gamma(r_t) = \ln(2) + \tfrac{1}{2}\ln(r_t),$$
$$\text{Cl}_2(x) = \text{Im}[\text{Li}_2(e^{ix})], \qquad \text{Cl}_3(x) = \text{Re}[\text{Li}_3(e^{ix})], \tag{A8}$$
$$h(r_t) = \ln(2) + \tfrac{1}{2}\ln(1 - r_t).$$

The resummation of large logs from μ_H to μ_J is given by $U_H(Q, \mu_H, \mu_J)$ in Eq. (A5) which is the solution of the RGE for the square of the SCET Wilson coefficient [9]

$$U_H(Q, \mu_H, \mu) = e^{2K(\Gamma_H, \gamma_H, \mu, \mu_H)} \left(\frac{\mu_H^2}{Q^2}\right)^{\omega(\Gamma_H, \mu, \mu_H)}, \tag{A9}$$

and the functions ω and K are given in Eqs. (A23) and (A24) below.

Finally using results for the convolution of plus functions from Ref. [38] we have the momentum space formula

$$P(Q, k, \mu_J) = \frac{1}{\xi} E_S^{(\tau)}(\xi, \mu_J, \mu_S) \sum_{\substack{n,m,k,l=-1 \\ m+n+1 \geq k \\ k+1 \geq l}}^{\infty} V_k^{mn} J_m\left[\alpha_s(\mu_J), \frac{\xi Q}{\mu_J^2}\right]$$
$$\times S_n\left[\alpha_s(\mu_S), \frac{\xi}{\mu_S}\right] V_l^k[-2\omega(\Gamma_S, \mu_J, \mu_S)]$$
$$\times \mathcal{L}_l^{-2\omega(\Gamma_S, \mu_J, \mu_S)}\left(\frac{k}{\xi}\right). \tag{A10}$$

This result is independent of the dummy variable ξ.[22] Here $E_S^{(\tau)}(\xi, \mu_J, \mu_S)$ encodes part of the running between the jet and the soft scale [113,114]:

[22] When convoluted with S_τ^{mod} we evaluate the right-hand side of Eq. (A10) for $\xi = Q\tau - 2\bar{\Delta}(R, \mu_S)$ which simplifies the final numerical integration.

$$E_S^{(\tau)}(\xi,\mu_J,\mu_S) = \exp[2K(\Gamma_S,\gamma_S,\mu_J,\mu_S)]\left(\frac{\xi}{\mu_S}\right)^{-2\omega(\Gamma_S,\mu_J,\mu_S)} \times \frac{\exp[2\gamma_E\omega(\Gamma_S,\mu_J,\mu_S)]}{\Gamma[1-2\omega(\Gamma_S,\mu_J,\mu_S)]}. \tag{A11}$$

The sum in Eq. (A10) contains coefficients of the momentum space soft and jet functions. Shifting the plus functions so that they have common arguments gives

$$J(p^-k,\mu_J) = \frac{1}{p^-\xi}\sum_{m=-1}^{\infty} J_m\left[\alpha_s(\mu_J),\frac{p^-\xi}{\mu_J^2}\right]\mathcal{L}_m\left(\frac{k}{\xi}\right),$$
$$S(k,\mu_S) = \frac{1}{\xi}\sum_{n=-1}^{\infty} S_n\left[\alpha_s(\mu_S),\frac{\xi}{\mu_S}\right]\mathcal{L}_n\left(\frac{k}{\xi}\right). \tag{A12}$$

Here the thrust soft function coefficients are

$$S_{-1}[\alpha_s,x] = S_{-1}(\alpha_s) + \sum_{n=0}^{\infty} S_n(\alpha_s)\frac{\ln^{n+1}x}{n+1},$$
$$S_n[\alpha_s,x] = \sum_{k=0}^{\infty}\frac{(n+k)!}{n!k!}S_{n+k}(\alpha_s)\ln^k x. \tag{A13}$$

The soft function is known to $\mathcal{O}(\alpha_s^3)$ except for the constant s_3 term [14,15,20,62]

$$\begin{aligned}
S_{-1}(\alpha_s) &= 1 + 0.349066\alpha_s + (1.26859 + 0.0126651 s_2)\alpha_s^2 \\
&\quad + (1.54284 + 0.00442097 s_2 + 0.00100786 s_3)\alpha_s^3, \\
S_0(\alpha_s) &= 2.07321\alpha_s^2 + (4.80020 - 0.0309077 s_2)\alpha_s^3, \\
S_1(\alpha_s) &= -1.69765\alpha_s - 6.26659\alpha_s^2 \\
&\quad - (16.4676 + 0.021501 s_2)\alpha_s^3, \\
S_2(\alpha_s) &= 1.03573\alpha_s^2 - 0.567799\alpha_s^3, \\
S_3(\alpha_s) &= 1.44101\alpha_s^2 + 9.29297\alpha_s^3, \\
S_4(\alpha_s) &= -1.46525\alpha_s^3, \\
S_5(\alpha_s) &= -0.611585\alpha_s^3.
\end{aligned} \tag{A14}$$

Note that s_2 and s_3 are the $\mathcal{O}(\alpha_s^{2,3})$ coefficients of the nonlogarithmic terms in the series expansion of the logarithm of the position space thrust soft function. The coefficients appearing in the shifted thrust jet function are

$$J_{-1}[\alpha_s,x] = J_{-1}(\alpha_s) + \sum_{n=0}^{\infty} J_n(\alpha_s)\frac{\ln^{n+1}x}{n+1},$$
$$J_n[\alpha_s,x] = \sum_{k=0}^{\infty}\frac{(n+k)!}{n!k!}J_{n+k}(\alpha_s)\ln^k x \tag{A15}$$

and are known up to $\mathcal{O}(\alpha_s^3)$ except for the constant j_3 term [20,58–61,115]

$$\begin{aligned}
J_{-1}(\alpha_s) &= 1 - 0.608949\alpha_s - 2.26795\alpha_s^2 \\
&\quad + (2.21087 + 0.00100786 j_3)\alpha_s^3, \\
J_0(\alpha_s) &= -0.63662\alpha_s + 3.00401\alpha_s^2 + 4.45566\alpha_s^3, \\
J_1(\alpha_s) &= 0.848826\alpha_s - 0.441765\alpha_s^2 - 11.905\alpha_s^3, \\
J_2(\alpha_s) &= -1.0695\alpha_s^2 + 5.36297\alpha_s^3, \\
J_3(\alpha_s) &= 0.360253\alpha_s^2 + 0.169497\alpha_s^3, \\
J_4(\alpha_s) &= -0.469837\alpha_s^3, \\
J_5(\alpha_s) &= 0.0764481\alpha_s^3.
\end{aligned} \tag{A16}$$

The $\mathcal{L}$ distributions are defined as $[n \geq 0]$

$$\mathcal{L}_n^a(x) = \left[\frac{\theta(x)\ln^n x}{x^{1-a}}\right]_+ = \frac{d^n}{da^n}\mathcal{L}^a(x), \tag{A17}$$

$\mathcal{L}_{-1}^a(x) = \mathcal{L}_{-1}(x) = \delta(x)$, and for $a > -1$

$$\mathcal{L}^a(x) = \left[\frac{\theta(x)}{x^{1-a}}\right]_+ = \lim_{\epsilon\to 0}\frac{d}{dx}\left[\theta(x-\epsilon)\frac{x^a-1}{a}\right]. \tag{A18}$$

In Eq. (A10) we use the coefficients [38]

$$V_k^n(a) = \begin{cases} a\frac{d^n}{db^n}\frac{V(a,b)}{a+b}\Big|_{b=0}, & k=-1, \\ a\binom{n}{k}\frac{d^{n-k}}{db^{n-k}}V(a,b)|_{b=0} + \delta_{kn}, & 0\leq k\leq n, \\ \frac{a}{n+1}, & k=n+1 \end{cases} \tag{A19}$$

and the coefficients

$$V_k^{mn} = \begin{cases} \frac{d^m}{da^m}\frac{d^n}{db^n}\frac{V(a,b)}{a+b}\Big|_{a=b=0}, & k=-1, \\ \sum_{p=0}^m\sum_{q=0}^n \delta_{p+q,k}\binom{m}{p}\binom{n}{q}\frac{d^{m-p}}{da^{m-p}}\frac{d^{n-q}}{db^{n-q}}V(a,b)|_{a=b=0}, & 0\leq k\leq m+n, \\ \frac{1}{m+1}+\frac{1}{n+1}, & k=m+n+1, \end{cases} \tag{A20}$$

where

$$V(a,b) = \frac{\Gamma(a)\Gamma(b)}{\Gamma(a+b)} - \frac{1}{a} - \frac{1}{b}. \tag{A21}$$

Special cases not covered by the general formulas in Eqs. (A19) and (A20) include

$$V_{-1}^{-1}(a) = 1, \qquad V_0^{-1}(a) = a, \qquad V_{k\geq 1}^{-1}(a) = 0, \qquad V_k^{-1,n} = V_k^{n,-1} = \delta_{nk}. \tag{A22}$$

2. Evolution factors and anomalous dimensions

The evolution factors appearing in Eqs. (A9)–(A11) are

$$\begin{aligned}\omega(\Gamma,\mu,\mu_0) &= 2\int_{\alpha_s(\mu_0)}^{\alpha_s(\mu)}\frac{d\alpha}{\beta(\alpha)}\Gamma(\alpha)\\ &= -\frac{\Gamma_0}{\beta_0}\left\{\ln r+\frac{\alpha_s(\mu_0)}{4\pi}\left(\frac{\Gamma_1}{\Gamma_0}-\frac{\beta_1}{\beta_0}\right)(r-1)+\frac{1}{2}\frac{\alpha_s^2(\mu_0)}{(4\pi)^2}\left(\frac{\beta_1^2}{\beta_0^2}-\frac{\beta_2}{\beta_0}+\frac{\Gamma_2}{\Gamma_0}-\frac{\Gamma_1\beta_1}{\Gamma_0\beta_0}\right)(r^2-1)\right.\\ &\quad\left.+\frac{1}{3}\frac{\alpha_s^3(\mu_0)}{(4\pi)^3}\left[\frac{\Gamma_3}{\Gamma_0}-\frac{\beta_3}{\beta_0}+\frac{\Gamma_1}{\Gamma_0}\left(\frac{\beta_1^2}{\beta_0^2}-\frac{\beta_2}{\beta_0}\right)-\frac{\beta_1}{\beta_0}\left(\frac{\beta_1^2}{\beta_0^2}-2\frac{\beta_2}{\beta_0}+\frac{\Gamma_2}{\Gamma_0}\right)\right](r^3-1)\right\},\end{aligned}\tag{A23}$$

and

$$\begin{aligned}&K(\Gamma,\gamma,\mu,\mu_0)-\omega\left(\frac{\gamma}{2},\mu,\mu_0\right)\\ &=2\int_{\alpha_s(\mu_0)}^{\alpha_s(\mu)}\frac{d\alpha}{\beta(\alpha)}\Gamma(\alpha)\int_{\alpha_s(\mu_0)}^{\alpha}\frac{d\alpha'}{\beta(\alpha')}\\ &=\frac{\Gamma_0}{2\beta_0^2}\left\{\frac{4\pi}{\alpha_s(\mu_0)}\left(\ln r+\frac{1}{r}-1\right)+\left(\frac{\Gamma_1}{\Gamma_0}-\frac{\beta_1}{\beta_0}\right)(r-1-\ln r)-\frac{\beta_1}{2\beta_0}\ln^2 r+\frac{\alpha_s(\mu_0)}{4\pi}\left[\left(\frac{\Gamma_1\beta_1}{\Gamma_0\beta_0}-\frac{\beta_1^2}{\beta_0^2}\right)(r-1-r\ln r)\right.\right.\\ &\quad\left.-B_2\ln r+\left(\frac{\Gamma_2}{\Gamma_0}-\frac{\Gamma_1\beta_1}{\Gamma_0\beta_0}+B_2\right)\frac{(r^2-1)}{2}+\left(\frac{\Gamma_2}{\Gamma_0}-\frac{\Gamma_1\beta_1}{\Gamma_0\beta_0}\right)(1-r)\right]+\frac{\alpha_s^2(\mu_0)}{(4\pi)^2}\left[\left[\left(\frac{\Gamma_1}{\Gamma_0}-\frac{\beta_1}{\beta_0}\right)B_2+\frac{B_3}{2}\right]\frac{(r^2-1)}{2}\right.\\ &\quad+\left(\frac{\Gamma_3}{\Gamma_0}-\frac{\Gamma_2\beta_1}{\Gamma_0\beta_0}+\frac{B_2\Gamma_1}{\Gamma_0}+B_3\right)\left(\frac{r^3-1}{3}-\frac{r^2-1}{2}\right)-\frac{\beta_1}{2\beta_0}\left(\frac{\Gamma_2}{\Gamma_0}-\frac{\Gamma_1\beta_1}{\Gamma_0\beta_0}+B_2\right)\left(r^2\ln r-\frac{r^2-1}{2}\right)\\ &\quad\left.\left.-\frac{B_3}{2}\ln r-B_2\left(\frac{\Gamma_1}{\Gamma_0}-\frac{\beta_1}{\beta_0}\right)(r-1)\right]\right\},\end{aligned}\tag{A24}$$

where $r=\alpha_s(\mu)/\alpha_s(\mu_0)$ depends on 4-loop running couplings, and the coefficients are $B_2=\beta_1^2/\beta_0^2-\beta_2/\beta_0$ and $B_3=-\beta_1^3/\beta_0^3+2\beta_1\beta_2/\beta_0^2-\beta_3/\beta_0$. These results are expressed in terms of series expansion coefficients of the QCD β function $\beta[\alpha_s]$, of $\Gamma[\alpha_s]$ which is given by a constant of proportionality times the QCD cusp anomalous dimension, and of a noncusp anomalous dimension $\gamma[\alpha_s]$:

$$\beta(\alpha_s)=-2\alpha_s\sum_{n=0}^{\infty}\beta_n\left(\frac{\alpha_s}{4\pi}\right)^{n+1},\quad \Gamma(\alpha_s)=\sum_{n=0}^{\infty}\Gamma_n\left(\frac{\alpha_s}{4\pi}\right)^{n+1},\quad \gamma(\alpha_s)=\sum_{n=0}^{\infty}\gamma_n\left(\frac{\alpha_s}{4\pi}\right)^{n+1}.\tag{A25}$$

The coefficients for $n_f=5$ are [61,116–120]

$$\begin{aligned}&\beta_0=23/3,\quad \beta_1=116/3,\quad \beta_2=180.907,\quad \beta_3=4826.16,\\ &\Gamma_0^{\rm cusp}=16/3,\quad \Gamma_1^{\rm cusp}=36.8436,\quad \Gamma_2^{\rm cusp}=239.208.\end{aligned}\tag{A26}$$

For the unknown four-loop cusp anomalous dimension we use the Padé approximation assigning 200% uncertainty:

$$\Gamma_3^{\rm cusp}=(1\pm 2)\frac{(\Gamma_2^{\rm cusp})^2}{\Gamma_1^{\rm cusp}}.\tag{A27}$$

The anomalous dimensions for the hard, jet, and soft functions are [21,51,61,114,121–123]

$$\begin{aligned}&\Gamma_n^H=-\Gamma_n^{\rm cusp},\quad \Gamma_n^J=2\Gamma_n^{\rm cusp},\quad \Gamma_n^S=-\Gamma_n^{\rm cusp},\\ &\gamma_0^H=-8,\quad \gamma_1^H=1.141\,94,\quad \gamma_2^H=-249.388,\\ &\gamma_0^J=8,\quad \gamma_1^J=-77.3527,\quad \gamma_2^J=-409.631,\\ &\gamma_n^S=-\gamma_n^H-\gamma_n^J.\end{aligned}\tag{A28}$$

To determine the strong coupling $\alpha_s(\mu)$ in terms of $\alpha_s(m_Z)$ at 4 loops with 5 light flavors we use

$$\begin{aligned}\frac{1}{\alpha_s(\mu)}&=\frac{X}{\alpha_s(m_Z)}+0.401\,347\,248\ln X\\ &\quad+\frac{\alpha_s(m_Z)}{X}[0.011\,652\,28(1-X)+0.161\,079\,61\ln X]\\ &\quad+\frac{\alpha_s^2(m_Z)}{X^2}[0.158\,611\,7(X^2-1)+0.059\,972\,2(X+\ln X-X^2)\\ &\quad+0.032\,324\,4\{(1-X)^2-\ln^2 X\}],\end{aligned}\tag{A29}$$

where $X=1+\alpha_s(m_Z)\ln(\mu/m_Z)\beta_0/(2\pi)$ and the displayed numbers are determined from the β_i in Eq. (A26). The form in Eq. (A29) agrees very well with the numerical solution of the beta function equation.

3. Nonsingular cross-section formula

At $\mathcal{O}(\alpha_s^2)$ there is an axial singlet contribution to the nonsingular terms through the three-parton cut of Fig. 2, which is given by the function $f_{\rm singlet}$ appearing in Eq. (27)

for $f_{\rm qcd}^{ba}$. The result for this function can be extracted from results in Ref. [70] and reads [$r_t = Q^2/(4m_t^2)$]

$$f_{\rm singlet}(\tau, r_t) = -\frac{64}{3}\theta\left(\frac{1}{3}-\tau\right)\left[\int_{1+\tau}^{2(1-\tau)} dy\, y\, g(y-1, r_t) + (1-3\tau)\frac{(1+\tau)}{2} g(\tau, r_t)\right],$$
$$g(\tau, r_t) = \frac{2r_t[\sqrt{\frac{1-r_t\tau}{r_t\tau}}\sin^{-1}(\sqrt{r_t\tau}) - \sqrt{\frac{1-r_t}{r_t}}\sin^{-1}(\sqrt{r_t})] + [\sin^{-1}(\sqrt{r_t\tau})]^2 - [\sin^{-1}(\sqrt{r_t})]^2 - r_t\log(\tau)}{4r_t(1-\tau)^2}. \quad \text{(A30)}$$

4. *R* evolution

Finally we display here the function $D^{(k)}$ [39] which appears in the solution in Eq. (41) of the R-RGE equation for $\bar{\Delta}(R, R)$:

$$D^{(k)}(\alpha_1, \alpha_2) = e^{i\pi\hat{b}_1}\sum_{j=0}^{k}(-1)^j S_j[\Gamma(-\hat{b}_1 - j, t_1) - \Gamma(-\hat{b}_1 - j, t_2)], \quad \text{(A31)}$$

which is real since the complex phase $e^{i\pi\hat{b}_1}$ cancels the imaginary part coming from the incomplete Gamma functions, defined as

$$\Gamma(c, t) = \int_t^\infty dx\, x^{c-1}e^{-x}. \quad \text{(A32)}$$

In Eq. (A31) k is the order of the matrix elements. (That is, $k = 0$ for NLL$'$ and NNLL, $k = 1$ for NNLL$'$ and N^{3}LL, and $k = 2$ for N^{3}LL$'$. For lower orders $D^{(k)} = 0$.) In Eq. (A31) we have defined

$$t_i = -\frac{2\pi}{\beta_0\alpha_i}, \quad \hat{b}_1 = \frac{\beta_1}{2\beta_0^2}, \quad S_0 = 0, \quad S_1 = \frac{\gamma_1^R}{(2\beta_0)^2},$$
$$S_2 = \frac{\gamma_2^R}{(2\beta_0)^3} - \frac{2\beta_0^2\beta_1 + \beta_1^2 - \beta_0\beta_2}{16\beta_0^6}\gamma_1^R, \quad \text{(A33)}$$

where the R-anomalous dimensions γ_i^R were given in Eq. (40).

5. Total hadronic cross section

The total hadronic QCD cross section can be evaluated in the fixed-order perturbation theory with $\mu \simeq Q$ and was given in Eq. (58) with the vector QCD results given in Eq. (59). The function appearing in the singlet contribution in Eq. (58) at $\mathcal{O}(\alpha_s^2)$ is [56]

$$I(r_t) = \frac{-\Phi(r_t)\,\mathrm{Cl}_2[2\Phi(r_t)] - \mathrm{Cl}_3[2\Phi(r_t)] + \zeta_3}{r_t^2} + \sqrt{\frac{1}{r_t}-1}\left(\frac{2[1-\gamma(r_t)]\Phi(r_t) - \mathrm{Cl}_2[2\Phi(r_t)]}{r_t} + 2\,\mathrm{Cl}_2[2\Phi(r_t)] + 2[2\gamma(r_t) - 3]\Phi(r_t)\right) + 6\gamma(r_t) + 2\Phi(r_t)^2 - \frac{4\Phi(r_t)^2+1}{r_t} - \frac{\pi^2}{3}, \quad \text{(A34)}$$

where the necessary functions appear in Eq. (A8). Note that we have dropped the four particle cut contribution $I_4 = \pi^2/3 - 15/4$ since we have not accounted for it in the $\mathcal{O}(\alpha_s^2)$ nonsingular distribution.

APPENDIX B: SOFT FUNCTION OPE MATCHING

To derive Eq. (21) we must demonstrate uniqueness of the power correction Ω_1 and derive its perturbative Wilson coefficient to all orders in α_s. We carry out these two parts of the proof in turn.

Since the operator appearing in the matrix element Ω_1 is nonlocal, the proof of uniqueness is more involved than for a typical OPE where we could just enumerate all local operators of the appropriate dimension. Here we are integrating out perturbative soft gluons in $S_\tau(k, \mu)$ while retaining nonperturbative soft gluons. The hierarchy between these soft gluons is in their invariant masses $k^2 \gg \Lambda_{\rm QCD}^2$. This process cannot introduce Wilson lines in new lightlike directions nor additional Wilson lines following paths in n and $\bar{n}$. Thus the Wilson lines will be the same as those in the full theory operator, Eq. (17). Additional Wilson lines could only be induced by integrating out collinear or hard gluons, which would yield power corrections suppressed by the hard or jet scales. The second point to demonstrate is that dimension one combinations of derivatives other than $i\hat{\partial}$ do not lead to new nonperturbative matrix elements at this order. The key is that for derivative operators inside our vacuum matrix element involving Wilson lines, boost invariance along the thrust axis relates all matrix elements to Ω_1 [65]. The proof relies on boost invariance along the thrust axis of derivative operators inside the vacuum matrix element. To see this one defines the transverse energy flow operator $\mathcal{E}_T(\eta)$ by its action on states [17,47]

$$\mathcal{E}_T(\eta)|X\rangle = \sum_{i\in X}|\vec{k}_i^{\perp}|\delta(\eta - \eta_i)|X\rangle. \quad \text{(B1)}$$

Any dimension one derivative operator we might wish to consider, such as $n\cdot\partial, \bar{n}\cdot\partial, \partial_t, \partial_z, \ldots$, or combinations thereof, is given by an integral $\int d\eta h(\eta)\mathcal{E}_T(\eta)$ for an appropriate rapidity function $h(\eta)$. For example, for the thrust derivative $i\hat{\partial}$ we have $h(\eta) = e^{-|\eta|}$. Boost invariance implies [65]

$$\bar{\Omega}_1 = \frac{1}{2N_c}\langle 0|\mathrm{tr}\bar{Y}_{\bar{n}}^T(0)Y_n(0)i\hat{\partial}Y_n^\dagger(0)\bar{Y}_{\bar{n}}^*(0)|0\rangle$$
$$= \int d\eta \frac{h(\eta)}{2N_c}\langle 0|\mathrm{tr}\bar{Y}_{\bar{n}}^T(0)Y_n(0)\mathcal{E}_T(\eta+\eta')Y_n^\dagger(0)\bar{Y}_{\bar{n}}^*(0)|0\rangle$$
$$= \frac{1}{N_c}\langle 0|\mathrm{tr}\bar{Y}_{\bar{n}}^T(0)Y_n(0)\mathcal{E}_T(\eta')Y_n^\dagger(0)\bar{Y}_{\bar{n}}^*(0)|0\rangle, \quad \text{(B2)}$$

for arbitrary η'. The same steps hold for any other derivative operator and function $h(\eta)$, and different choices only affect the constant calculable prefactor. This suffices to show the second point.

To derive an all-orders expression for the Wilson coefficient of Ω_1 we construct an analog of the OPE matching done for the soft function in $B \to X_s\gamma$ [59]. The proof is considerably simpler for $B \to X_s\gamma$ because the OPE in that case yields local heavy quark effective theory operators. Nevertheless the thrust soft function can be manipulated such that a similar strategy can be used. Using the thrust axis we define hemisphere a, where $p^+ < p^-$, and hemisphere b, where $p^- < p^+$. Consider the soft function written as a matrix element squared:

$$S_\tau(k,\mu) = \frac{1}{N_c}\sum_X \delta(k - k_s^{a+} - k_s^{b-})\,\mathrm{tr}\langle 0|\bar{Y}_{\bar{n}}^T(0)Y_n(0)|X\rangle \times \langle X|Y_n^\dagger(0)\bar{Y}_{\bar{n}}^*(0)|0\rangle, \quad \text{(B3)}$$

where the trace is over color, $k_s^{a+} = n\cdot p_X^a$ is the total plus momentum of the particles in state X in hemisphere a, and $k_s^{b-} = \bar{n}\cdot p_X^b$ is the minus momenta of particles in X in hemisphere b. To carry out the OPE we need to consider a state that has overlap with the operator in Eq. (20). Thus we could replace the vacuum by very soft nonperturbative gluons with momenta of $\mathcal{O}(\Lambda_{\mathrm{QCD}})$ and then consider matrix elements with perturbative gluons having momenta $\sim k \gg \Lambda_{\mathrm{QCD}}$. Since the OPE is independent of the particular states we choose, we will instead consider a simpler alternative in the following.

First we write the matrix element in Eq. (B3) as

$$\mathrm{tr}\langle 0|\bar{Y}_{\bar{n}}^T Y_n|X\rangle\langle X|Y_n^\dagger \bar{Y}_{\bar{n}}^*|0\rangle = \langle 0|\bar{\zeta}_{\bar{n}}\bar{Y}_{\bar{n}}^T Y_n\zeta_n|Xu_n\upsilon_{\bar{n}}\rangle\langle Xu_n\upsilon_{\bar{n}}|\bar{\zeta}_n Y_n^\dagger \bar{Y}_{\bar{n}}^*\zeta_{\bar{n}}|0\rangle, \quad \text{(B4)}$$

where ζ_n and $\zeta_{\bar{n}}$ are noninteracting collinear fields whose contractions with the sterile quark u_n and antiquark $\upsilon_{\bar{n}}$ are chosen with a normalization to reproduce the original matrix element (and a sum over their color correctly reproduces the trace). Here u_n should be thought of as a very energetic collinear quark in hemisphere a with large label momentum p_n^- and zero residual momentum. The large momentum is conserved by soft interactions from the Wilson lines due to the SCET multipole expansion. Here the plus momentum of u_n is included into k_s^{a+} but is zero and does not contribute to the δ function. The same is true for $\upsilon_{\bar{n}}$ which has zero minus momentum and large label $p_{\bar{n}}^+$ momentum and is always in hemisphere b. We introduced u_n and $\upsilon_{\bar{n}}$ so that we can use them to systematically add a very soft momentum to the end of the Wilson lines (at ∞). They provide a convenient state with which to carry out the OPE, because there is nonzero overlap taking only the 1 out of the Wilson lines, Y. In particular, they allow us to perform the OPE and pick out the $i\hat{\partial}$ present in $\bar{\Omega}_1$ at tree level, without the necessity to add explicit soft gluons with momenta $\ll k$.

To carry out the OPE we now give u_n a very small soft momentum ℓ^+ and $\upsilon_{\bar{n}}$ a very small soft momentum ℓ^- and denote them by u_n^ℓ and $\upsilon_{\bar{n}}^\ell$, respectively. These particles are kept on-shell by adjusting their large label $\perp$ momenta so that $\ell^+ = p_{n\perp}^2/p_n^-$ and $\ell^- = p_{\bar{n}\perp}^2/p_{\bar{n}}^+$. Because of the multipole expansion these $\perp$ momenta have no influence on diagrams with perturbative soft gluons having momenta $k \ll p_{n\perp} = -p_{\bar{n}\perp}$. The Wilson line propagators reduce to the same as before, such as

$$\frac{p_n^-}{k^+p_n^- + \ell^+p_n^- + p_{n\perp}^2} = \frac{1}{k^+}. \quad \text{(B5)}$$

This property is familiar in SCET where soft couplings to energetic collinear quarks in SCET remain eikonal for any values of the quark's large momenta by using the equations of motion, as long as the final particles are on-shell. Thus at any order in perturbation theory, with any number of soft gluons and soft quarks of momenta $\sim k$ in the matrix elements, the only change caused by $\ell^\pm$ is on the $\delta(k - k_s^{a+} - k_s^{b-})$ in Eq. (B3) which is shifted to $\delta(k - \ell - k_s^{a+} - k_s^{b-})$, where $\ell \equiv \ell^+ + \ell^-$. Expanding with $\ell \ll k$ the matrix element with this choice of state evaluates to

$$S_\tau^{\mathrm{part}}(k-\ell,\mu) = S_\tau^{\mathrm{part}}(k) - \frac{dS_\tau^{\mathrm{part}}(k)}{dk}\ell + \cdots. \quad \text{(B6)}$$

At lowest order in emission of very soft gluons $\sim\Lambda_{\mathrm{QCD}}$ the corresponding matrix element in the lower energy theory is

$$\frac{1}{N_c}\langle 0|\bar{\zeta}_{\bar{n}}\bar{Y}_{\bar{n}}^T Y_n\zeta_n i\hat{\partial}|u_n^\ell\upsilon_{\bar{n}}^\ell\rangle\langle u_n^\ell\upsilon_{\bar{n}}^\ell|\bar{\zeta}_n Y_n^\dagger\bar{Y}_{\bar{n}}^*\zeta_{\bar{n}}|0\rangle = \ell. \quad \text{(B7)}$$

Virtual radiative corrections do not correct this result since they are scaleless and vanish in pure dimensional regularization. Thus we can identify $\ell \to 2\bar{\Omega}_1$ in Eq. (B6), and this then yields the stated result for the OPE in Eq. (21).

APPENDIX C: OPERATOR EXPANSION FOR THE FIRST THRUST MOMENT

For moment integrals of the thrust distribution over $\tau \in [0, 1/2]$ there is not a hierarchy of scales that induces large logs, and one may formulate the theoretical result in terms of an expansion in α_s and Λ_{QCD}/Q. The zeroth moment of thrust is just the total cross section for $e^+e^- \to$ hadrons, and the power corrections are formulated in terms of the well known OPE [124]. For higher moments the fact that thrust constrains a nontrivial combination of final-state momenta makes carrying out an OPE more difficult. For

example, when we weigh the integral by a power of thrust it is not possible to collapse all propagators to a point, so the nonperturbative parameters are no longer constrained to be given by a basis of local operators. In the effective coupling model [35] the same nonperturbative parameter α_0 that appears for the thrust distribution also occurs in the first moment. However it is not clear to what level of accuracy this carries over to a field theoretical description of power corrections derived from QCD. In this appendix we show how one can carry out an OPE for the 1st moment of the thrust distribution and demonstrate that at leading order it only involves the same nonperturbative matrix element Ω_1 from Eq. (6).

To carry out an OPE for the thrust moment we can work order by order in the hard $\alpha_s(Q)$ expansion and analyze direct computations where we couple soft nonperturbative gluons to hard partons in Feynman diagrams. The appropriate nonlocal operator(s) appearing in the expansion will be identified by the structure of the amplitudes in this computation. In the following discussion the soft gluons will *not* be treated as final-state particles for which there is a phase space integral but rather as a means of probing the structure of the nonperturbative operator. The lowest order graphs with zero or one soft gluon and a virtual photon current (for simplicity) are shown in Fig. 21. Here $k^\mu \sim \Lambda_{\rm QCD}$ is soft, and $p^\mu \sim Q$, $p'^\mu \sim Q$ are hard momenta. To carry out the OPE we calculate and square the on-shell amplitude $\mathcal{M}_h^\mu \mathcal{M}_h^\nu$, where μ and ν are the virtual photon current indices. We sum over the final quark and antiquark spins since these particles are hard and are being integrated out. On the other hand, the gluon vector indices α and α' are left uncontracted and are used to help in identifying the operator for the nonperturbative matrix element. For simplicity, the indices α and α' are suppressed in writing down the amplitudes below. We start out without making restrictions on the number of gluons coming from $\mathcal{M}_h^\mu$ and $\mathcal{M}_h^{\nu *}$, which corresponds to directly matching onto the nonperturbative operator, without considering the final vacuum matrix element which gives a nonperturbative parameter. Since $p^2 = p'^2 = k^2 = 0$ the denominators of the propagators in the one-gluon graphs reduce to $2p \cdot k$ and $2p' \cdot k$. In the numerators we can drop $\not{k}$'s relative to the large $\not{p}$ and $\not{p}'$. The interference between the zero and one gluon amplitudes gives

$$\mathcal{M}_h^\mu \mathcal{M}_h^{\nu *} = N_c \mathrm{tr}[\not{p}\gamma^\mu \not{p}'\gamma^\nu] \frac{2gT^A}{N_c} \left[\frac{p'^\alpha}{p' \cdot k} - \frac{p^\alpha}{p \cdot k} \right]. \quad \text{(C1)}$$

The interference with one gluon from each of $\mathcal{M}_h^\mu$ and $\mathcal{M}_h^{\nu *}$ is

$$\mathcal{M}_h^\mu \mathcal{M}_h^{\nu *} = N_c \,\mathrm{tr}[\not{p}\gamma^\mu \not{p}'\gamma^\nu] \frac{g^2 T^A T^B}{N_c} \left[\frac{p^\alpha p^{\alpha'}}{(p \cdot k)^2} + \frac{p'^\alpha p'^{\alpha'}}{(p' \cdot k)^2} - \frac{(p^\alpha p'^{\alpha'} + p'^\alpha p^{\alpha'})}{(p \cdot k)(p' \cdot k)} \right]. \quad \text{(C2)}$$

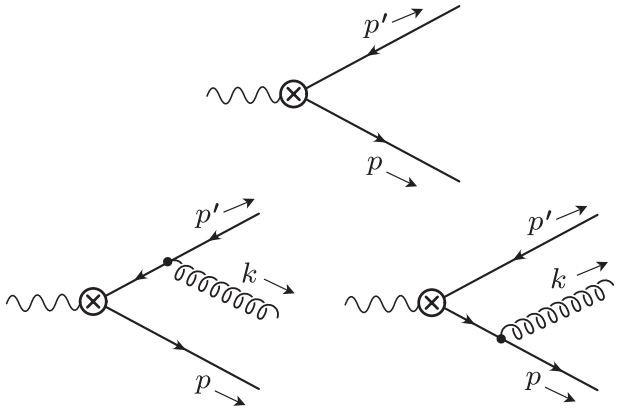

FIG. 21. Amplitudes for zero and one soft gluon.

Continuing in this fashion with any number of gluons from $\mathcal{M}_h^\mu$ and any number from $\mathcal{M}_h^{\nu *}$ we always find the tree level amplitude squared with no soft gluons, $N_c \,\mathrm{tr}[\not{p}\gamma^\mu \not{p}'\gamma^\nu]$, times an amplitude from the soft gluons.

Since the hard quarks are on-shell and back-to-back their four-momenta are given by lightlike vectors along the thrust axis:

$$p^\mu = n^\mu \frac{\bar{n} \cdot p}{2}, \qquad p'^\mu = \bar{n}^\mu \frac{n \cdot p}{2}, \quad \text{(C3)}$$

up to power corrections beyond those considered here. Here $n^\mu = (1, \hat{\mathbf{t}})$ and $\bar{n}^\mu = (1, -\hat{\mathbf{t}})$ are identical to the n and $\bar{n}$ appearing in Eq. (6). Using Eq. (C3) the soft gluon amplitudes in Eqs. (C1) and (C2) are eikonal with precisely the right factors to come from the $\bar{Y}_{\bar{n}}^T(0)$, $Y_n(0)$, $Y_n^\dagger(0)$, and $\bar{Y}_{\bar{n}}^*(0)$ in the Ω_1 matrix element in Eq. (6).

For the first moment observable we can focus on amplitudes that have the same number of gluons in $\mathcal{M}_h^\mu$ and $\mathcal{M}_h^{\nu *}$ and at least one gluon for the $i\hat{\partial}$ operation in Eq. (6) to act on. Since the gluon is soft, the factor of τ in $\int d\tau (\tau/\sigma)(d\sigma/d\tau)$ is given by

$$\tau = \min\left[\frac{2p \cdot k}{q^2}, \frac{2p' \cdot k}{q^2} \right] = \frac{1}{Q} \min[n \cdot k, \bar{n} \cdot k]$$
$$= \frac{1}{Q} \{ n \cdot k \,\theta(\bar{n} \cdot k - n \cdot k) + \bar{n} \cdot k \,\theta(n \cdot k - \bar{n} \cdot k) \}, \quad \text{(C4)}$$

and is exactly equal to $i\hat{\partial}$ given in Eq. (7) acting on the soft gluon in Fig. 21. Hence in the first moment of thrust we find that τ together with the soft gluon amplitude give precisely $2\Omega_1/Q$, with the vacuum matrix in Eq. (6) (where the trace comes from the sum over color for the final-state quarks). The remaining $N_c \,\mathrm{tr}[\not{p}\gamma^\mu \not{p}'\gamma^\nu]$ amplitude goes together with the two-body phase space to yield the tree level cross section σ_0^I. Together these results yield Eq. (25) for the lowest order OPE for the first moment of thrust.

[1] S. Kluth, Rep. Prog. Phys. **69**, 1771 (2006).
[2] E. Farhi, Phys. Rev. Lett. **39**, 1587 (1977).
[3] A. Gehrmann-De Ridder, T. Gehrmann, E. W. N. Glover, and G. Heinrich, Phys. Rev. Lett. **99**, 132002 (2007).
[4] A. Gehrmann-De Ridder, T. Gehrmann, E. W. N. Glover, and G. Heinrich, J. High Energy Phys. 12 (2007) 094.
[5] S. Weinzierl, Phys. Rev. Lett. **101**, 162001 (2008).
[6] S. Weinzierl, J. High Energy Phys. 06 (2009) 041.
[7] C. W. Bauer, D. Pirjol, and I. W. Stewart, Phys. Rev. D **65**, 054022 (2002).
[8] C. W. Bauer, S. Fleming, and M. E. Luke, Phys. Rev. D **63**, 014006 (2000).
[9] C. W. Bauer, S. Fleming, D. Pirjol, and I. W. Stewart, Phys. Rev. D **63**, 114020 (2001).
[10] C. W. Bauer and I. W. Stewart, Phys. Lett. B **516**, 134 (2001).
[11] C. W. Bauer, S. Fleming, D. Pirjol, I. Z. Rothstein, and I. W. Stewart, Phys. Rev. D **66**, 014017 (2002).
[12] C. W. Bauer, A. V. Manohar, and M. B. Wise, Phys. Rev. Lett. **91**, 122001 (2003).
[13] C. W. Bauer, C. Lee, A. V. Manohar, and M. B. Wise, Phys. Rev. D **70**, 034014 (2004).
[14] S. Fleming, A. H. Hoang, S. Mantry, and I. W. Stewart, Phys. Rev. D **77**, 074010 (2008).
[15] M. D. Schwartz, Phys. Rev. D **77**, 014026 (2008).
[16] A. H. Hoang and I. W. Stewart, Phys. Lett. B **660**, 483 (2008).
[17] G. P. Korchemsky and G. Sterman, Nucl. Phys. **B555**, 335 (1999).
[18] G. P. Korchemsky and S. Tafat, J. High Energy Phys. 10 (2000) 010.
[19] G. P. Korchemsky, arXiv:hep-ph/9806537.
[20] T. Becher and M. D. Schwartz, J. High Energy Phys. 07 (2008) 034.
[21] S. Catani, L. Trentadue, G. Turnock, and B. R. Webber, Nucl. Phys. **B407**, 3 (1993).
[22] G. Dissertori *et al.*, J. High Energy Phys. 02 (2008) 040.
[23] R. A. Davison and B. R. Webber, Eur. Phys. J. C **59**, 13 (2008).
[24] S. Bethke, S. Kluth, C. Pahl, and J. Schieck (JADE Collaboration), Eur. Phys. J. C **64**, 351 (2009).
[25] G. Dissertori *et al.*, J. High Energy Phys. 08 (2009) 036.
[26] R. W. L. Jones, M. Ford, G. P. Salam, H. Stenzel, and D. Wicke, J. High Energy Phys. 12 (2003) 007.
[27] M. Beneke, Phys. Rep. **317**, 1 (1999).
[28] A. V. Manohar and M. B. Wise, Phys. Lett. B **344**, 407 (1995).
[29] B. R. Webber, Phys. Lett. B **339**, 148 (1994).
[30] Y. L. Dokshitzer and B. R. Webber, Phys. Lett. B **352**, 451 (1995).
[31] R. Akhoury and V. I. Zakharov, Phys. Lett. B **357**, 646 (1995).
[32] P. Nason and M. H. Seymour, Nucl. Phys. **B454**, 291 (1995).
[33] G. P. Korchemsky and G. Sterman, Nucl. Phys. **B437**, 415 (1995).
[34] P. A. Movilla Fernandez, S. Bethke, O. Biebel, and S. Kluth, Eur. Phys. J. C **22**, 1 (2001).
[35] Y. L. Dokshitzer, G. Marchesini, and B. R. Webber, Nucl. Phys. **B469**, 93 (1996).
[36] E. Gardi and J. Rathsman, Nucl. Phys. **B609**, 123 (2001).
[37] E. Gardi and J. Rathsman, Nucl. Phys. **B638**, 243 (2002).
[38] Z. Ligeti, I. W. Stewart, and F. J. Tackmann, Phys. Rev. D **78**, 114014 (2008).
[39] A. H. Hoang, A. Jain, I. Scimemi, and I. W. Stewart, Phys. Rev. Lett. **101**, 151602 (2008).
[40] A. H. Hoang, A. Jain, I. Scimemi, and I. W. Stewart, Phys. Rev. D **82**, 011501 (2010).
[41] S. Fleming, A. H. Hoang, S. Mantry, and I. W. Stewart, Phys. Rev. D **77**, 114003 (2008).
[42] P. A. Baikov, K. G. Chetyrkin, A. V. Smirnov, V. A. Smirnov, and M. Steinhauser, Phys. Rev. Lett. **102**, 212002 (2009).
[43] A. Denner, S. Dittmaier, T. Gehrmann, and C. Kurz, Phys. Lett. B **679**, 219 (2009).
[44] A. Denner, S. Dittmaier, T. Gehrmann, and C. Kurz, Nucl. Phys. **B836**, 37 (2010).
[45] I. Wolfram Research, *Mathematica Edition: Version 7.0* (Wolfram Research, Champaign, IL, 2008).
[46] C. F. Berger and G. Sterman, J. High Energy Phys. 09 (2003) 058.
[47] A. V. Belitsky, G. P. Korchemsky, and G. Sterman, Phys. Lett. B **515**, 297 (2001).
[48] T. Matsuura and W. L. van Neerven, Z. Phys. C **38**, 623 (1988).
[49] T. Matsuura, S. C. van der Marck, and W. L. van Neerven, Nucl. Phys. **B319**, 570 (1989).
[50] T. Gehrmann, T. Huber, and D. Maitre, Phys. Lett. B **622**, 295 (2005).
[51] S. Moch, J. A. M. Vermaseren, and A. Vogt, J. High Energy Phys. 08 (2005) 049.
[52] R. N. Lee, A. V. Smirnov, and V. A. Smirnov, J. High Energy Phys. 04 (2010) 020.
[53] G. Heinrich, T. Huber, D. A. Kosower, and V. A. Smirnov, Phys. Lett. B **678**, 359 (2009).
[54] T. Gehrmann, E. W. N. Glover, T. Huber, N. Ikizlerli, and C. Studerus, J. High Energy Phys. 06 (2010) 094.
[55] I. W. Stewart, F. J. Tackmann, and W. J. Waalewijn, Phys. Rev. D **81**, 094035 (2010).
[56] B. A. Kniehl and J. H. Kuhn, Nucl. Phys. **B329**, 547 (1990).
[57] W. L. van Neerven, Nucl. Phys. **B268**, 453 (1986).
[58] E. Lunghi, D. Pirjol, and D. Wyler, Nucl. Phys. **B649**, 349 (2003).
[59] C. W. Bauer and A. V. Manohar, Phys. Rev. D **70**, 034024 (2004).
[60] T. Becher and M. Neubert, Phys. Lett. B **637**, 251 (2006).
[61] S. Moch, J. A. M. Vermaseren, and A. Vogt, Nucl. Phys. **B688**, 101 (2004).
[62] A. H. Hoang and S. Kluth, arXiv:0806.3852.
[63] S. Catani and M. H. Seymour, Phys. Lett. B **378**, 287 (1996).
[64] S. Catani and M. H. Seymour, Nucl. Phys. **B485**, 291 (1997).
[65] C. Lee and G. Sterman, *Proceedings of the FRIF Workshop on First Principles Non-Perturbative QCD of Hadron Jets, Paris, 2006*, econf C06/01/12.1, A001 (2006).
[66] C. Lee and G. Sterman, Phys. Rev. D **75**, 014022 (2007).
[67] K. S. M. Lee and I. W. Stewart, Nucl. Phys. **B721**, 325 (2005).

[68] G. Paz, J. High Energy Phys. 06 (2009) 083.
[69] R. K. Ellis, D. A. Ross, and A. E. Terrano, Nucl. Phys. **B178**, 421 (1981).
[70] K. Hagiwara, T. Kuruma, and Y. Yamada, Nucl. Phys. **B358**, 80 (1991).
[71] A. Jain, I. Scimemi, and I. W. Stewart, Phys. Rev. D **77**, 094008 (2008).
[72] P. Achard *et al.* (L3 Collaboration), Phys. Rep. **399**, 71 (2004).
[73] D. Buskulic *et al.* (ALEPH Collaboration), Phys. Lett. B **355**, 381 (1995).
[74] G. Abbiendi *et al.* (OPAL Collaboration), Eur. Phys. J. C **11**, 643 (1999).
[75] H. Boos, T. Feldmann, T. Mannel, and B. D. Pecjak, J. High Energy Phys. 05 (2006) 056.
[76] B. L. Ioffe, Phys. Lett. **78B**, 277 (1978).
[77] H. P. Nilles, Phys. Rev. Lett. **45**, 319 (1980).
[78] A. Brandenburg and P. Uwer, Nucl. Phys. **B515**, 279 (1998).
[79] P. Nason and C. Oleari, Nucl. Phys. **B521**, 237 (1998).
[80] G. Rodrigo, M. S. Bilenky, and A. Santamaria, Nucl. Phys. **B554**, 257 (1999).
[81] K. G. Chetyrkin, J. H. Kuhn, and A. Kwiatkowski, Phys. Rep. **277**, 189 (1996).
[82] W. Braunschweig *et al.* (TASSO Collaboration), Z. Phys. C **47**, 187 (1990).
[83] Y. K. Li *et al.* (AMY Collaboration), Phys. Rev. D **41**, 2675 (1990).
[84] P. A. Movilla Fernandez, O. Biebel, S. Bethke, S. Kluth, and P. Pfeifenschneider (JADE Collaboration), Eur. Phys. J. C **1**, 461 (1998).
[85] K. Abe *et al.* (SLD Collaboration), Phys. Rev. D **51**, 962 (1995).
[86] B. Adeva *et al.* (L3 Collaboration), Z. Phys. C **55**, 39 (1992).
[87] J. Abdallah *et al.* (DELPHI Collaboration), Eur. Phys. J. C **29**, 285 (2003).
[88] P. Abreu *et al.* (DELPHI Collaboration), Eur. Phys. J. C **14**, 557 (2000).
[89] D. Wicke, Report No. wU-B-DIS-1999-05, 1999.
[90] P. Abreu *et al.* (DELPHI Collaboration), Phys. Lett. B **456**, 322 (1999).
[91] G. Abbiendi *et al.* (OPAL Collaboration), Eur. Phys. J. C **40**, 287 (2005).
[92] K. Ackerstaff *et al.* (OPAL Collaboration), Z. Phys. C **75**, 193 (1997).
[93] G. Abbiendi *et al.* (OPAL Collaboration), Eur. Phys. J. C **16**, 185 (2000).
[94] A. Heister *et al.* (ALEPH Collaboration), Eur. Phys. J. C **35**, 457 (2004).
[95] T. Gehrmann, M. Jaquier, and G. Luisoni, Eur. Phys. J. C **67**, 57 (2010).
[96] C. F. Berger, T. Kucs, and G. Sterman, Phys. Rev. D **68**, 014012 (2003).
[97] A. Hornig, C. Lee, and G. Ovanesyan, J. High Energy Phys. 05 (2009) 122.
[98] G. P. Salam and D. Wicke, J. High Energy Phys. 05 (2001) 061.
[99] Y.-T. Chien and M. D. Schwartz, J. High Energy Phys. 08 (2010) 058.
[100] J. Blumlein, H. Bottcher, and A. Guffanti, Nucl. Phys. **B774**, 182 (2007).
[101] A. D. Martin, W. J. Stirling, R. S. Thorne, and G. Watt, Eur. Phys. J. C **64**, 653 (2009).
[102] S. Alekhin, J. Blumlein, S. Klein, and S. Moch, Phys. Rev. D **81**, 014032 (2010).
[103] F. Demartin, S. Forte, E. Mariani, J. Rojo, and A. Vicini, Phys. Rev. D **82**, 014002 (2010).
[104] H.-L. Lai *et al.*, Phys. Rev. D **82**, 054021 (2010).
[105] C. T. H. Davies *et al.* (HPQCD Collaboration), Phys. Rev. D **78**, 114507 (2008).
[106] H. Flacher *et al.*, Eur. Phys. J. C **60**, 543 (2009).
[107] M. Beneke and M. Jamin, J. High Energy Phys. 09 (2008) 044.
[108] M. Davier, S. Descotes-Genon, A. Hocker, B. Malaescu, and Z. Zhang, Eur. Phys. J. C **56**, 305 (2008).
[109] S. Bethke, Eur. Phys. J. C **64**, 689 (2009).
[110] K. Maltman and T. Yavin, Phys. Rev. D **78**, 094020 (2008).
[111] S. Bethke, Prog. Part. Nucl. Phys. **58**, 351 (2007).
[112] W. M. Yao *et al.* (Particle Data Group), J. Phys. G **33**, 1 (2006).
[113] C. Balzereit, T. Mannel, and W. Kilian, Phys. Rev. D **58**, 114029 (1998).
[114] M. Neubert, Eur. Phys. J. C **40**, 165 (2005).
[115] S. W. Bosch, B. O. Lange, M. Neubert, and G. Paz, Nucl. Phys. **B699**, 335 (2004).
[116] O. V. Tarasov, A. A. Vladimirov, and A. Y. Zharkov, Phys. Lett. **93B**, 429 (1980).
[117] S. A. Larin and J. A. M. Vermaseren, Phys. Lett. B **303**, 334 (1993).
[118] T. van Ritbergen, J. A. M. Vermaseren, and S. A. Larin, Phys. Lett. B **400**, 379 (1997).
[119] G. P. Korchemsky and A. V. Radyushkin, Nucl. Phys. **B283**, 342 (1987).
[120] M. Czakon, Nucl. Phys. **B710**, 485 (2005).
[121] A. Vogt, Phys. Lett. B **497**, 228 (2001).
[122] A. Idilbi, X. dong Ji, and F. Yuan, Nucl. Phys. **B753**, 42 (2006).
[123] T. Becher, M. Neubert, and B. D. Pecjak, J. High Energy Phys. 01 (2007) 076.
[124] M. A. Shifman, A. I. Vainshtein, and V. I. Zakharov, Nucl. Phys. **B147**, 385 (1979).